December 2019

Chemical Self-Assembly Strategies Toward the Design of Molecular Electronic Circuits

Dustin Olson
University of Wisconsin-Milwaukee

CHEMICAL SELF-ASSEMBLY STRATEGIES TOWARD THE DESIGN OF MOLECULAR ELECTRONIC CIRCUITS

by

Dustin R. Olson

A Dissertation Submitted in

Partial Fulfillment of the

Requirements for the Degree of

Doctor of Philosophy

in Chemistry

at

The University of Wisconsin-Milwaukee

December 2019

ABSTRACT

CHEMICAL SELF-ASSEMBLY STRATEGIES TOWARD THE DESIGN OF MOLECULAR ELECTRONIC CIRCUITS

by

Dustin R. Olson

The University of Wisconsin-Milwaukee, 2019
Under the Supervision of Professor Wilfred T. Tysoe

The field of molecular electronics is generally divided into one of two major categories, the first focusing on the unique functionalization of single molecules to produce electronic behavior, the other utilizing large assemblies of molecules to produce electronic behavior. The former approach is largely attributed to the seminal paper by Aviram and Ratner in which they proposed a molecular donor-bridge-acceptor $(D-B-A)$ type architecture could lead to single molecule rectification producing electronic effects similar to conventional semiconductor based diodes. Extensive research has been carried out in both fields as it is foreseen that new approaches to electronics miniaturization will be necessary in the near future.

In the following research, the focus turns to a seemingly overlooked area of molecular electronics, this being the necessity for designed interconnects of nanoscale electrodes. The approach to problem utilized the well studied oligomerization properties of 1,4-phenylene diisocyanide (PDI), which upon exposure to gold incorporates gold adatoms to form conductive one-dimensional oligomers of the form -(Au-PDI)$_n$-. Monte Carlo simulations along with conductivity studies of nanoparticle arrays both suggest the oligomerization is inherently self-limiting, providing a potential avenue toward controlled interconnection of nanoelectrodes and design of molecular electronic circuits.

TABLE OF CONTENTS

LIST OF FIGURES

LIST OF TABLES

LIST OF ABBREVIATIONS

AFM	**A**tomic **F**orce **M**icroscopy
DFT	**D**ensity **F**unctional **T**heory
RAIRS	**R**eflection **A**bsorbtion **I**nfrared **S**pectroscopy
QCM	**Q**uartz **C**rystal **M**icrobalance
SEM	**S**canning **E**lectron **M**icroscopy
STM	**S**canning **T**unneling **M**icroscopy
TPD	**T**emperature **P**rogrammed **D**esorption
UHV	**U**ltra **H**igh **V**acuum

ACKNOWLEDGEMENTS

I would first and foremost like to thank my advisor, Prof. Wilfred T. Tysoe. His guidance throughout my time in his research group has been instrumental to the success of the following research. His work ethic has been truly inspiring, and sets a great example of what is necessary to be successful in the lab. Finally, I would like to thank him for his outstanding support of his students.

A sincere thank you goes to each of my committee members, Prof. Jorg Woehl, Prof. Alan Schwabacher, Prof. Jian Chen, and Prof. Arsenio Pacheco. Each of them has provided valuable ideas, and insight during yearly committee meetings that is greatly appreciated.

I would like to thank my family, friends and Alex, for their love and continuous support. They provided a great support system, with constant words of encouragement throughout my time in graduate school. I must thank my mother especially for continually encouraging me to pursue higher education.

Last, but not least I must thank the many Tysoe group members, both current and former that I have had the pleasure to learn from, and collaborate with throughout my time at UWM. I could always count on a positive, encouraging attitude in the lab, which has made my time at UWM very enjoyable.

Chapter 1

Introduction

Since the invention of the semiconductor-based integrated circuit by Jack Kilby in 1958 [1], and its following integration into consumer electronics, the semiconductor industry has expanded to become a $429 billion market annually. The common theme of this industry is the continual decrease in the size of single transistors that can be fabricated, allowing for the packing of more and more devices into smaller packages improving both efficiency and computational power. It was predicted in 1965 by Gordon Moore one of the founders of intel, that the number of transistors on integrated chips would double every year, and this prediction is now referred to as "Moore's law" [2] and has stood the test of time for nearly six decades.

The industry approach to this continual decrease in the size of components of an integrated circuit can be regarded as a "top-down" approach to electronic circuit miniaturization, as the methods to do so rely on the improvement of photolithography techniques, in which large silicon wafers are transformed into integrated circuits. It is predicted that these conventional techniques are reaching their limits, effectively ending the long standing prediction of "Moores law", and if further miniaturization is to continue new approaches must be used.

One of the first suggestions to a new approach which can be viewed as a "bottom-up" approach toward the design of circuits, was Richard Feynman's "Plenty of room at

the bottom" [3] lecture at an annual APS meeting in 1959, where he suggested the enormous possibilities the could come from the ability to store information on an atomic scale. Since this seminal speech, enormous amounts of research have been done in fields such as quantum computation, and spintronics both attempting to encode information into single, or coupled atoms. An alternative approach is that of molecular electronics, a field focused on functionalization of single molecules to produce electronic behaviour similar to conventional silicon-based electronics.

Largely accredited with the growth of interest in molecular electronics was a paper by Aviram and Ratner that proposed a molecular architecture that could produce single molecule rectification by tuning the alignment of molecular orbital energies relative to the Fermi level of the electrodes [4]. The ability to acquire electrical measurements of single molecules largely eluded experimentation until the invention of the scanning tunneling microscope (STM). Following its development in 1982, some of the first single molecule coductivity studies were conducted [5]. This work, focuses not only on the functionalization of single molecules, but also on the application of molecular self-assembly as a means to interconnect nanoelectrodes, a necessity if true molecular based circuits are to be realized.

This dissertation begins by introducing the equipment necessary to achieve and maintain high and ultrahigh vacuum conditions ($1 \times 10^{-8} - 1 \times 10^{-10}$ Torr) used in a majority of the work that follows. Descriptions of the working mechanisms for the common vacuum pumps used in the lab are provided (Chapter 2). In Chapter 3 the details for both experimental and theoretical methods applied throughout the remaining chapters are given. Details are provided for sample preparation both of single crystal samples and gold nanoparticle arrays used for electrical measurements, as well as descriptions of the theory and working principles of experimental techniques used in UHV.

The design of molecular electronic circuits will require the development of strategies for making controlled interconnections between nanoelectrodes. The simplest example of a molecular electronic component consists of aryl rings with para-anchoring functionalities, commonly isocyanide or thiol groups. In particular, 1,4-phenylene diisocyanide (1,4-PDI) has been shown to form conductive one-dimensional, oligomeric chains that are composed of alternating gold and 1,4-PDI units in which a gold adatom is linked to two trans isocyanide groups [6]. Density functional theory (DFT) calculations of the oligomerization pathway reveal that growth occurs via a vertical, mobile Au–PDI adatom complex that forms by binding to the gold substrate and oligomerizes by the gold adatom attaching to the isocyanide terminus of a growing chain. In this case, the gold atoms in the oligomer derive from the gold substrate [7]. In principle, bridging between adjacent electrodes could be tuned by controlling the 1,4-PDI dose [8]. However, because both nucleation of the adatom complex and the subsequent oligomerization reactions occur at the periphery of gold nanoparticles, it is postulated that oligomer growth is inherently self-limiting. In (Chapter 4) an analytical model is developed for this process that demonstrates the existence of self-limiting growth. This is modeled in greater detail using kinetic Monte Carlo simulations with the energy parameters derived from DFT calculation on gold that confirm that the growth is self-limiting and predicts that bridging between nanoelectrodes should only occur for spacings less than $\sim$12 nm and is depicted in Figure 1.1.

In order to test the postulated self-limiting oligomerization predicted for 1,4-PDI on nanoparticle by Monte Carlo simulations two types of nanoparticle arrays are fabricated and their conductivity investigated in (Chapter 5). The first device consisting of electrodes with a separation of (0.25 mm), upon which gold nanoparticles are deposited in vacuum. We find that increasing nanoparticle separation results in a decrease in the change in conductivity when exposed to PDI in vacuum. In order to

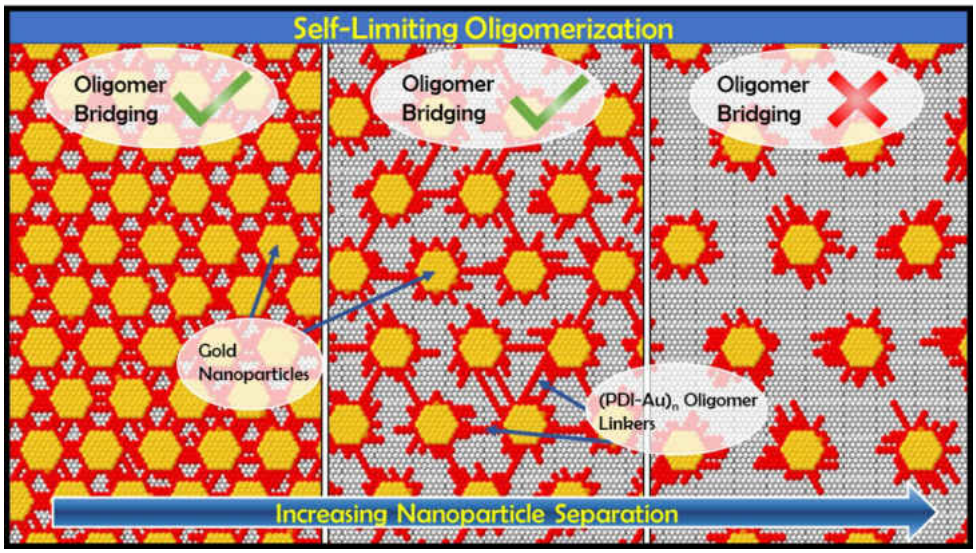

FIGURE 1.1: Monte Carlo simulations, predicting the self-limiting oliogmerization of 1,4-PDI, demonstrated by the lack of connectivity between nodal points with separations of >12nm.

more accurately investigate the self-limiting properties of PDI, nanogap samples are prepared by means of electron beam lithography. We find that no change in conductivity is observed for gaps of 30 nm when saturated with PDI, whereas when the gap is reduce to ∼10 nm by the deposition of gold nanoparticles a significant change is observed during exposure(Fig 1.2) Both of the fabricated nanoparticle samples are found to suggest the predicted self-limiting behavior of oligomer formation by PDI, suggesting oligomeric structures formed by PDI could be used for targeted briging of nanoelectrodes.

Following the proposal of Aviram and Ratner that a properly functionalized single molecule could act as a molecular rectifier [4], in Chapter 6 we investigate a potential molecular diode candidate 4-isocyanophenyl disulfide(ICPD). It is assumed that adsorption on a gold surface will lead to the dissociation of the disulfide bond producing a para-substituted ring with both isocyanide and thiolate functionality. The surface chemistry of ICPD is studied on a Au(111) surface by the combination of reflection absorbtion infrared spectroscopy (RAIRS), and temperature programmed desorption

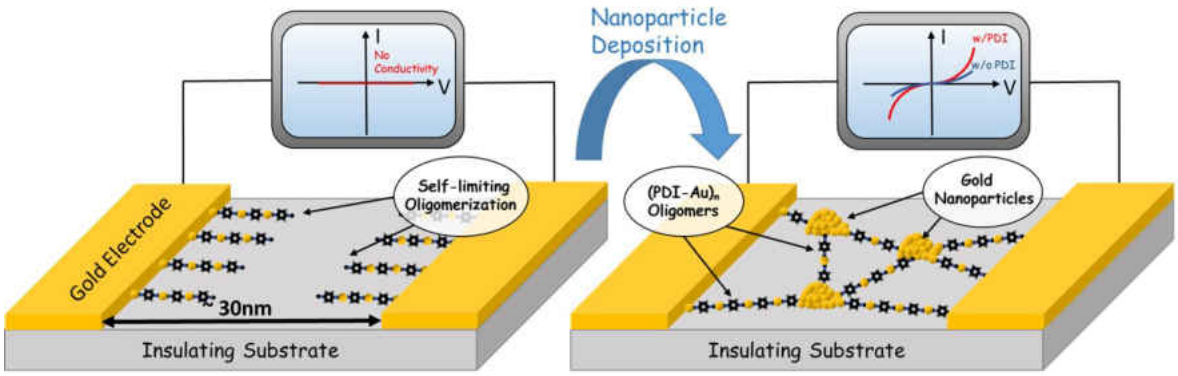

FIGURE 1.2: Depiction of experimental observation of self-limiting oligomerization. No increase in conductivity is observed for 30 nm gaps upon exposure to PDI, whereas when the gap is reduced by the addition of nanoparticles, a significant change in conductivity is observed.

(TPD). The presence of the well known surface bound isocyanide mode in infrared suggests the formation of oligomeric species in accord with those previously observed for 1,4-PDI.

The use of dithiols as molecular electronic components has seen extensive research [9] due largely to the ability of thiols to deprotonate and form strong thiolate binding with gold. It has been previously suggested that dithiols, similarly to diisocyanides, form oligomeric chains by the incoperation of gold adatoms [10] between molecules. In Chapter 7, we interrogate the oligomeric structures formed by 1,4-BDT on Au(111) with a combination of STM, and density functional theory (DFT), finding agreement with the previously postulated structures of the oligomers.

Bibliography

[1] Jack S Kilby. Miniaturized electronic circuits, June 23 1964. US Patent 3,138,743.

[2] Gordon E Moore et al. Cramming more components onto integrated circuits, 1965.

[3] Richard P Feynman. Plenty of room at the bottom. In *APS annual meeting*, 1959.

[4] Arieh Aviram and Mark A Ratner. Molecular rectifiers. *Chemical physics letters*, 29(2):277–283, 1974.

[5] X. D. Cui, A. Primak, X. Zarate, J. Tomfohr, O. F. Sankey, A. L. Moore, T. A. Moore, D. Gust, G. Harris, and S. M. Lindsay. Reproducible measurement of single-molecule conductivity. *Science*, 294(5542):571–574, 2001.

[6] Jorge A Boscoboinik, Florencia C Calaza, Zeesham Habeeb, Dennis W Bennett, Dario J Stacchiola, Martin A Purino, and Wilfred T Tysoe. One-dimensional supramolecular surface structures: 1, 4-diisocyanobenzene on au (111) surfaces. *Physical Chemistry Chemical Physics*, 12(37):11624–11629, 2010.

[7] John Kestell, Rasha Abuflaha, J Anibal Boscoboinik, Michael Garvey, Dennis W Bennett, and Wilfred T Tysoe. Determination of adsorbate structures from 1, 4-phenylene diisocyanide on gold. *The journal of physical chemistry letters*, 5(20):3577–3581, 2014.

[8] Alejandro Miguel Boscoboinik, Sergio Javier Manzi, WT Tysoe, Victor Daniel Pereyra, and JA Boscoboinik. Directed nanoscale self-assembly of molecular wires

interconnecting nodal points using monte carlo simulations. *Chemistry of Materials*, 27(19):6642–6649, 2015.

[9] Hyunwook Song, Mark A Reed, and Takhee Lee. Single-molecule devices: Single molecule electronic devices (adv. mater. 14/2011). *Advanced Materials*, 23(14):1576–1576, 2011.

[10] John Kestell, Rasha Abuflaha, Michael Garvey, and Wilfred T Tysoe. Self-assembled oligomeric structures from 1, 4-benzenedithiol on au (111) and the formation of conductive linkers between gold nanoparticles. *The Journal of Physical Chemistry C*, 119(40):23042–23051, 2015.

Chapter 2

Ultrahigh Vacuum Systems

2.1 Why UHV?

Ultrahigh vacuum (UHV) refers to pressures on the order of $1 \times 10^{-8} - 1 \times 10^{-10}$ Torr, roughly a ten billion fold reduction in pressure relative to atmosphere. Achieving pressures of this magnitude not only requires sophisticated vacuum pumps, but can require days of baking the vacuum chamber to drive off any residual gases that have adsorbed onto the walls. The obvious question then becomes why would someone go through the difficulty of achieving these pressures, what are the advantages?

Main issues due to the frequency of collisions at atmospheric pressure are largely resoved by the extremely long mean-free path of atoms present in a UHV system. Where here the mean-free path refers to the average distance a molecule can travel between collisions. We approximate that gas molecules behave as hard, elastic spheres although this is generally not true due to electrostatic interactions between colliding molecules. [1] Nonetheless, this approximation allows us to define the average diameter of a moving molecule as σ as well as using Boltzmann statistics of average molecular velocity to define the mean free path as $\lambda = \frac{1}{\sqrt{2}\pi n \sigma^2}$, [2] where n is defined as the average number of gas molecules per unit volume, which is given by $n = \frac{N_A P}{RT}$, resulting in the following definition for the mean-free path $\lambda = \frac{RT}{\sqrt{2}\pi\sigma^2 N_A P}$, where here N_A is

Avogadros number, P is the pressure, T the temperature, and R the gas constant.

The above idea is important for a number of reasons, the most substantial being that it allows for the use of electron and ion based spectroscopic and diffraction techniques such as low-energy electron diffraction (LEED) and X-ray photoelectron spectroscopy (XPS) which are only a few of many common surface analytically techniques. To understand this, we can use the above equation to calculate the mean-free path at various pressures. For example, at atmospheric pressure an oxygen molecule can travel an average of roughly 100 nm before a collision occurs. In contrast, under UHV conditions, this average distance is on the order of 10 km. This large mean free path allows electrons and ions to travel the necessary distances to probe surfaces and return for detection.

The second advantage to working in UHV conditions is the ideal conditions under which experiments can be performed. This can be understood though deriving a unit of measure essential to UHV the Langmuir. We can begin the derivation by defining the exposure or number of particles colliding with a surface per unit area by

$$\Phi = \int J_n dt \tag{2.1}$$

where J_n here is the number flux, or the number of gas molecules that pass through a surface per unit time and is derived from kinetic theory. The resulting number flux for an ideal gas is then found to be $J_n = p\sqrt{\frac{1}{2\pi kTm}}$. We can then derive the units of the Langmuir by making the approximation that an average surface has roughly 1×10^{15} atoms/cm^2, and assuming that we have a sticking probability of 1, which indicates that every gas molecule that impacts the surface will adsorb. Under these assumptions, we find one Langmuir to be equivalent to 1×10^6 Torr$\times$s, which under the assumptions made leads to a surface coverage of one monolayer of adsorbed species in 1 second. This helps to clarify the point that surfaces under UHV conditions ($\sim 1 \times 10^{-10}$ Torr)

will remain clean for on the order of a few hours as one Langmuir at this pressure would correspond to 10,000s. This allows the ability to perform experiments for long times with the assurance that their surface of interest will remain mostly free of contaminating species.

2.2 Vacuum Pumps

2.2.1 Rotary Vane Pumps

The first stage in the vacuum system typically starts with a rotary vane pump, also known as a roughing, or mechanical pump. These pumps fall under the classification of gas displacement pumps as their mechanism of gas removal is through mechanical displacement of gases. These pumps consist of a rotor which spins eccentrically within a fixed stator, the rotor is equipped with two metal vanes which are forced outward by internal springs. The close contact of these vanes with the stator walls during rotation are responsible for the pumping mechanism. The entire system is submerged in oil which acts as both a sealant, and a lubricant for the system.

Depicted in Figure 2.1 is each stage of a one complete pumping cycle performed by a rotary vane pump, which begins the with suction of gas into the stator. The gas is then transported by the vanes as the rotor revolves within the system. Following transport of the gases the compression stage begins, in which a sealed outlet valve forces compression of the gas within the stator. The final stage is reached when the gas is compressed to a point in which it overcomes the force of the outlet valve releasing the gas from the system.

The importance of the rotary vane pump comes from their ability to operate at atmospheric pressures, and achieve pressures on the order of milliTorr, suitable for the next stages of pumping to begin operation. These pumps generally require very little

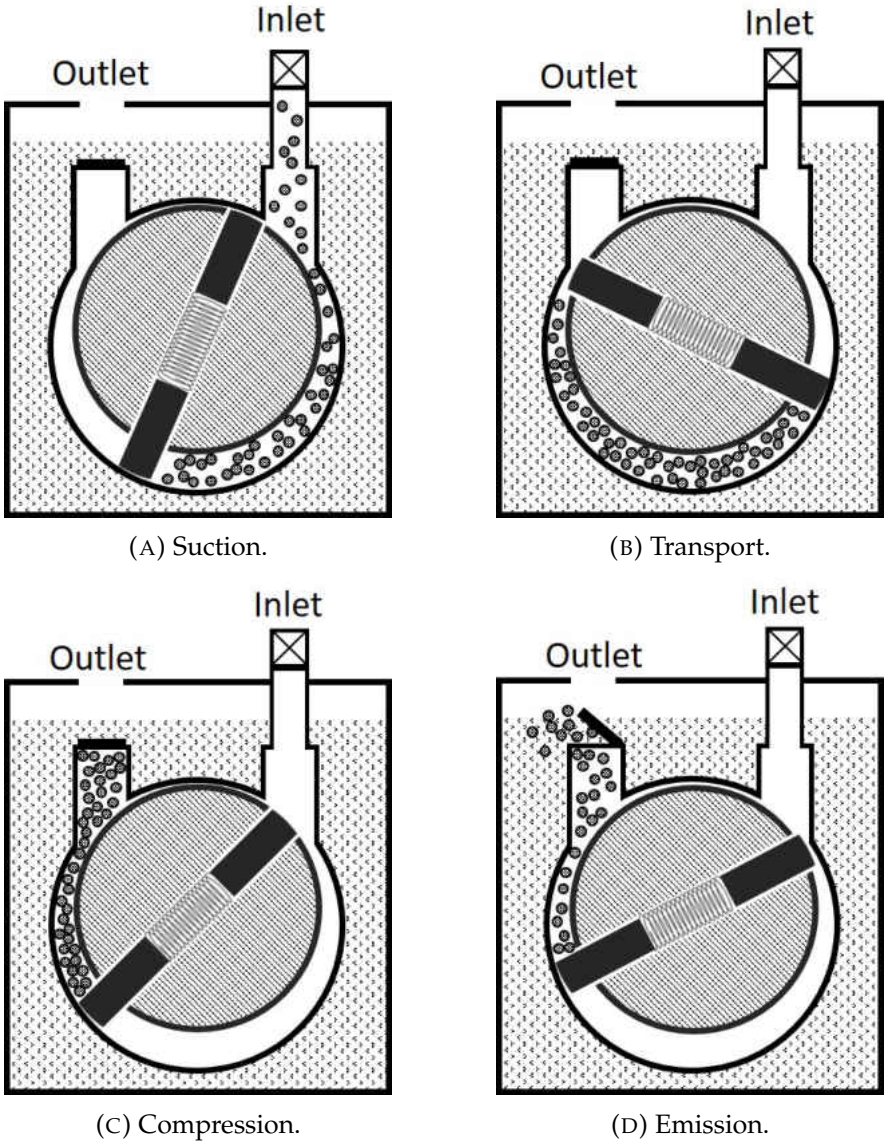

(A) Suction. (B) Transport.

(C) Compression. (D) Emission.

FIGURE 2.1: Rotary Vane Pump Operation.

maintenance apart from periodically changing the oil in the system. One potential issue limiting efficiency of these pumps is the dissolution of compressed gases within the oil, thereby lowering the minimum vacuum achievable by the pump. This issue has largly been resolved in modern pumps with the addition of a gas ballast which allows the addition of atmospheric gas to the compression stroke of a pumping cycle. The addition of atmopheric pressure gas causes the partial pressure of the unwanted vapor

to become a very small portion of the overall pressure preventing its condensation in the pump [3].

2.2.2 Turbo Molecular Pumps

The second stage of pumping for the majority of our chambers utilizes a turbo molecular pump also known as just turbo pumps for short. These types of pumps are classified as kinetic molecular pumps as their pumping mechanism relies on gas species acquiring directional momentum from collisions with spinning rotor blades, a similar mechanism occurs in jet turbines. Figure 2.2 shows a cutaway diagram of a typical turbo pump. It can be seen that in addition to the stack of spinning rotor blades, a series of fixed stator blades are also present between each set of rotor blades. As the blades spin they are capable of imparting momentum to gas molecules, effectively driving them down through the nearest stator blade. It can be seen in the cutaway (Fig. 2.2) that the geometry of the stators is such that they are designed to inhibit diffusion of gas molecules back through the pump. A very important aspect of turbo pumps is the proximity of the rotor and stator blades, in order for the pumps to work effectively the pressure must be sufficiently low such that the mean free path of the molecules is larger than the separation of the blades. This requires that turbo pumps be backed by rotary mechanical pumps bringing the pressure down to $\sim 1 \times 10^{-3}$ Torr before start up.

It can be seen in Figure 2.2 that the rotor and stator blade have continually increasing angles going towards the rear of the pump. This results in an increasing compression of gases toward the rear of the pump reducing the chamber pressure. An equation can be derived for the maximum compression ratio of a turbo pump resulting in [2],

$$K_{max} \approx \exp\left(\frac{\nu_b M^{1/2}}{(2k_b N_A T)^{1/2}}\right) f(\theta) \tag{2.2}$$

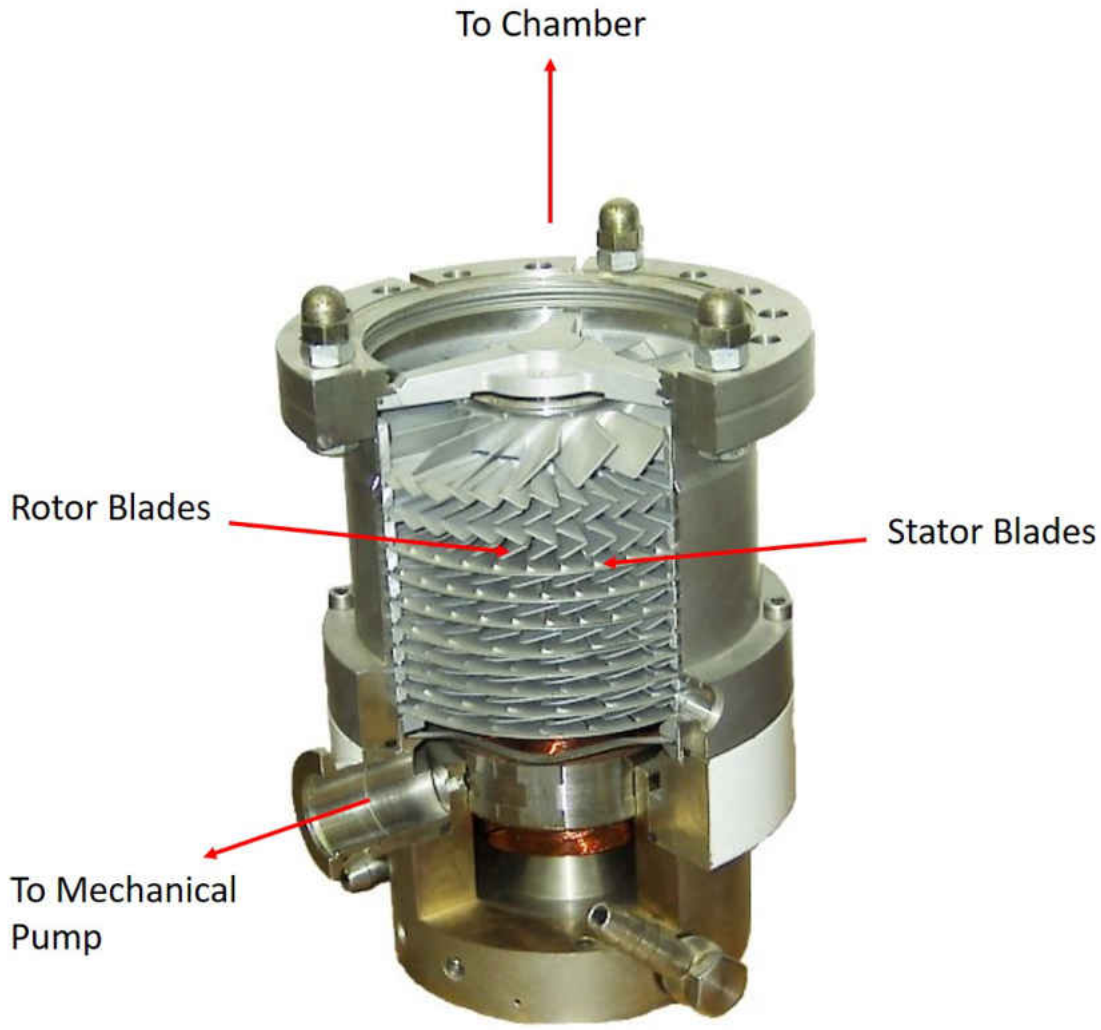

FIGURE 2.2: Cutaway of a turbomolecular pump showing inner stack of alternating rotor and stator blades [4].

A number of important points can be observed from Equation 2.2. The first being the exponential dependence of compression on the velocity of the rotor blades, as a result turbo pumps generally operate at ∼75,000 RPM. These high speeds along with the thinness of the blades result in turbo pumps to be very susceptible to damage. We can also see that the molar mass of the gases being pumped has an effect on the maximum compression, and this results in the ultimate pressures being determined by the compression ratio of light gases. Under typical operation turbo pumps provide an effective way to achieve clean vacuum, capable of reaching base pressures of 10^{-10} Torr.

Although under certain conditions, when vibrational isolation is necessary, alternative pumping methods may be required due to the mechanical nature of turbo pumps.

2.2.3 Oil Diffusion Pumps

Oil diffusion pumps, or known better simply as diffusion pumps are also classified as kinetic molecular pump similar to turbo pumps. The pumping mechanism of diffusion pumps also relies on the transfer of momentum to gas molecules causing their eventual removal from the vacuum system. In the case of a diffusion pump this momentum transfer is done by a supersonic vapor jet of oil, that is created when oil vapor is force through the cones shown in Figure **??**. The vapor jet is required to be supersonic in order to impart directional momentum to the gas molecules in vacuum, effectively forcing them to a lower stage in the pump to be removed by a mechanical backing pump.

Diffusion pumps, similarly to turbo pumps, require the backing of a mechanical pump before the can become effective. In addition to the backing pump there is the requirement of cooling typically by means of cooling rings for water circulation. In our lab these pumps are typically reserved for use on gas-lines, although when operated with a cold trap maintained with liquid nitrogen diffusion pumps can acheive and maintain UHV conditions with the main limitation being the specific oil used in the pump. Advantages of diffusion pump are their ease of maintenance as there are no moving parts in the pump, in addition they are capable of very high pumping speeds that are only limited by the diameter of the inlet to the pump [2]. Although they come with some downsides, primarily being that they require large amounts of liquid nitrogen to maintain UHV, as well as can result in the back streaming of oil into the chamber contaminating both instrumentation and the sample being studied.

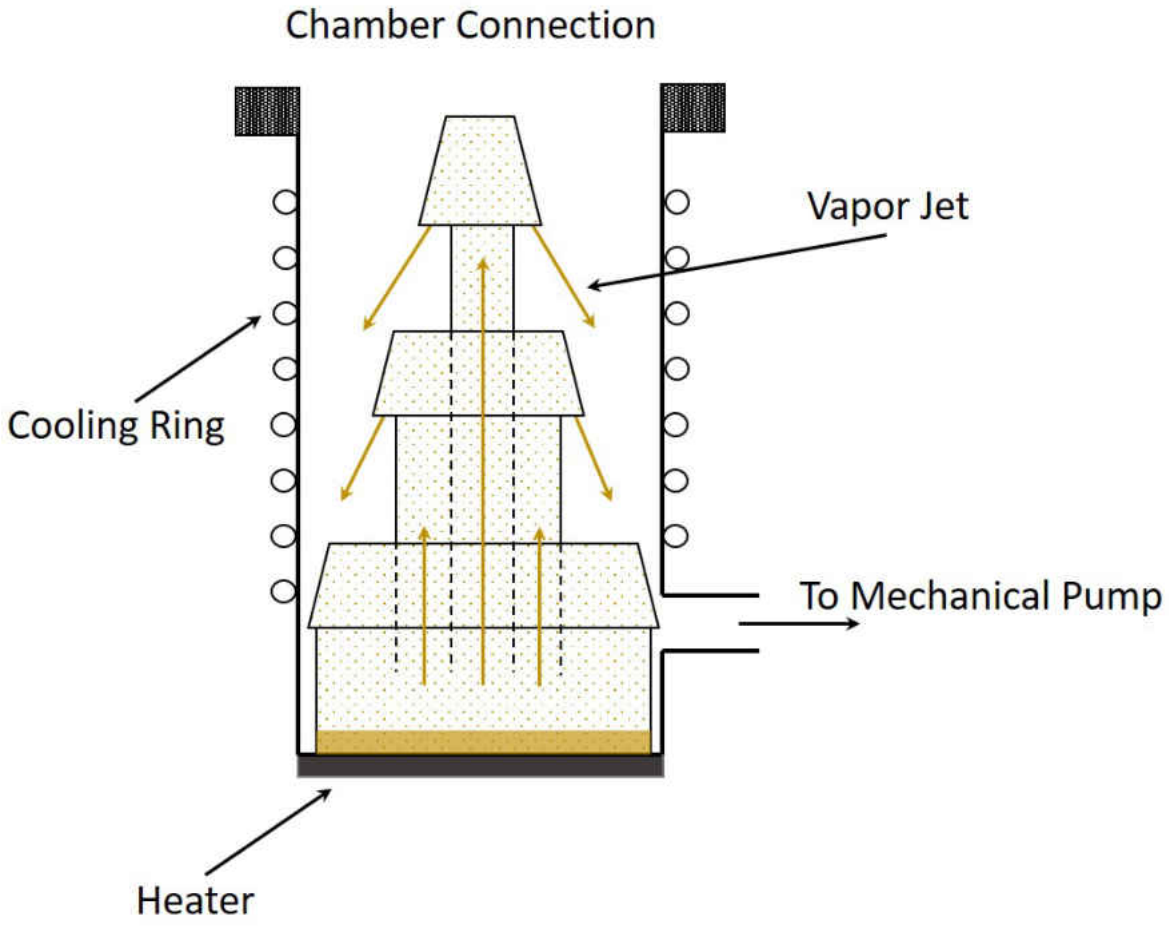

FIGURE 2.3: Depiction of diffusion pump, oil heated at the base is vaporized and forced through pumping stages resulting in a vapor jet that forces gas molecules downward to be removed by a mechanical pump.

2.2.4 Ion Pumps

Ion pumps, also known as sputter-ion, or getter-ion pumps provide a clean, non-mechanical method of achieving and maintaining UHV. The working principle of an ion-pump is ionization of gas molecules followed by either gettering or sputtering of the ionized species, this requires both a permanent magnetic field, and high voltages ($\sim 3000 - 7000$) kV [2, 5]. The high voltage applied between the anode and cathode of a pumping element Figure 2.4B results in electrical discharge, and in the presence of the magnetic field, these stray electrons move toward the anode in a spiral-shaped

motion, increasing the likelihood that they will collide with a gas molecule. Following collision the gas species will form a positive ion, as well as secondary electrons that can contribute to the ionization of other species. The positive ion is then attracted to the cathode by the strong electric field present, the cathode is typically made from titanium as it a very chemically active surface. Upon collision with the cathode the gas can be pumped by one of two typical methods. Firstly, the species can be a reactive gas that forms a stable chemical species with titanium, or secondly it can be physically buried in the cathode as is the case for noble gases such as argon. Many advances have been made to improve the efficiency of pumping for noble gases, one main approach is changing the geometry of the cathode such that ions impact the surface at shallow grazing angles providing higher pumping speeds for noble gases [5].

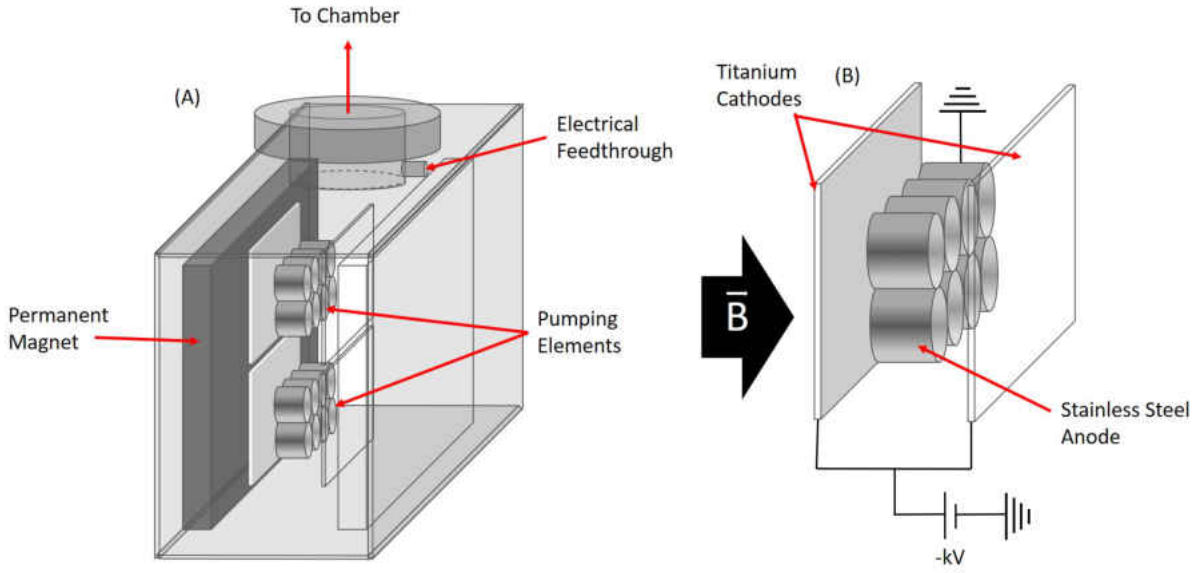

FIGURE 2.4: (A) shows the general shape of an ionization pump, externally the main connection is a single high-voltage feedthrough. (B) shows a single pumping element of an ion pump with the cathode and anode indicated.

Ion pumps, like turbo and diffusion pumps require vacuum prior to start up. This typically requires that a turbo pump is used to achieve initial vacuum pressures before an ion pump can be used. Ion pumps have a number of key factors that make them

very useful, the first being they consist of zero moving parts and as such can maintain UHV conditions for systems that require complete vibration isolation. They also have quite high pumping speeds making them very efficient, and finally are typically self-serviceable, in that new pumping elements can be easily exchanged withing the pump, although due to the large heavy magnets present they tend to be difficult to move.

2.3 Gas Handling systems

2.3.1 Gas-Line

Introduction of gases into the vacuum system is typically handled by a gas-line system depicted in Figure 2.5. The gas-line is constructed mainly from Pyrex gas with the exception of locations where Swagelok valves are attached requiring glass to metal transitions. It is pumped down by a combination of mechanical and diffusion pumps and is capable of reaching base pressures of $\sim 1 \times 10^{-6}$ Torr.

As seen in Fig. 2.5 the typical gas-line features a number of available connections through Swagelok valves to gas or liquid sources for introduction to the UHV chamber. Teflon valves are used to isolate different sides of the gas-line allowing the presence of two gases in the line simultaneously, for instance argon and oxygen required for crystal cleaning. Introduction of gases into the chamber is done by means of a variable leak valve that allows for precise control over the leak rate. The pressure of the gas-line when at pressures greater than $\sim 1 \times 10^{-3}$ is measured by a diaphragm manometer, and is used to monitor pressures when filling the line from a gas cylinder. A cold-cathode gauge is used to monitor the base pressure of the line when pumped by means of the diffusion pump.

The gas-line also provides a means to purify samples through a technique known as freeze-pump-thaw. Briefly, a gas sample vial containing a liquid to be purified is

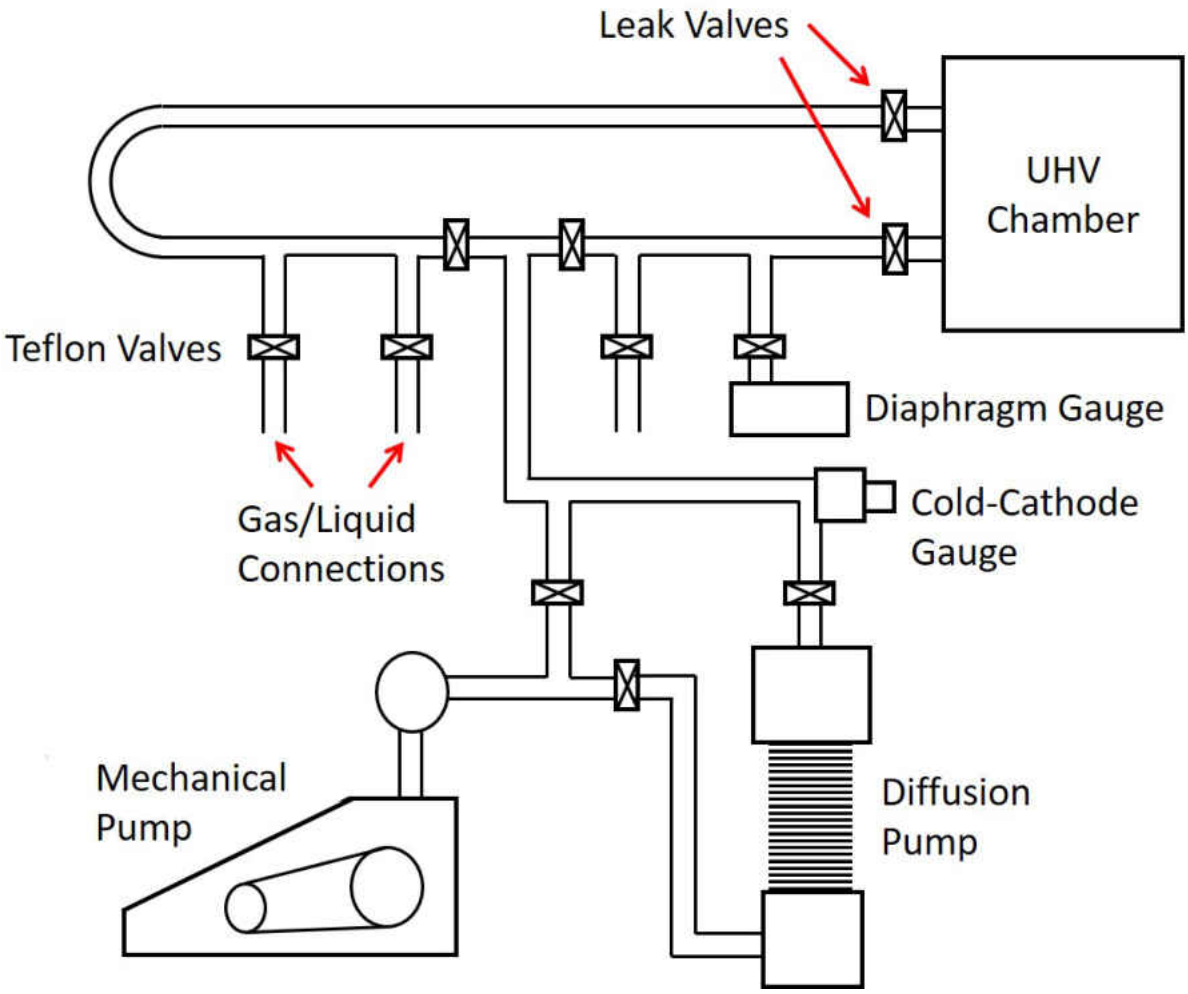

FIGURE 2.5: Diagram of typical gas-line system pumped by mechanically backed diffusion pump, allowing for introduction of gases to vacuum chamber.

submerged in liquid nitrogen until frozen solid, at which point the valve to the gas-line is opened to pump on the sample and the liquid nitrogen is removed. During the thaw dissolved gases and other contaminant present in the sample with greater vapor pressures sublimate first and are pumped away. This process is generally repeated until the formation of bubbles is no longer observed during the thawing process.

2.3.2 Knudsen Source

In order to introduce molecules that have sufficiently low vapor pressures, home built Knudsen sources are constructed as shown in Figure 2.6. They are assembled utilizing two $2\frac{3}{4}$" flanges that have welded $\frac{1}{4}$" stainless steel tubes through the center. The tubes on either side are then connected to $\frac{1}{4}$" Swagelok valves and, each side is connected in the center by a T, where the sample vial or holder can be affixed. It should be noted that great care must be taken during assembly to follow manufacture specified tightening of Swagelok connections as they are not intended for use in UHV and are therefore unfortunately prone to leaking.

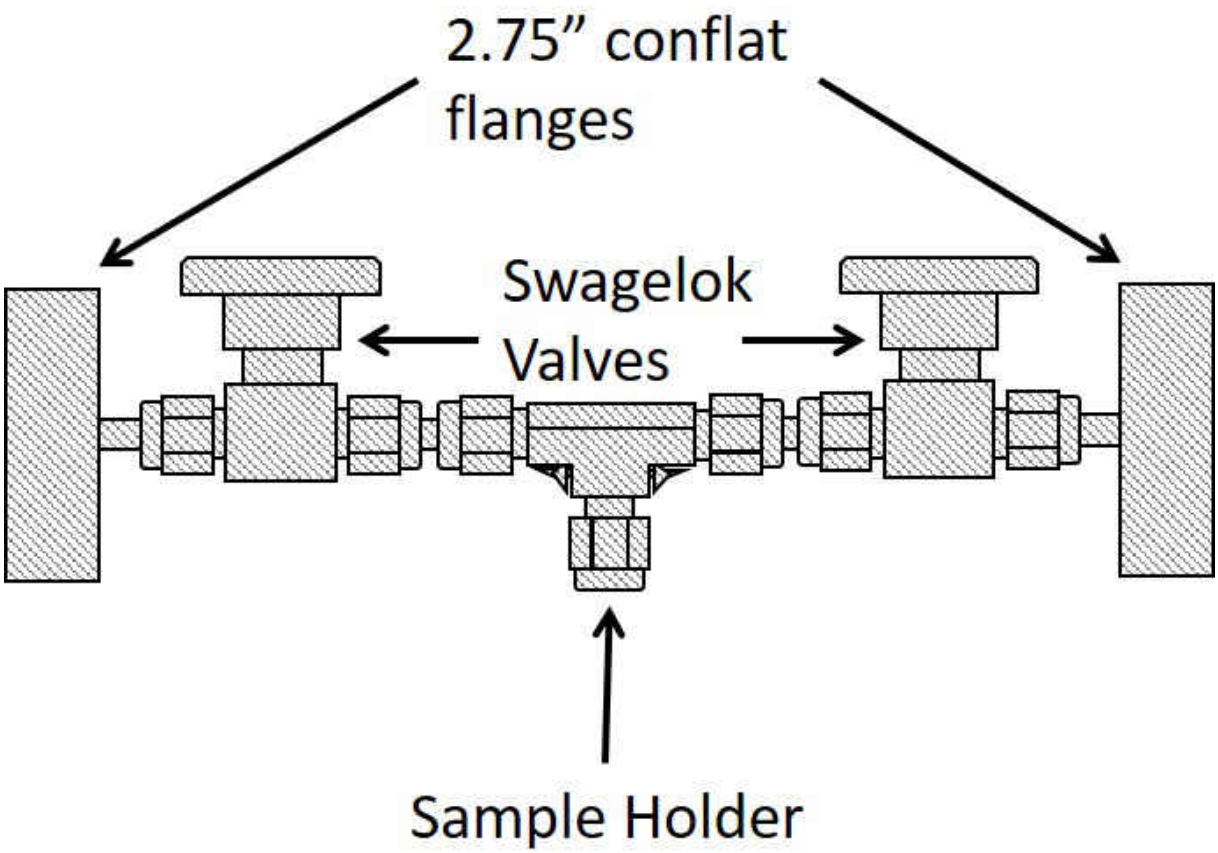

FIGURE 2.6: Diagram of Knudsen source used to introduce low-vapor-pressure compounds into UHV.

During use the Knudsen source is pumped by means of a turbo pump though one of the Swagelok valves to reduce the pressure of the system, while the valve connected to the chamber is closed until gas exposure is desired. Depending on the particular application the sample can be affixed though either a glass vial, or commonly for solid samples placed directly in a blank Swagelok connector. The use of a glass vial allows samples to be cooled by means of submersion in an ice or cryogenic bath allowing the control of vapor pressure and therefore exposure. As an alternative for compounds with extremely low-vapor-pressure the use of a blank for solid samples allows for the entire Knudsen source to be wrapped with heating tape allowing for another avenue to control the vapor pressure of the particular sample.

2.4 Vacuum Chambers

The construction of modern UHV systems utilizes stainless steel for the large majority of its components since it provides both a low outgassing rate and ease of fabrication [6]. A typical vacuum chamber body is outfitted with a number of standard flanges that can be used for the attachment of instrumentation. Shown in Figure 2.7 is a top down view of the UHV chamber used for electrical measurements of gold nanoparticle arrays. This particular chamber was pumped by the combination of turbo, and ion pump to reach a base pressure of $\sim 1 \times 10^{-8}$ without baking.

In order to achieve UHV conditions flanges are connected by means of a Conflat connection which utilizes oxygen free copper gaskets between the two sides of a flange machined with a knife-edge, creating a UHV suitable seal. The use of common flange sizes allows for enormous customization of UHV chambers to meet the particular needs of the experimenter. In order to reach UHV conditions it is required that vacuum chambers be "baked" referring to heating of the chamber to a consistent $\sim 120\ ^{o}$C for a period of $\sim$ 36 hours. This process is used to drive off adsorbed water

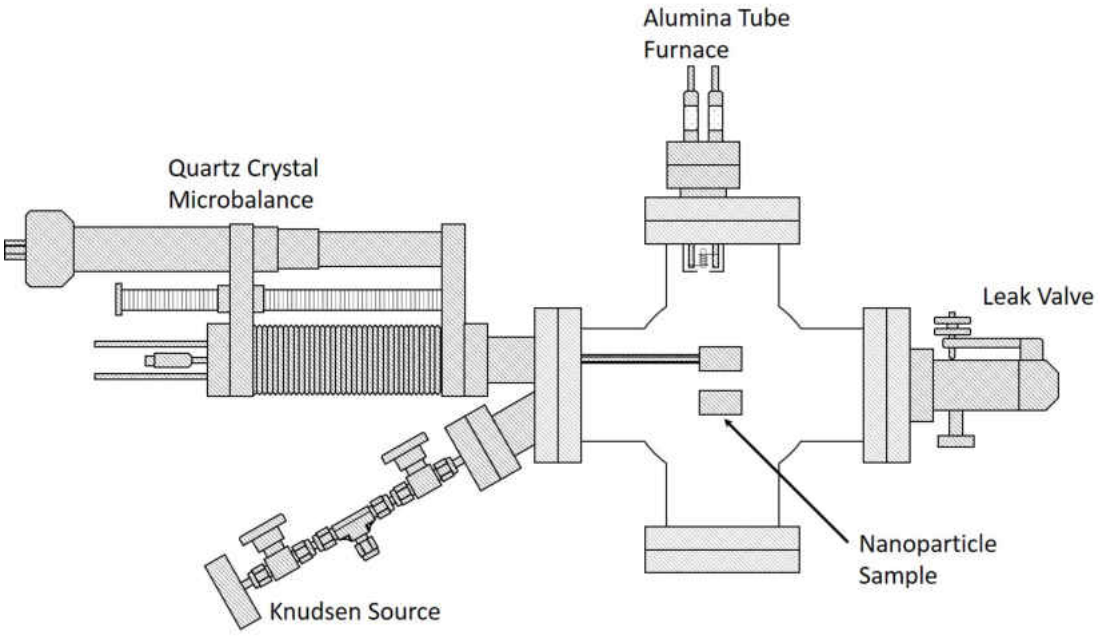

FIGURE 2.7: Top down schematic of the vacuum chamber used for electrical measurements of nanoparticle samples, not shown are vacuum pumps and sample manipulator.

that is the result of a chamber being open to air. To reduce adsorbed contaminants it is also advised that a chamber be vented using liquid nitrogen introduced through a leak valve, the use of liquid nitrogen ensures the vacuum chamber does not become over pressurized. Once a chamber has reached UHV conditions it can generally maintain those pressures for as long as needed, with the exemption of particularly harsh experiments that may require periodic baking to return to UHV conditions.

Bibliography

[1] R.Nave. Meanfreepath,http://hyperphysics.phy-astr.gsu.edu/hbase/kinetic/menfre.html, 2018.

[2] Trevor A Delchar. *Vacuum physics and techniques*. Chapman and Hall, 1993.

[3] *Owner's Manual for Duoseal Vacuum Pump Model 1400 and 1392*.

[4] Wikimedia Commons. Turbo molecular pump, 2005.

[5] *Ion Pump Operation and Trouble Shooting Guide*.

[6] G Lee. Materials for ultra-high vacuum. *NASA STI/Recon Technical Report N*, 90, 1989.

Chapter 3

Experimental and Theoretical Methods

3.1 Experimental Techniques

3.1.1 Current/Voltage Measurements

In order to measure current-voltage characteristics of molecularly linked nanoparticle arrays we employ the use of a Labview controlled National Instruments analog to digital (A/D) converter card. The Labview software is used to generate a ramped voltage over a range specified by the user, where the maximum voltage is ± 10 V. The voltage output from the A/D card is applied to the sample by means of flange outfitted with multiple BNC feedthroughs. The current through the sample is then measured by connecting another BNC feedthrough to a Keithley picoammeter that can produce an output voltage corresponding to the measured sample current. This output voltage is then feed back into the A/D card and is then plotted against the applied voltage in the Labview software. A block diagram showing the connection scheme for current/voltage measurement is given in Figure 3.1. In order to acquire low noise measurements two main approaches are taken, the first method being a user adjustable averaging function present in the I/V software. Secondly, the utilization of shielded BNC cables, and careful grounding of the measurement assembly is necessary in order to acquire low noise measurements.

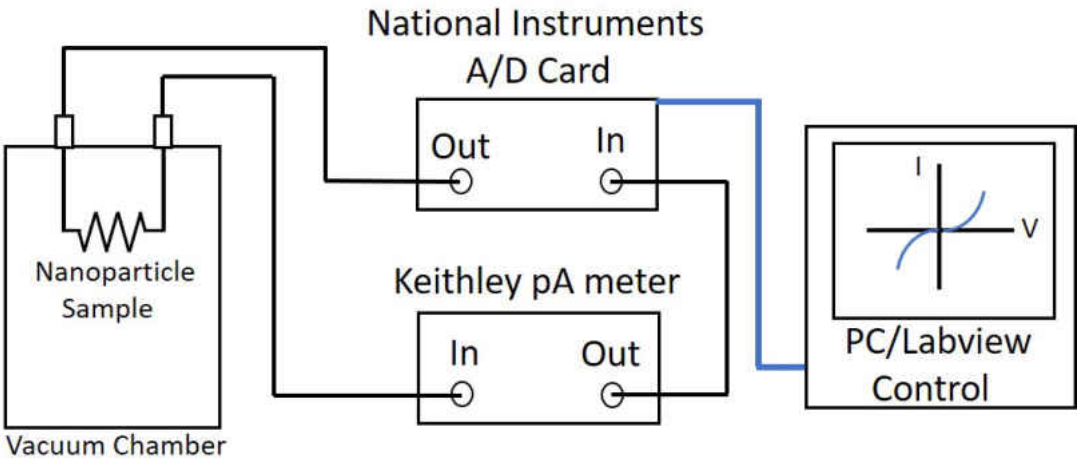

FIGURE 3.1: Block diagram of I/V curve measurement assembly. A Labview controlled national instruments A/D card is used to generate a ramped voltage applied to the nanogap samples, the current is measured by a Keithley picoammeter, a corresponding voltage is fed back into the A/D card and plotted in Labview.

Connection to the nanoparticle arrays prepared on silica required the construction of a specialized sample holder shown in Figure 3.2 which allowed for electrical isolation of the sample, was fabricated in the UWM machine shop. The sample holder was constructed in two halves, one is responsible for physically holding the sample while the lower half could be outfitted with a coiled heating element, or allowing a thermocouple connection to the base of the sample. The nanoparticle arrays were held in place between two sapphire washers using spring clips isolating them from the body of the sample holder, Kapton wires connected to the arrays were then feed through the feedthroughs indicated in Fig. 3.2. The sample holder is also connected physically by copper rod to a liquid nitrogen reservoir allowing the arrays to be cooled to $\sim$100 K and the temperature dependent conductivity to be measured.

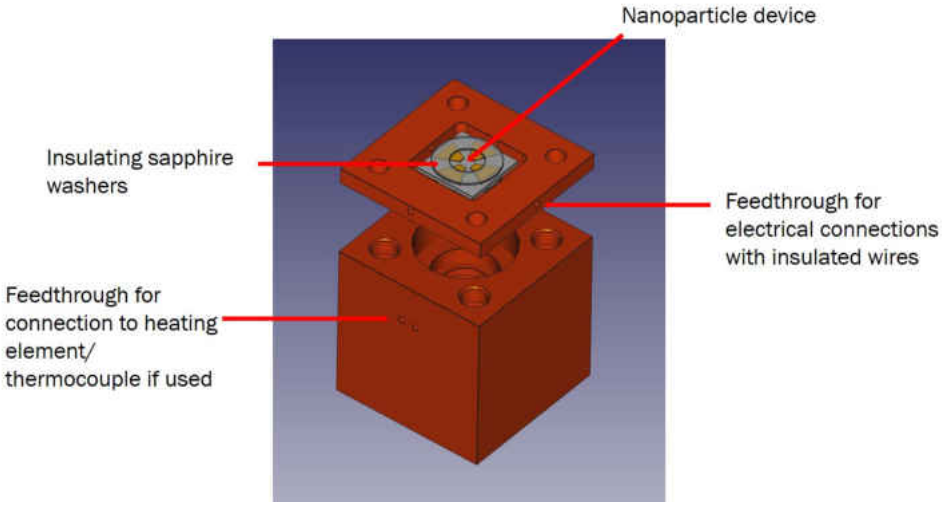

FIGURE 3.2: Sample holder fabricated for electrical measurements of nanoparticle arrays on silica, allowing for both cooling and heating of the arrays. The silica sample is sandwiched between two insulating sapphire washers, and insulated wires are connected through the sample holder then connected to BNC feedthroughs.

3.1.2 Scanning Electron Microscopy

The scanning electron microscope (SEM), originally developed in 1958 by Everhart and Thornley [1], has become one of the most widely used imaging technologies utilized by a variety of disciplines. Its necessity arises from the limitations of optical microscopy, in that the wavelength of light determines the ultimate resolution. The SEM surmounts this obstacle by using electrons as a structural probe, whose wavelength and therefore resolution can be tuned by changing the kinetic energy. For example a 10 kV electron (commonly used for nanoparticle imaging in the following work) will have a wavelength on the order of 10 pm, much smaller than that of visible light.

The working principle of a SEM is depicted in Figure 3.3, where electrons generated by an electron gun are accelerated to the desired kinetic energy by a potential applied to the anode. Following acceleration, the electrons will travel through a series of electromagnetic lenses that serve two purposes, the first being the primary focusing of the electron beam, and secondly though signals sent from a computer control, generate a

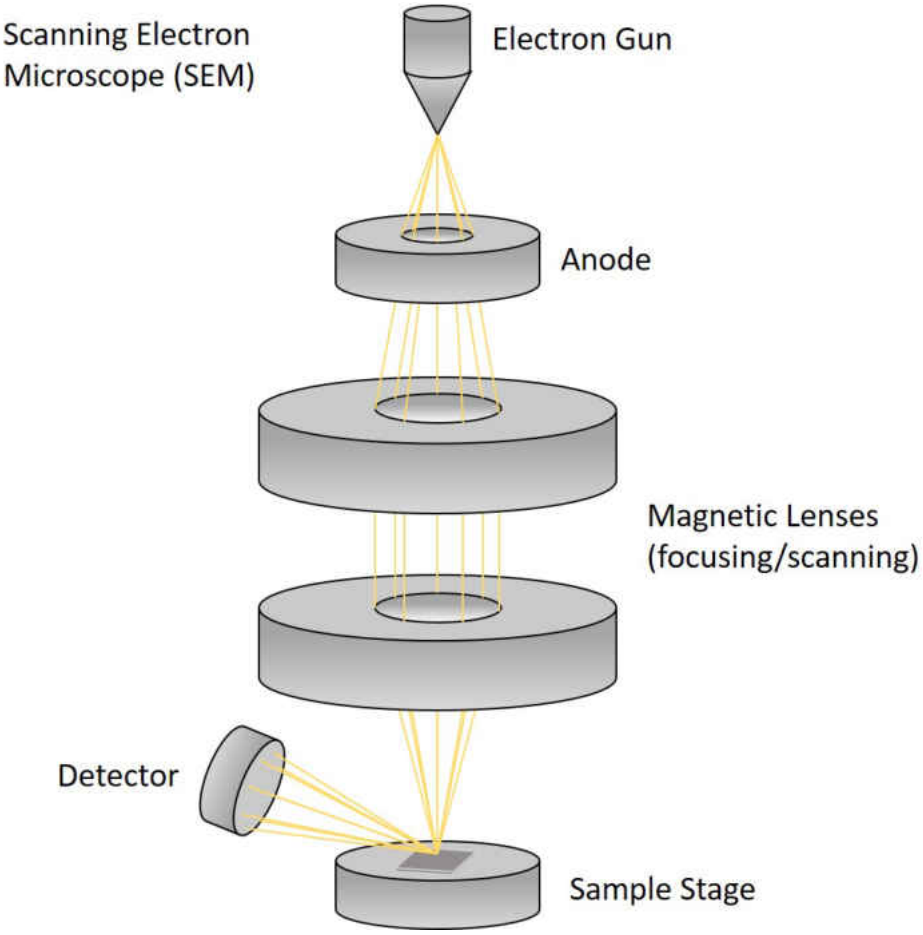

FIGURE 3.3: Working principle of a SEM, electrons are generated by an electron gun and focused through a series of magnetic lenses to a point on the sample, where backscattered and secondary electrons are detected.

raster scan over the sample. The focused electron beam can then interact with the sample in a number of ways. However, primarily used for imaging are backscattered, and secondary electrons ejected from valance bands of the scanned sample that are then detected by an electron detector and used to generate an image.

3.1.3 Temperature-Programmed Desorption

Temperature-programmed desorption (TPD) also known as thermal desorption spectroscopy (TDS) is a technique widely used to study the desorption of adsorbates from surfaces, TPD can thus provides us with fundamental information on the strength of

the adsorbate bond with the substrate. In TPD, compounds are dosed at low temperatures onto the surface of the substrate through either a variable leak valve or from a Knudsen source, the sample is then heated in a controlled manner typically at a linear rate, desorption of the species is then monitored by means of a quadruple mass spectrometer. In addition to simple desorption, reactions on surfaces can be studied by following decomposition or reaction products using TPD.

Desorption of adsorbate species is an activated process that follows Arrhenius behavior, and according to the Polanyi-Wigner equation, the rate of desorption can be written as follows,

$$r_d = -\frac{d\theta}{dt} = v\theta^n \exp\left(\frac{-E_d}{k_b T}\right) \tag{3.1}$$

where r_d is the rate of desorption, v is the frequency factor, θ is the coverage of the adsorbate species, E_d is the activation energy of desorption, k_b is the Boltzmann constant, and T is the absolute temperature. During a TPD experiment the temperature is raised, thereby causing a constant increase in the rate of desorption, however during this process the coverage of surface species decreases. It is these two effects that give rise to peak observed by TPD and can be seen in Figure 3.4.

We can then derive a useful approximation that allows for an estimation of desorption activation energies from the peak temperature. The derivation begins by taking into account the fact that we are using a linear heating rate $\beta = \frac{dT}{dt}$ which can be incorporated into equation 3.1

$$\frac{r_d}{\beta} = -\frac{d\theta}{dT} = \frac{v\theta^n}{\beta} \exp\left(\frac{-E_d}{k_b T}\right) \tag{3.2}$$

considering now that at the peak temperature $(T = T_p)$ of the desorption profile the derivative with respect to dT of 3.2 can be set to 0, allowing us to obtain

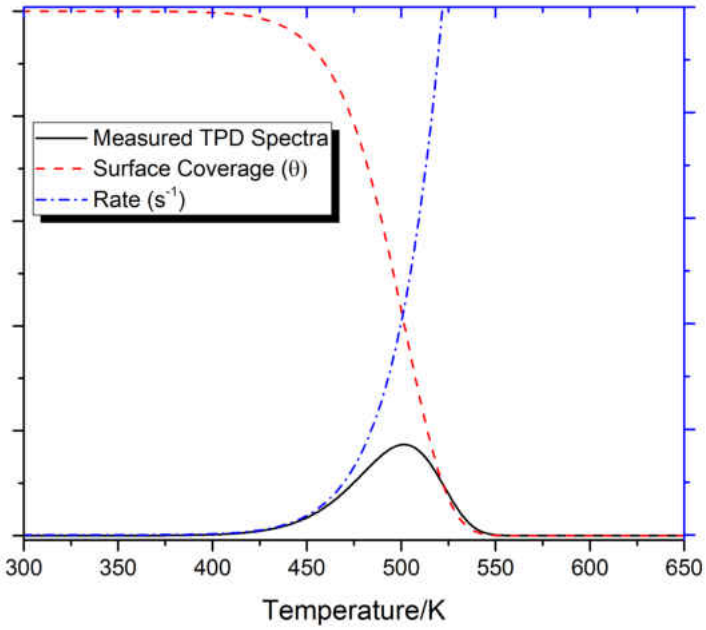

FIGURE 3.4: Origin of observed peak in TPD spectra.

$$\frac{d^2\theta}{dT^2} = 0 = \frac{v}{\beta}\left(\frac{\theta^n E_d}{k_b T^2}\exp\left(\frac{-E_d}{k_b T}\right) + n\theta^{n-1}\frac{d\theta}{dT}\exp\left(\frac{-E_d}{k_b T}\right)\right) \tag{3.3}$$

If we now assume that we are dealing with a first-order process (in which $(n = 1)$), as well as substituting into equation 3.2, we can obtain the following relationship

$$\frac{E_d}{k_b T^2} = \frac{v}{\beta} exp\left(\frac{-E_d}{k_b T}\right) \tag{3.4}$$

We can observe an important point from equation 3.4 in that, for a first order desorption process, the peak temperature does not depend on θ, and is therefore independent of the initial coverage of adsorbates on the surface. A empircal solution for equation 3.4 was obtained in 1962 by Redhead [2] which is now referred to as the Redhead equation,

$$E_d = k_b T ln\left(\frac{vT_p}{\beta}\right) - 3.64 \tag{3.5}$$

The Redhead equation provides a way to calculate an approximation of the desorption energy from just the peak temperature, in which we also need to assume that the desorption process is first order, and that the value of v the frequency factor is $\sim 10^{-13}$. Although there can be errors associated with the use of equation 3.5, it nonetheless provides us with a reasonable estimate for the activation energy of desorption.

An alternative approach toward obtaining more accurate values for the desorption energy is the use of simulated TPD spectra, which can be obtained through numerical integration of equation 3.1. In general an estimation of the desorption energy is needed and can be obtained through the use of the Redhead equation or DFT calculations. Parameters such as the initial coverage, and frequency factor can then be adjusted in order to obtain reasonable fits to the experimental data. In addition to providing a more accurate method for the determination of kinetic parameters in experimental data, it also provides a way to become familiar with the effects the parameters have on both peak shape and temperature.

The spectra shown in Figure 3.5 were simulated using the parameters from reference [3] using the TPD simulation program (included in Appendix A) used in later chapters to fit experimental data. A number of important observations can be made by simply observing a desorption spectra, and familiarity with them can provide insight in to the processes occurring on the surface. One of the most informative aspects of a desorption profile is the peak shape as it can indicate the reaction order for the process being observed as shown in Figure 3.5A,B where a first order process for instance a simple decomposition will have an asymmetric peak shape that is independent of coverage. However, a second order process displays a symmetric peak shape along with a shifting to lower temperature with increasing coverage.

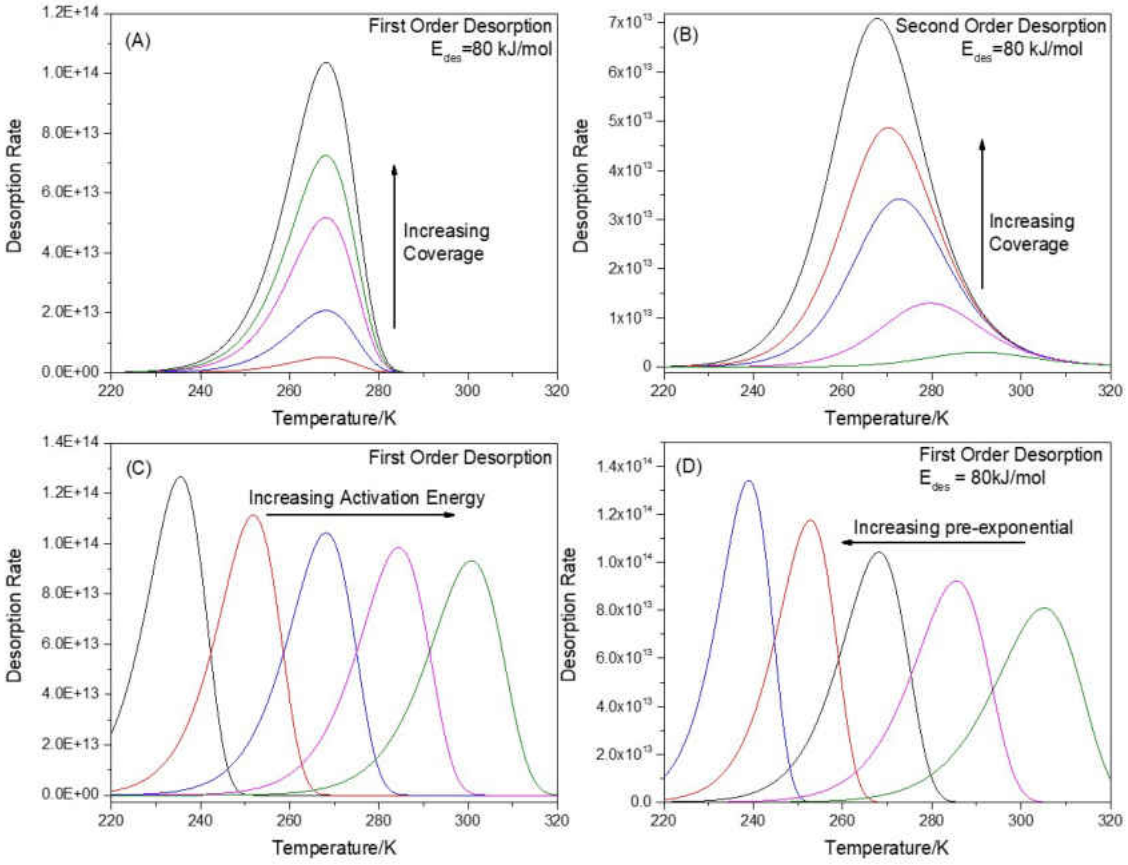

FIGURE 3.5: Figure A. shows the effect of increasing coverage on a first-order desorption profile, B. shows the effect of increasing coverage for second-order desorption, figures C, D show the effect of increasing activation energy and pre-exponential factor for a first-order desorption process.

3.1.4 Scanning Tunneling Microscopy

Introduction

Following the development of the scanning tunneling microscope (STM) in 1982 by Gerd Binning and Heinrich Roher [4,5] the pair were awarded the Nobel Prize in 1986. The STM quickly became an indisposable tool for the imaging and characterization of surface structure, and is now a key instrument in many surface science laboratories. Initially used as a means to observe only the structure of surfaces the STM has continued to develop an is now applied in the study of high pressure catalysis [6], most

recently with the use of radiation from a synchrotron light source STM was capable of directly identifing chemical signature [7, 8], finally another great advance is fast-scanning STM in which entire images can be recorded on the time scale of a second and can be used to study diffusion on surfaces [9]. STM continues to be an incredibly useful tool in the surface sciences and is continually increasing its capabilities in the field.

Theory

According to classical physics a particle approaching a potential barrier should only be able to pass though the barrier should it have kinetic energy greater than the potential of the barrier. However, due to the quantum nature of the electron it is able to penetrate such a potential barrier with a non-zero probability allowing for the measurement of a tunneling current which is the essence of STM and is depicted in Figure 3.6.

In the case of a particle approaching the potential barrier from the left, we can define the wave functions in the three regions as follows,

$$\psi_I = a_1 e^{ik_1 x} + b_1 e^{-ik_1 x}, \psi_{II} = a_2 e^{k_2 x}, \psi_{III} = a_3 e^{ik_3 x} \tag{3.6}$$

where we can define the wave vectors of the given wave functions as

$$k_1 = k_3 = \frac{\sqrt{2mE}}{\hbar} \ \ and \ \ k_2 = \frac{\sqrt{2m(V_0 - E)}}{\hbar} \tag{3.7}$$

We can then utilize the fact that the wavefunction and its first derivative are continuous to solve respective amplitudes of the given wavefunctions. This will allow for the calculation of the transmission coefficient $T(E) = \frac{|J_t|}{|J_i|}$ where J is the probability current of the transmitted and incident wave functions respectively, and is defined as

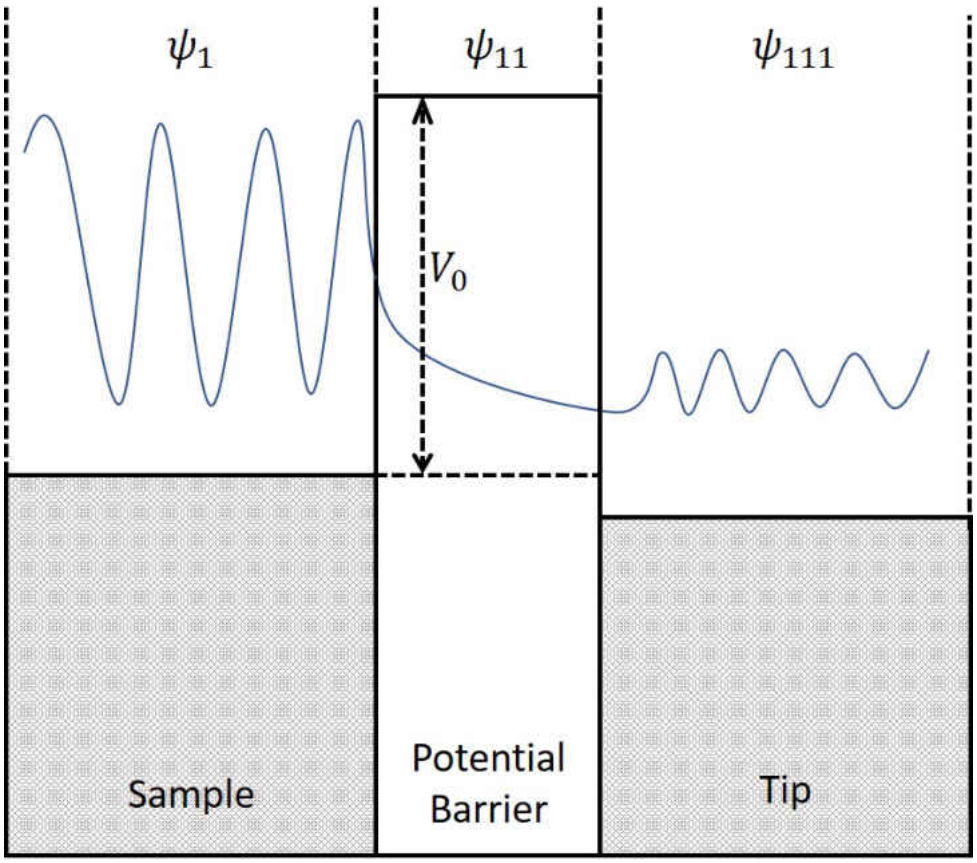

FIGURE 3.6: Tunneling of electron through a potential barrier; ψ_1 represents the wave function of the electron approaching the barrier, ψ_{11} the electron in the barrier, and ψ_{111} the electron after tunneling through the barrier.

$$\vec{J} = \frac{\hbar}{2mi}\left(\psi^* \frac{\partial}{\partial x}\psi - \psi \frac{\partial}{\partial x}\psi^*\right) \tag{3.8}$$

Solving the equations at the boundaries ($x = 0$,and $x = L$) and calculating the transmission coefficient for the given wave functions we obtain,

$$T(E) = \frac{1}{1 + \left(\frac{k_1^2 + k_2^2}{2k_1k_2}\right)\sinh^2(k_2L)} \tag{3.9}$$

The resulting transmission coefficient can be further simplified to the following $T(E) \propto exp\left(-2L\sqrt{\frac{2m(V_0-E)}{\hbar}}\right)$ [10] which is proportional to the tunneling current from

electrons penetrating the barrier. Although this is a simplified one-dimentional approximation it demonstrates a very important point in that the tunneling current measured by STM is exponentially dependent on the separation between the tip and the sample. In typical operation this requires that the tip be positioned on the order of a few Angstroms from the sample surface. Displacements of this order rely on the use of precision piezo electronic legs, capable of moving laterally and vertically by fractions of an Angstrom.

Application

There are a number of other very important factors that play a role in obtaining high quality images by STM including, but not limited to vibrational isolation, and fabrication of ideally atomically sharp tips. The first of these factors is addressed largely by the fact that entire instrument is mounted on air legs that can be inflated to suspend the chamber greatly dampening vibrations. Additionally, during an experiment vacuum is maintained though the use on only ion pumps, and all unnecessary connections to the chamber are removed. Typically, STM chambers are also locate in basement laboratories adding an additional stage of vibration isolation to the instrument.

The fabrication of atomically sharp tips is addressed by the use of electrochemical etching of tungsten wire, and the application of the drop off technique [11, 12]. Briefly, in this technique a tungsten wire, preferably single crystalline is placed through a ring shaped gold, or platinum electrode, one end of the wire is then place in a concentrated NaCl solution, the other held by a small chuck. Filling the small ring shaped electrode with 1-2 M KOH (or NaOH) such that the droplet is held in the ring forming a thin film around the tungsten wire, allows for a voltage to be applied (3-4 Volts) between the tip and the ring electrode resulting in the following electrochemical reaction.

Cathode: $6\,H_2O + 6\,e^- \longrightarrow 3\,H_2 + 6\,OH^-$

Anode: $W(s) + 8\,OH^- \longrightarrow WO_4^{2-} + 4\,H_2O + 6\,e^-$

Overall: $W(s) + 2\,OH^- + 2\,H_2O \longrightarrow WO_4^{2-} + 3\,H_2$

The drop-off techniques' usefulness comes from the fact that the tungsten tip effectively acts as a switch in the system, the moment the tip is etched through, the circuit becomes open, immediately stopping the etching process. This is key to obtaining atomically sharp tips for scanning, as any further etching would reduce the sharpness of the tips apex. Figure 3.7 displays the three stages of the tip etching process using the drop off method, firstly it is very important that droplet forms a very thin film around the tungsten wire shown in the first image. The second image shows the wire after some time of etching, during the process it can be seen that the process begins to slow and the bubbles produced will begin to decrease. At this point the initial droplet should be dried, and replace with fresh solution for the final etching. The voltage is then reapplied until the drop off occurs, the tip should then be visually inspected for any clear signs of damage to the apex. Upon passing the visual inspection the prepared tip can then be transferred into vacuum and tested in the instrument.

FIGURE 3.7: Three stages of the tip etching process, the first shows early stages of etching, in the second, clear etching of the tungsten wire can be observed, and finally after the lower wire has fallen.

The importance of a sharp tip for high-resolution STM is depicted in Figure 3.8, which shows a STM tip scanning over an atomic step. As described earlier the tunneling current between the tip and sample is the origin of the images obtained by STM, in the case of a large STM tip (Fig. 3.8A) the local area contributing to the tunneling current is much larger resulting in reduced resolution over such features. However, for a nearly atomically sharp tip (Fig. 3.6B), the localized tunneling area is largely reduced allowing for greatly improved lateral resolution. It is for this reason that a great amount of work has gone into the fabrication process of atomically sharp STM tips.

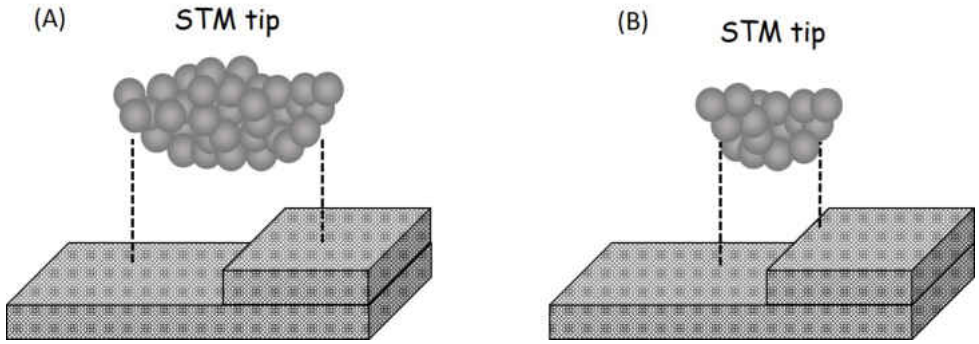

FIGURE 3.8: Importance of tip sharpness, in (A) there are tunneling contributions from a larger area reducing resolution, whereas in (B) a sharp tip results in more localized tunneling contribution.

3.1.5 Reflection Adsorption Infrared Spectroscopy

Introduction

Infrared spectroscopy is a very common and well established means of obtaining chemical information through the use of infrared radiation. The technique traditionally applied to gases, liquids, and thin films can also be extended to probe adsorbed layers on surfaces which is referred to as Reflection Adsorption Infrared Spectroscopy (RAIRS) the details of which will be discussed below. The working principle of IR spectroscopy is the absorption of IR radiation by molecules having a net dipole moment, allowing

the access of different vibrational energy levels depending on the specific energy of the radiation. Due to the selective absorption of radiation due to molecular composition we can utilize IR spectroscopy to determine chemical structure, and through the use of RAIRS with the surface selection rules, molecular orientation on a surface.

Surface Selection Rules

A key aspect of RAIRS is the fact that a set of surface selection rules apply to vibrations that are allowed to be observed that differ from gas- and liquid-phase IR. The first of these rules arises from the fact that a metal surface can only support an electric field perpendicular to its surface, this is a result of the image dipole effect that forms in a metal surface. Because of this, on a metal surface only vibrational modes with a dipole component normal to the surface will be active and therefore visible in RAIRS [13]. This is depicted in Fig 3.9 in which (A) depicts a parallel dipole that is canceled by the image dipole of the surface, and (B) which show an IR active perpendicular dipole that can will be enhanced by the image dipole of the surface.

The second component arises from the metals interaction with different polarizations of radiation. Historically RAIRS suffered from very low signal coming from both the small amount of sample present in an adsorption experiment, and absorbtion of radiation by the substrate. This was investigated theoretically in 1966 by Greenler [14] which indicated that for greatest IR signal p-polarized radiation should be used at a grazing incidence to the sample. This can be understood by considering the electric fields that would be produced by the the IR beam on a clean metal surface, this is depicted in Fig 3.10. It can be seen that, for any angle of incidence, the resulting electric field from s-polarized radiation is near zero due to a near 180^o phase shift, and therefore does not interact strongly with surface dipoles. Although p-polarized light also suffers a phase shift it can be seen that the resulting electric field perpendicular

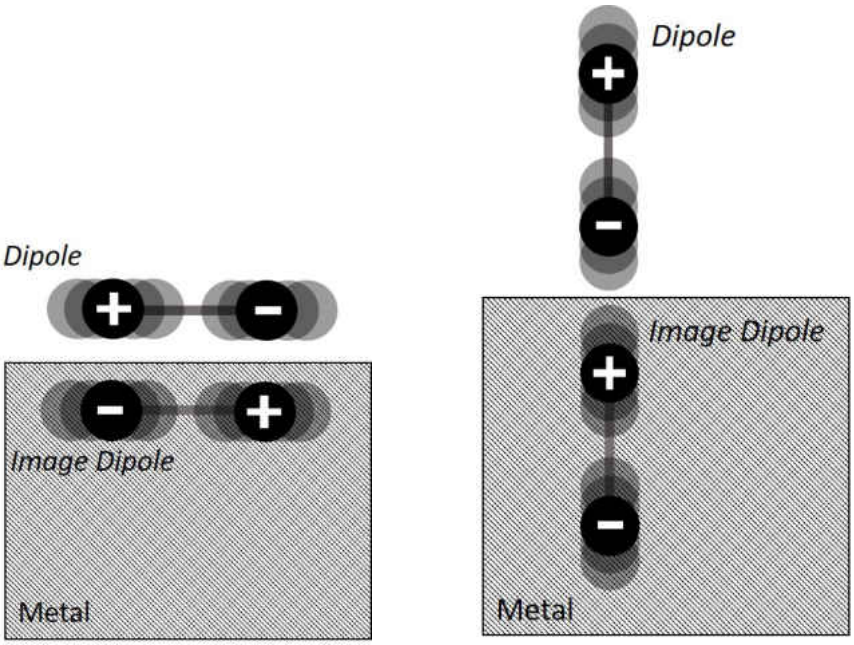

(A) Canceled parallel dipole. (B) Allowed perpendicular dipole.

FIGURE 3.9: Illustration of the image dipole effect.

to the surface can be nearly doubled at a grazing incidence, and can therefore interact strongly with a perpendicular surface dipole. If we then assume that the absorbance will be proportional to the square of the electric field at the surface, ${E_p}^2$, we can see that this will increase as $1/cos(\theta)$ where θ is the angle between the incident radiation and the surface normal. We can then conclude that the absorbance will be proportional to ${E_p}^2/cos(\theta)$, and this function is sharply peaked at grazing angles clearly demonstrating the importance of a high angle of incidence [15]. We can see that both photon dipole and electron dipole interactions play a role in the surface selection rules. Although certain dipole moments may be invisible to RAIRS, the surface selection rules more often than not yield detailed information into the geometry of adsorbed species on a surface.

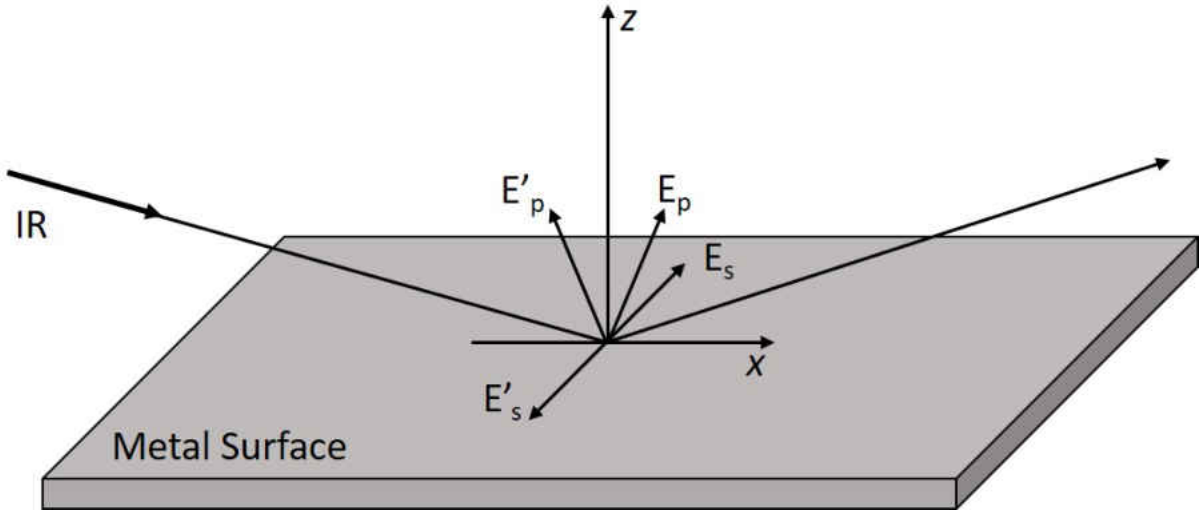

FIGURE 3.10: Diagram of electric field vectors produced from an IR beam striking a metal surface at a grazing incidence.

Application

In order to collect RAIRS spectra we utilize a commercially available bench top Fourier transform infrared (FTIR) spectrometer (Bruker Vertex). The light path from the spectrometer is completely enclosed in plexiglass boxes which are continually purged with dry air in order to largely reduced absorbance by atmospheric water and carbon dioxide thereby greatly improving the spectra. In the light path, the sample (in this work a Au(111) single crystal) is located in a 6-way gold-plated cell connected to a UHV chamber, with opposing KBr windows allowing transmission of IR radiation. Prior to probing the sample surface the IR beam is deflected by a number of gold- plated mirrors before passing though a polarizer perpendicular to the surface of the sample, finally after reflection the beam is detected by a liquid nitrogen cooled mercury cadmium telluride (MCT) detector. The sample is connected to a transfer arm allowing for movement into the UHV chamber for sample preparation. In addition, liquid nitrogen can be flowed through the transfer arm allowing experiments to be conducted at temperatures down to $\sim$90 K. In a typical kinetic study used to investigate either uptake,

or the effects of heating, spectra are recorded at a rate of 1/min yielding $\sim$ 350 scans at 4 cm^{-1} resolution which are the conditions applied in experiments carried out in this thesis.

3.2 Theoretical Techniques

3.2.1 Monte Carlo Simulations

Introduction

The essence of a Monte Carlo simulation is the application of random numbers generated during a simulation, which allow for the modeling of processes that proceed by a stochastic manner. This approach can be accurately applied to a number of natural phenomena such as percolation of a lattice, and Brownian motion [16]. In the past, the application of Monte Carlo simulations was largely restricted by computational power, as the working principle of Monte Carlo is inherently computationally expensive. With the growth in computing power, and sophisticated programming techniques the applications of Monte Carlo simulations has also grown. In this thesis, we investigate the self-assembly of PDI, the stochastic nature makes it an ideal system to be simulated by Monte Carlo.

Theory

In the simulations described in later chapters we use a lattice gas model, where the surface is represented by an array of $N = L \times L$, where L is the linear size of the array. Periodic boundary conditions are imposed to represent an infinitely large system. Each site can be occupied by a monomeric unit, where the monomeric unit is also given a value of an alignment parameter corresponding to one of the three surface directions.

In the following, fixed, low-coordination growth nucleation sites will be referred to as nodes or nodal points. As will be seen later, the nodes have a remarkable influence on the resulting self-assembled structures. In our model, the interaction of nodal points with Au-PDI monomers is considered to be attractive and to occur only in the direction of the axis determined by alignment parameter of the monomer. Then, the adsorbed phase, in the canonical ensemble (at fixed coverage), is characterized by the following Hamiltonian:

$$H = -w\sum_{i,j} int\{|\vec{r}_{ij}\cdot\vec{s}_j||\vec{r}_{ji}\cdot\vec{s}_i|\,(1-c_i)\,(1-c_j)\} \\ - w\sum_{i,j}\left[int\{|\vec{r}_{ij}\cdot\vec{s}_j|\,(1-c_j)\,c_i\} + int\{|\vec{r}_{ji}\cdot\vec{s}_i|\,(1-c_i)\,c_j\}\right] \quad (3.10)$$

Here, the sums are over pairs $\langle i,j\rangle$ of nearest-neighbor (NN) sites; the occupation of one site by the Au-PDI monomer is described by the vector $\vec{s}_i = \{0, \vec{x}_k\}$, which takes the value 0 if the site is empty and $\vec{x}_k$ if it is occupied, giving as well the orientation of the monomer in one of the k directions of the lattice; $\vec{r_{ij}}$ is the vector connecting site i with the site j; the node occupation variable is given by, $c_i = 0, 1$, where c_i takes the value 0 when the site does not have a nodal point; w represents the lateral interaction between two adsorbed monomers located in two NN sites or the lateral interaction between a monomer and a NN node. In this model, the interaction between nods is not considered since they form a regular array and are far apart from each other. Thus, the first term on the right hand side of equation 3.10 represents the contribution of the Hamiltonian corresponding to particles located at sites i and j, which are nearest neighbors; sites may or may not be occupied by monomers, which have orientations given by $\vec{s}_i$ and $\vec{s}_j$ monomers contribute with energy w, if and only if both are oriented in the direction of the vector connecting the two sites $\vec{r_{ij}}$ or $\vec{r_{ji}}$; the final contribution is

0 or 1, due to the function int, which takes the integer part of this factor. Finally, the factor $(1 - c_i)(1 - c_j)$ avoids the presence of nodal points at both i and j sites.

The second term represents the contribution to the Hamiltonian due to a monomer located at site $j(i)$ and a nodal point located at site $i(j)$. Note that, in the absence of nodes, the model is the well-known rigid-rod model, which has been extensively studied by others. For more details on the self-assembled rigid-rod model, see [17] and references therein.

The growth kinetics have been investigated by means of a standard-importance sampling Monte Carlo method in the canonical ensemble. As mentioned above, the simulation lattice is a triangular array of $N = L \times L$ sites with conventional periodic boundary conditions. Thermodynamic equilibrium is obtained by following the Kawasaki dynamic [18]. As an initial configuration a fixed number of nodes can be located at random or in a regular array (in what follows, only regular arrays can be considered); then, a predefined number of monomers is added to the system in fixed intervals of Monte Carlo steps simulating a constant flux of 1,4-PDI. Initially, monomers modeling the adatom complex are randomly adsorbed on only edge sites of nodes, they are then allowed to diffuse randomly across the surface until they are adjacent another adatom complex or oligomer chain; if then selected randomly the species can then become, or add to an existing oligomer. Then, the system is allowed to reorganize itself based on the following rules. First, one of two possible events, migration or rotation, is chosen at random. For a migration event, an occupied site and an empty site are selected randomly, establishing its coordinates. Then, the difference between the energies of the final and initial states, $\Delta E = E_f - E_i$, is calculated; a random number ξ uniformly distributed in the interval $(0 \leq \xi \leq 1)$ is chosen, and compared with a probability $P = min[1, exp(-\beta \Delta E)]$, where $\beta = 1/k_B T$, and k_B is the Boltzmann constant; an exchange between the occupation of the sites is carried out if $P > \xi$, i.e., if the

probability P is larger than the random number ξ.

For monomer rotation, the rotational state of the selected monomer is changed following the same procedure described above. A final rotational state is considered, and the energy of the monomer is calculated. Finally, the energy change between the initial and final rotated states is computed. The new rotated state is accepted after considering the comparison between a random number and the probability as described above.

A Monte Carlo step (MCs) is defined as $N = L \times L$ attempts to change the state of occupation and rotation of a surface site. Typically, the equilibrium state is reached after $1x10^5$ MCs, as will be shown later. In order to simplify the comparison of interaction energies, we will assume a temperature of 298K. However, it should be noted that, given $\Delta E/k_BT$ term in the probability equation, when discussing changes in energy, this would be equivalent to inverse change in temperature.

3.3 Sample Preparation

3.3.1 Single Crystal Cleaning

In order to study ideal systems under UHV conditions, it is required that single crystal surfaces be free of surface contaminants. In general, this is done by a combination of surface bombardment, and annealing. However, reactive metals such as palladium require additional oxygen roasting cycles to remove surface bound carbon. The bombardment process is done by acceleration of argon ions toward the crystal surface using an ion gun, the resulting emission current is then measured and adjusted to the desired value in μA. This process effectively drives off surface impurities into vacuum, but leaves the resulting surface very rough. In order to return the smoothness of the surface, the crystal must be held at its annealing temperature for typically $\sim$30 min,

although this process varies depending on the specific metal. Included below are the common recipes for cleaning crystals used in labs.

Au(111)

Bombard with Ar^+ at a current of $\sim 2.0 \mu A$ with an acceleration voltage of 500V for a period of 30 min. Following bombardment the sample should be annealed for a period of 5 min at 620^oC (24 mV) followed by 30 min at 420^oC (16 mV). This procedure is repeated until cleanliness is observed by available techniques such as AES, or resolution of the Herringbone reconstruction with STM.

Cu(111),(100)

Bombard with Ar^+ at a current of $\sim 2.0 \mu A$ and acceleration voltage of 1 kV for a period of 30 min. Following bombardment anneal the sample at 650^oC (25 mV) for 30 min. Repeat procedure until AES or available technique confirms cleanliness of sample.

Pd(111)

Bombard with Ar^+ (1 kV) with a current of $\sim 4\ \mu A$ for a period of 30 min. Following bombardment the sample should be annealed at 1000 K for 5 min. The sample should now be heated between 740 K and 875 K while dosing O_2 at a pressure of $\sim 5 \times 10^{-8}$ for 30 min, adjusting the temperature in the given range during this time. After the 30 min the sample should be flashed to 1000 K, then allowed to cool to 550 K under O_2 at a pressure of $\sim 5 \times 10^{-8}$. The final two steps should be repeated until an O_2 TPD, or AES confirm cleanliness of the sample.

Fe(100)

Bombard with Ar^+ (0.5 kV) with a sample current of 4μA for 30 min. Following bombardment anneal sample to 22 mV (830 K) for 30 min. Great care must be taken not to exceed 36 mV (1100 K) due to a phase transition of the Fe single crystal.

3.3.2 Alumina Tube Furnace

In order to deposit gold nanoparticles in situ a alumina tube furnace was constructed as shown in Figure 3.11. A 2 $\frac{3}{4}$" power feedthrough is used which features two $\frac{1}{4}$" copper rods to which we affix 2 mm tantalum rods. A tungsten coiled alumina tube is then mounted to the end of the tantalum rods, into which gold wire is placed for deposition, although the same source can be used for a variety of metals. The furnaces can also be outfitted with a thermocouple for temperature measurement that can be placed in the back of the alumina tube. Deposition is done by resistively heating the furnace with a high current power supply connected to the external copper rods, for gold this typically requires about 15 A at $\sim$4 V applied, but this will depend significantly on the particular geometry of the source.

3.3.3 Quartz Crystal Microbalance

One of the most commonly used instruments for precision thin film thickness measurements is the quartz crystal microbalance (QCM). The operating principle of a QCM utilizes the piezoelectric properties of quartz, those being that a quartz crystal cut along a specific crystallographic direction possesses a specific resonance frequency when an appropriate alternating current is applied. It was found that a change in this resonance frequency Δf can be monitored and linearly related to a change of mass Δm by Equation 3.11 [19]

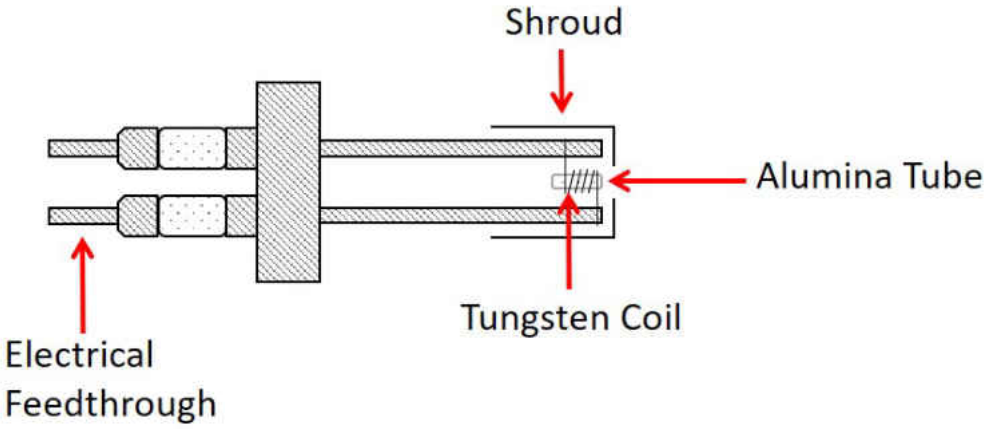

FIGURE 3.11: Tube furnace used for in vacuo deposition of gold nanoparticles, using a tungsten coil wrapped alumina tube, mounted on a 2 $\frac{3}{4}$" power feedthrough.

$$\Delta m = -C \times \Delta f \tag{3.11}$$

where C is a constant depending on the specific crystal used, thus providing a method to measure thin film thickness directly in vacuum. The QCM has applications not only in thin film measurments but has been shown accurate enough to measure gas adsorption down to masses on the order of 1 ng/cm^2 [20].

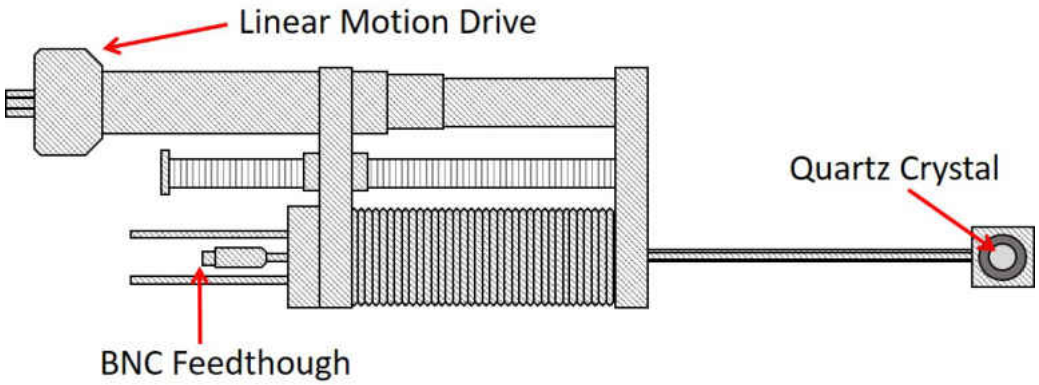

FIGURE 3.12: Quartz crystal microbalance used for monitoring film thickness for preparation of nanoparticle films in vacuum.

The QCM utilized in following experiments is depicted in Figure 3.12, is mounted

on a 2 $\frac{3}{4}$" conflat flange allowing it to be easily exchanged between chambers as necessary. The QCM also features a linear motion drive allowing it to be translated into and out of the chamber, and this feature allows it to be placed in front of the sample and effectively act as a flag until the desired deposition rate is established. A single BNC feedthough is used to connect the instrument to the controller where the deposition rate and thickness can be monitored. In the following experiments the QCM described is used to monitor gold nanoparticle film thickness as deposited in vacuum for electrical measurements.

3.3.4 Nanoparticle Array Fabrication

In order to test the conductivity of molecular linked nanoparticle arrays, devices were fabricated by the means of photo-lithography, a technique used to transfer a geometric pattern onto a substrate [21]. The first step of this process requires spin-coating of the substrate (mica or silica) with a photosensitive resist. For large array devices prepared at UWM a home-built spin coater was prepared using a commercial 120 V fan with an indicated RPM of ∼3000 Figure 3.13, which corresponds to the desired rotational frequency needed from the spin curve of our resist (AZ-1512). Commercially available spin coaters rely on the use of a centered vacuum port to hold the substrate in place, but here an inverted suction cup was used to mimic a vacuum source allowing substrates to be removed without causing damage. Generally samples are spun for ∼60 s at the maximum speed of the fan, and a Variac is used to power the fan in order to allow a slow increase to the maximum speed.

Following spin coating of the resist the substrate has be baked in order to cure the resist. This process is used to remove any solvent initially present in the photoresist, leaving behind a more robust film that is well adhered to the substrate. The baking procedure is typically done by placing the resist-coated substrate on a hot-plate for

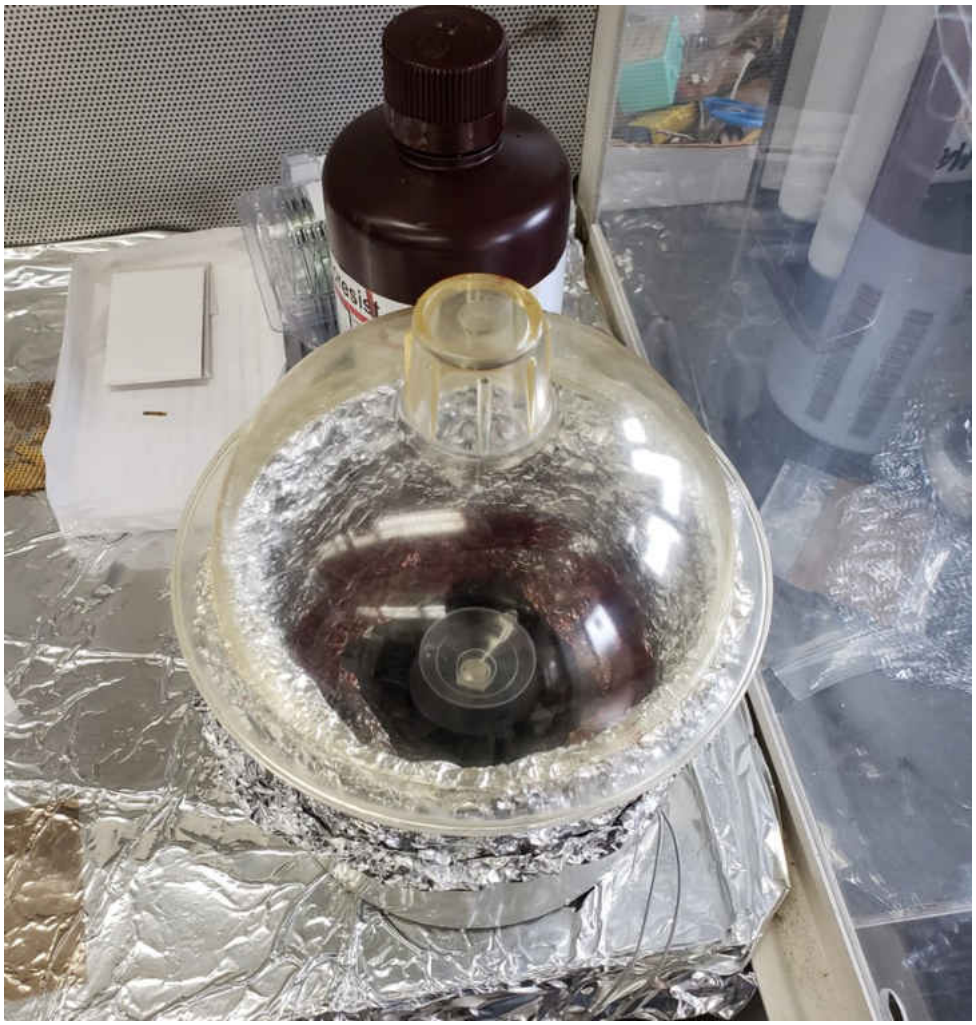

FIGURE 3.13: Home built spin coater used for the fabrication of large-array nanoparticle devices.

a specified time, and for the large array samples this was typically ∼60 s at 100^{o}C. Following the bake, the sample is ready for exposure of the mask pattern by UV radiation. Here we use a chromium mask shown in **??** which results in a exposure of only the transparent areas of the mask. For large array samples a TLC lamp is used as a UV source and requires an exposure time of ∼45 min. Since we are using a positive photoresist the chemical change that occurs in the resist causes the exposed areas to become soluble for the development step.

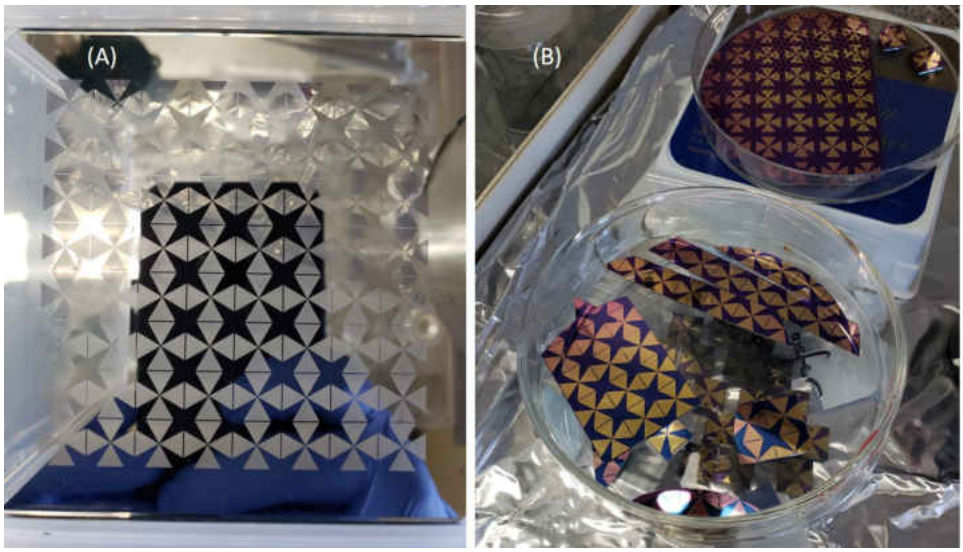

FIGURE 3.14: A) shows the chromium mask used to fabricate large-array samples as well as contact pads for nanogap devices, B) show resulting large array samples on an SiO_2 substrate.

During the development step the exposed substrate is place in a developer solution, and we used 8% tetramethylammonium hydroxide as a common developer. The samples were submerged until the UV exposed portions of the resist were clearly removed ($\sim$30 s), then rinsed thoroughly with deionized water. Following development the substrate is ready for metal evaporation to form the gold electrodes. Due to the weak adhesion of gold films, a thin chromel adhesion layer is first evaporated ($\sim$30 nm), followed by a $\sim$200 nm film of gold. Evaporation of both films takes place in a bell jar evaporator pumped to $\sim 1 \times 10^{-8}$ Torr by means of a liquid nitrogen cooled diffusion pump (Cooke Vacuum Products) shown in Figure 3.15.

Following deposition the substrate is ready for the final stage of lithography referred to as lift-off. The lift-off process utilizes a solvent capable of dissolving the unexposed photo-resist, such as acetone. The substrate now with covered by a gold film is placed in a bath of acetone and sonicated until the resist is completely removed. This leaves behind a thin gold film in the pattern of the original mask to be used as gold electrodes shown in Figure 3.14B. The silica wafer is now ready to be cleaved into

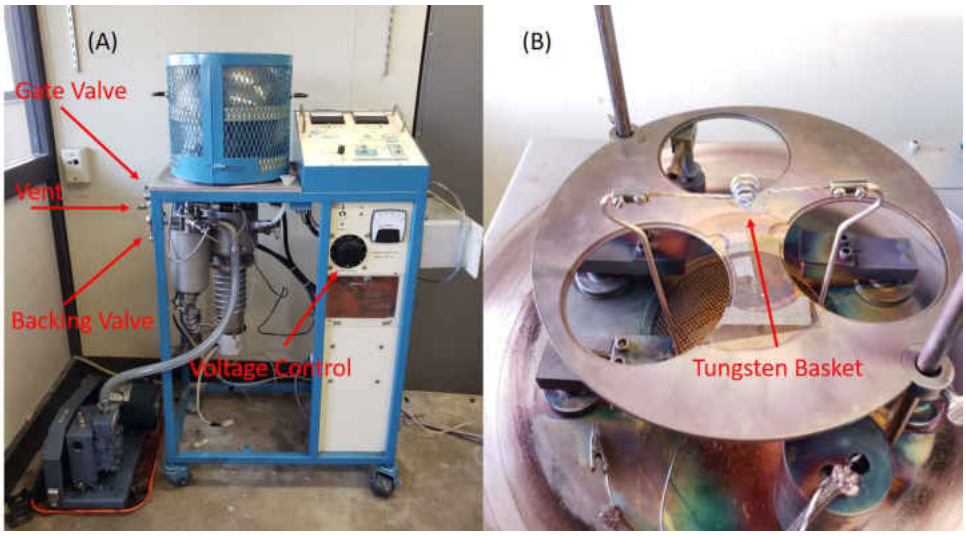

FIGURE 3.15: A) Bell jar evaporator used to deposit gold electrodes for large array devices, B) Tungsten basket used for depositing chromel, and gold films.

single devices consisting of four electrodes. In order to avoid shorting through the oxide film insulated wires are adhered using conductive silver epoxy (H-21D) before finally being placed in the chamber for nanoparticle deposition.

3.3.5 Hybrid Device Fabrication

In order to more precisely investigate the limiting oligomerization of PDI, gold nanoelectrodes were fabricated by means of electron beam lithography. This technique has many similarities with the procedure for photolithography described above. The major difference being the replacement of a physical mask and UV source, with a high energy electron beam that operates using the same principles as SEM. In electron beam lithography the physical mask is replaced by a CAD software designed geometry, that the electron beam system then uses as a guide to control the electron beam, effectively writing the geometry onto the resist coated substrate. The specifics for the fabrication of the gold nanoelectrodes used in this thesis is provided below.

The gold nanoelectrodes were fabricated using a JOEL model JBX-6300FS electron beam lithography system at the Center for Functional Nanomaterials at the Brookhaven National Laboratory. A uniform film of (1:2) ZEP520A:Anisole resist, was spin-coated on a SiO_2 wafer with a 300 nm-thick oxide layer at 2 krpm for 60s and then baked on a hot plate at 180^{o}C for 3 min. Gold electrodes were defined using an electron dose between 300-600 μC/cm^2 using a beam current of 1 nA with a design gap of 0nm. [22] The film was developed in cold hexyl acetate at -20 ^{o}C for 90 sec. Following development, nanogaps were fabricated by e-beam evaporating a chromium adhesion layer which was 3nm thick and deposited at a rate of 0.5 A/s followed by a 30 nm-thick film of gold deposited at a rate of 1.0 A/s, using a Kurt J. Lesker PVD-75 Evaporator. The final lift-off took place by sonication in pure acetone.

Contact pads were fabricated using photolithography that was carried out using a Karl Zeiss MA6 Mask Aligner using S1811 photoresist, which was spin coated at 4krpm for 60s, then baked at 110 ^{o}C for 3 min. A chromium mask was aligned with the previously fabricated nanogaps and exposed to UV radiation for 8.5 s, then developed in MF-312/H_2O 2:3 for 75s. A 3 nm thick chromium adhesion layer was deposited, followed by a 100 nm thick gold film using the conditions given above. The resist was then lifted-off in remover 1165 at 80 ^{0}C. The resulting nanogaps are shown in Figure 3.16.

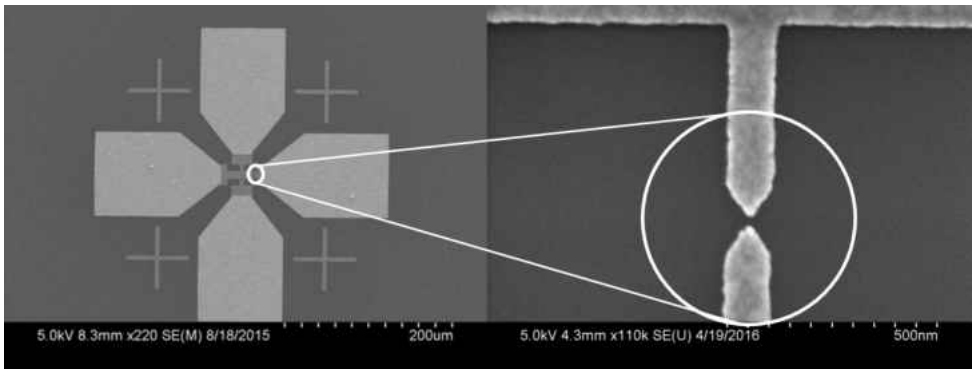

FIGURE 3.16: Resulting nanogap electrodes fabricated by electron beam lithography, typical electrodes have a separation of ∼30 nm.

Bibliography

[1] David C. Joy. *Scanning Electron Microscopy: Theory, History and Development of the Field Emission Scanning Electron Microscope*, chapter 1, pages 1–6. John Wiley Sons, Ltd, 2019.

[2] PA Redhead. Thermal desorption of gases. *vacuum*, 12(4):203–211, 1962.

[3] Kurt W. Kolasinski. *Surface Science: Foundations of Catalysis and Nanoscience*. John Wiley Sons, Ltd, Chichester, UK, 2012.

[4] G Binning and H Rohrer. Scanning tunneling microscopy. In *Scanning Tunneling Microscopy*, pages 40–54. Springer, 1986.

[5] Gerd Binnig, Heinrich Rohrer, Ch Gerber, and Edmund Weibel. Tunneling through a controllable vacuum gap. *Applied Physics Letters*, 40(2):178–180, 1982.

[6] Erik Lægsgaard, Lars Österlund, P Thostrup, PB Rasmussen, I Stensgaard, and F Besenbacher. A high-pressure scanning tunneling microscope. *Review of Scientific Instruments*, 72(9):3537–3542, 2001.

[7] V Rose, JW Freeland, KE Gray, and SK Streiffer. X-ray-excited photoelectron detection using a scanning tunneling microscope. *Applied Physics Letters*, 92(19):193510, 2008.

[8] Nozomi Shirato, Marvin Cummings, Heath Kersell, Yang Li, Benjamin Stripe, Daniel Rosenmann, Saw-Wai Hla, and Volker Rose. Elemental fingerprinting of materials with sensitivity at the atomic limit. *Nano letters*, 14(11):6499–6504, 2014.

[9] Ann-Kathrin Henß, Sung Sakong, Philipp K Messer, Joachim Wiechers, Rolf Schuster, Don C Lamb, Axel Groß, and Joost Wintterlin. Density fluctuations as door-opener for diffusion on crowded surfaces. *Science*, 363(6428):715–718, 2019.

[10] Scheer Elke Cuevas, Juan Carlos. World Scientific, 2010.

[11] AK Kar, S Gangopadhyay, and BK Mathur. A reverse electrochemical floating-layer technique of spm tip preparation. *Measurement Science and Technology*, 11(10):1426, 2000.

[12] Stefan Ernst. Optimisation of the preparation process for tips used in scanning tunneling microscopy. *Physics, Technische Universitat Dresden*, 2006.

[13] Kurt W Kolasinski. *Surface science: foundations of catalysis and nanoscience*. John Wiley & Sons, 2012.

[14] Robert G Greenler. Infrared study of adsorbed molecules on metal surfaces by reflection techniques. *The Journal of Chemical Physics*, 44(1):310–315, 1966.

[15] Friedrich M Hoffmann. Infrared reflection-absorption spectroscopy of adsorbed molecules. *Surface Science Reports*, 3(2-3):107–192, 1983.

[16] David P Landau and Kurt Binder. *A guide to Monte Carlo simulations in statistical physics*. Cambridge university press, 2014.

[17] Luis Gonzalo Lopez, DH Linares, Antonio Jose Ramirez-Pastor, DA Stariolo, and Sergio Alejandro Cannas. Critical behavior of self-assembled rigid rods on two-dimensional lattices: Bethe-peierls approximation and monte carlo simulations. *The Journal of Chemical Physics*, 138(23):234706, 2013.

[18] Kyozi Kawasaki. Diffusion constants near the critical point for time-dependent ising models. i. *Physical Review*, 145(1):224, 1966.

[19] G Sauerbrey. Use of the vibrating quartz for thin film weighing and microweighing. *Z. Phys.*, 155:206, 1959.

[20] V Tsionsky and E Gileadi. Use of the quartz crystal microbalance for the study of adsorption from the gas phase. *Langmuir*, 10(8):2830–2835, 1994.

[21] Philippe Bandelier, Anne-Laure Charley, and Alexandre Lagrange. *Photolithography*, chapter 1, pages 1–40. John Wiley Sons, Ltd, 2013.

[22] MSM Saifullah, T Ondarcuhu, DK Koltsov, C Joachim, and ME Welland. A reliable scheme for fabricating sub-5 nm co-planar junctions for single-molecule electronics. *Nanotechnology*, 13(5):659, 2002.

Chapter 4

Monte Carlo Studies of Nano-Particle Arrays: Modeling Chemical Self-Assembly and Self-Limiting Oligomerization

4.1 Introduction

Following the proposal by Aviram and Ratner that, in principle, electronic devices can be fabricated from individual molecular units [1], there has been a significant effort to understand molecular conductivity. The simplest architecture for building molecular wires comprises pi-conjugated systems wit two terminal anchoring -SH or -NC groups to attach the molecular wire to gold nanoelectrodes; such molecules have been used as linkers for single-molecule conductivity experiments. [2–22] However, in order to design molecular-electronic circuits it is necessary to be able to make controlled electrical connections between nanoelectrodes. This can, in principle, be accomplished by designing a self-assembly strategy in which the growth kinetics of a conducting molecular wire is controlled to selectively connect between gold nodes with different

spacings. [23] A possible strategy to achieve this is to use functionalized nanoparticles to provide molecular linkages between adjacent nanoelectrodes, [24–26] but this approach cannot specifically tune the inter electrode connectivity. An alternative approach is to selectively self-assemble conductive electrical bridges between adjacent nanoelectrodes and this stategy is illustrated in the following using the oligomerization chemistry found for 1,4-phenylene diisocyanobenzene (1,4-PDI) on an Au(111) surface, decribed in greater detail below. In addition, recent work has shown that it is possible to template the distribution of gold nanoparticles on a surface suggesting that organized (gold nanoparticle) nodes can be fabricated as a basis for implementing such circuits. [27]

The experimental approach is based on the discovery that 1,4-PDI self-assembles on an Au(111) substrate to form long one-dimensional, oligomeric chains. The chains are comprised of alternating gold and 1,4-PDI units [28–32] in which a gold adatom is linked to two trans isocyanide groups. In this case, the gold atoms in the oligomer derive from the gold substrate. Density functional theory (DFT) calculations of the oligomerization pathway reveal that growth occurs via a vertical, mobile Au-PDI adatom complex that forms by binding to gold substrate and oligomerizes by the gold adatom attaching to the isocyanide terminus of a growing chain. [33] This process is depicted in Figure 4.1, which illustrates how the interaction of the vertical Au-PDI adatom compex with the terminus of a growing chain forms linear, gold-containing oligomers. It has been shown that 1,4-PDI and analogous molecular can form conductive molecular bridges between adjacent nanoparticles [6, 7, 31, 34, 35] and oligomer-linked gold nanoparticles have been directly imaged using STM. [31]

The original concept for selectively tuning the interconnectivity between gold nanoelectrodes relied on carefully adjusting the dose of the gas-phase oligomer-forming species (in this case, 1,4-PDI) to halt the oligomerization process when the required

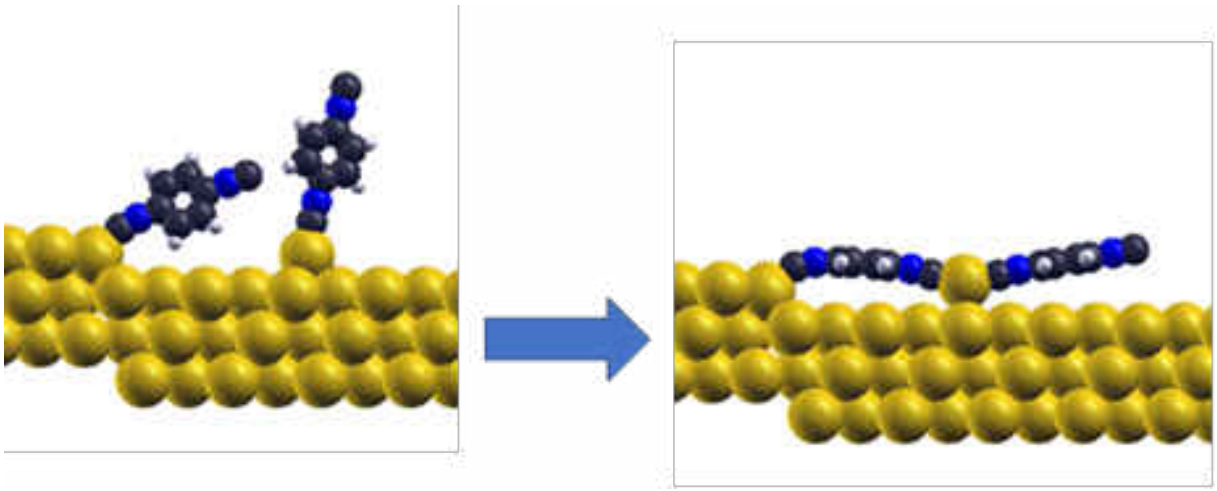

FIGURE 4.1: Schematic depiction of the oligomerization pathway of 1,4-PDI on Au(111) showing the initial approach of a 1,4-PDI/Au adatom complex to the terminus of a 1,4-PDI molecule adsorbed at a step edge or other defect on the Au(111) surface, followed by insertion of the adatom complex into the terminus of the bound 1,4-PDI molecule to initiate self-assembly of Au-1,4-PDI oligomer chains. Adapted with permission from reference [33]. Copyright 2014 American Chemical Society.

bridges had been formed. This necessitates careful control over the dose, internode spacing and the temperature at which the reaction is carried out (to control the various surface reaction rates). In the following, it is shown that the growth of oligomer chains nucleated by gold nanoparticles arrays by reaction with 1,4-PDI is inherently self-limiting, thus eliminating the sensitivity of the interparticle linking process to the reactant dose. This occurs because, on an extended Au(111) substrate, the supply of gold sites required to form the propagating Au-PDI adatom complex is essentially infinite, thereby allowing long oligomer chains to grow essentially uninhibited. In the case of reactions occurring at nodes consisting of gold nanoparticles, both mobile Au-PDI adatom complex formation and the propagation of the oligomer chain are proposed to take place at the peripheral sites on the gold nanoparticle. This suggest that the initiation and growth of oligomer chains block the sites at which the Au-PDI adatom complexes are formed, eventually quenching the reaction to prevent the growth of further oligomers. This process is inherently self-limiting and thus simplifies the strategy

for precisely and selectively linking between carefully spaced nodes that will facilitate the targeted design of nanoelectronic circuits.

The feasibility of this process is investigated in the following by studying the bridging of oligomers formed by dosing 1,4-PDI and the connectivity between gold electrodes as a function of the separation between them. The reaction barriers for the self-assembly process are obtained from the results of previous DFT calculations of the energy barriers for the various elementary step reactions found on a gold substrate. [33] While the reaction barriers found on a pure gold substrate are likely to differ somewhat from those for gold nanoparticles on an insulating substrate, and thus may differ in the kinetic details, these results will provide a test of the feasibility of this approach and will yield predictions of the results of experimental tests of these ideas.

Monte Carlo simulations have been used previously to model the kinetics of relatively complex processes such as catalytic reaction pathways where the kinetics depend on the local enviroment, [36,37] but have also been used to explore self-assembly processes, [38, 39] and provide an ideal approach to studying the kinetics of complex chemical phenomena.

4.2 Results

4.2.1 Analytical Model of Self-Limiting Growth Kinetics

The following simple mean-field kinetic model is developed to illustrate the self-limiting oligomerization kinetics described above. The kinetics will be simulated in greater detail using kinetic Monte Carlo methods in greater detail below. It is assumed that the formation of both the Au-PDI adatom complexes that initiate the reaction (see Figure 4.1) and the growth of the oligomers both occur at the edge sites of the gold nanoparticle nucleus. It is assumed that the proportion of the peripheral sites occupied by the

adatom complexes is given by P_{ad} and the proportion of sites having reacting oligomers is P_{react}, so that, if the proportion of unoccupied peripheral sites is P_v, then;

$$P_v + P_{ad} + P_{react} = 1 \tag{4.1}$$

It is assumed that the 1,4-PDI adsorbs on the surface with Langmuirian kinetics with a rate of adsorption given by $k_{ads}P_vF$, where k_{ads} is an adsorption rate constand and F is the incident flux. The adsorbed adatom complex is also allowed to desorb 1,4-PDI into the gas phase ($k_{des}P_v$), diffuse away from the periphery of the gold nanoparticle to form oligomers (k_1P_{ad}), or tilt to form a terminus to nucleate the growth of an oligomer (k_2P_{ad}) and, assuming steady state, gives;

$$\frac{dP_{ad}}{dt} = k_{ads}P_vF - k_{des}P_v - k_1P_{ad} - k_2P_{ad} = 0 \tag{4.2}$$

where it is assumed that $k_2 >> k_1$ to allow oligomers to form. This provides a relationship between P_{ads} and k_2P_v and substituting from Eqn. 4.1 yields;

$$P_{ad} = \alpha\left(1 - P_{react}\right) \tag{4.3}$$

where $\alpha = \frac{k_{ads}F}{(k_{des}+k_1+k_2)}$. Since the reactive species are proposed to form from the adatom complex at a rate given by k_2P_{ad}, from Eqn. 4.3:

$$P_{react} = 1 - exp\left(-At\right) \tag{4.4}$$

where $A = \frac{k_2\alpha}{1+\alpha}$ and allows an equation for P_{ad} to be derives as:

$$P_{ad} = \frac{A}{k_2}exp\left(-At\right) \tag{4.5}$$

The oligomers form from a reaction between mobile adatom complexes on the surface of the insulating substrate between gold nanoparticle and the reactive site, so that the rate of oligomerization, $\frac{dP_{oligomer}}{dt}$ is written as a second-order process with a rate constant k_3, as:

$$\frac{dP_{oligomer}}{dt} = k_3 P_{react} \theta_{ad} \tag{4.6}$$

where θ_{ad} is the coverage of the reacting adatom complex on the surface and is, for simplicity assumed to be in equilibrium with the adatom complex formed on the periphery of the gold nanoparticle; $\frac{\theta_{ad}}{P_{ad}} = K$. This yields a time dependence of the average oligomer length given by:

$$P_{oligomer} = \frac{k_3 K}{2k_2} \left(1 - 2exp\left(-At\right) + exp\left(-2At\right)\right) \tag{4.7}$$

Since the term in brackets tends asymptotically to unity, the limiting oligomer length is given by $\frac{k_3 K}{2k_2}$, while the rate at which they form depends on the parameter A.

The variation in the proportion of the gold nanoparticle sites occupied by reactive sites (P_{react}) and adatom complexes (P_{ad}) are plotted as a function of time for $\alpha = 5$,k_2 and $k_1 = 0.002$ and $K = 10$ in Figure 4.2. At the beginning of the reaction, only adatom compexes (•) and a small proportion of vacant sites are present. As the reaction proceeds, the proportion of adatom complexes decreases exponentially (4.5), while the proportion of active sites (■) increases, eventually occupying all sites on the periphery of the gold nanoparticle, thereby quenching the reaction. This is illustrated in Figure 4.3 using the same kinetic parameters as for Figure 4.2, where the oligomers initially grow slowly as the reactive sites are initiated, but then slow and eventually sease when there are no more available sites for the adatom complexes to form (Figure 4.2), in this

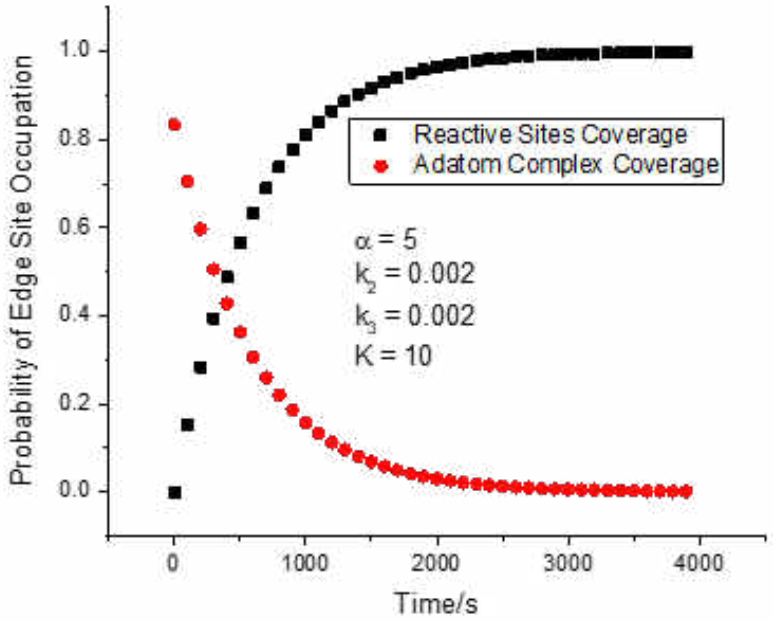

FIGURE 4.2: Plot of variation in the proportion of the gold nanoparticle sites occupied by reactive sites (P_{react}) and adatom complexes (P_{ad}) plotted as a function of time for $\alpha = 5$, k_2 and $k_1 = 0.002$ and $K = 10$.

case at an average oligomer length of 6 units. While this is a simplified model, it illustrated the salient points of the self-limiting assembly of conducting Au-PDI oligomer chains.

4.2.2 Monte Carlo Simulations of Self-Limiting Growth Kinetics

The effect of particle separation on the ability of oligomers to form conducting bridges between gold nanoparticles is studied using the model system schematically illustrated in Figure 4.4. This shows a series of hexagonal gold nanoparticles (in yellow) on an insulating substrate for various increasing particle separations, with Panel (a) showing the smallest separation and Panel (d) showing the larges separation used for

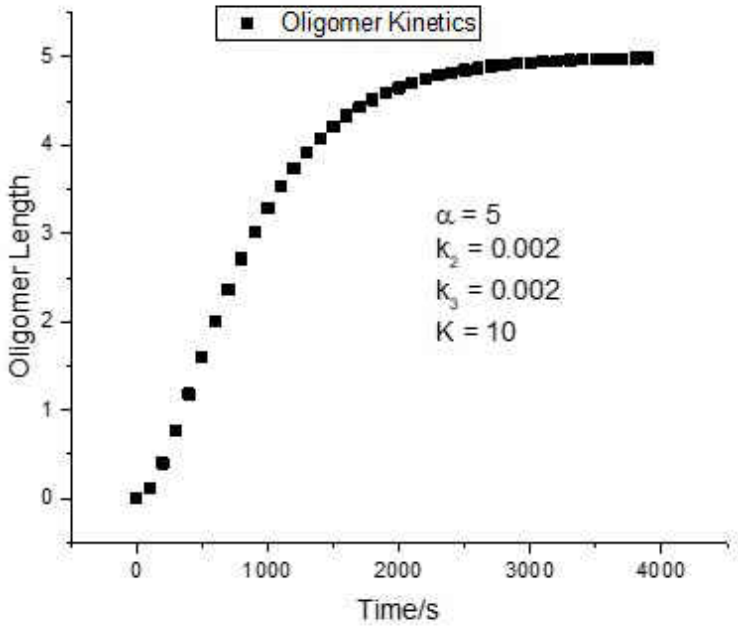

FIGURE 4.3: Plot of average oligomer length plotted as a function of time for $\alpha = 5$, k_2 and $k_1 = 0.002$ and $K = 10$.

the simulations. Each of the simulations are carried out using a constant 1,4-PDI arrival rate (proportional to the flux). The 1,4-PDI is allowed to adsorb only on the edge sites of the gold nanoparticle. Note that the 1,4-PDI could also adsorb on top of the gold nanoparticle. [40] Note that 1,4-PDI can then diffuse to adsorb to an edge site, this 1,4-PDI could contribute to the growth of an oligomer chain and would result in an effectively higher edge-site arrival rate and an acceleration of the overall growth kinetics. The 1,4-PDI could, in principle, also adsorb on the insulating substrate but, because this cannot form an Au-PDI adatom complex, it does not contribute to the overall growth kinetics. As noted above, the simulation parameters were derived from the energy barriers obtained from DFT calculations. [33] The final structures after the completion of self-limited growth are also indicated in 4.4, showing the resulting oligomeric assemblies in red and remaining peripheral adatom complexes in orange. Figure 4.4(d)

shows the final structures with a node separation that prohibits oligomer bridges from forming between nano-particles and reveals the formation of oligomers at almost all peripheral sites on the nanoparticle. Closer examination shows a few edge sites that contain an adatom complex, but they are surrounded by loops of oligomers detected prevoiusly by STM [31] and are therefore trapped and not able to diffuse away from the gold nanoparticles.

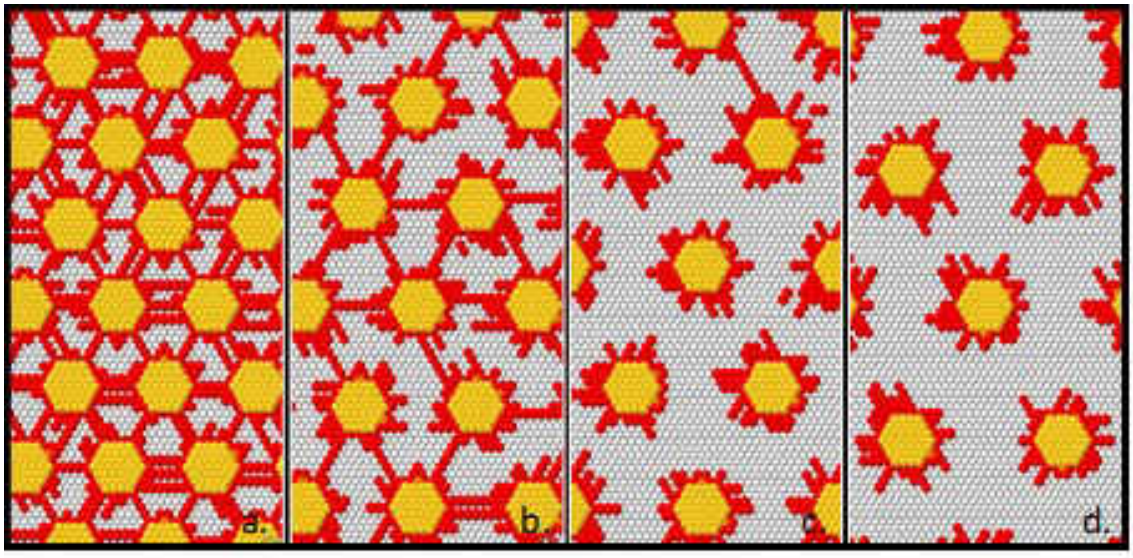

FIGURE 4.4: Depiction of typical model nanoparticles systems used for the simulations. The diameters of the hexagonal gold nanoparticles (depicted in yellow) are maintained at a constant value of seven units across. The growing Au–PDI oligomer units are depicted in red on the same scale as the atoms in the gold nanoparticles. The nearest-neighbor separations are varied from (a) 5, (b) 8, (c) 11 and (d) 13 units.

Smaller interparticle spacings (Figure 4.4b) lead to the formation of oligomeric bridges between nanoparticle nodes that form when two oligomers from adjacent nanoparticles join to provide a longer oligomer. In almost all cases for this nanoparticle spacing, the nanoparticles are linked by a single oligomer, suggesting that it may be possible to judiciously select interparticle spacings to form single conductive linkages. As the interparticle spacing decreases (Figure 4.4a), multiple bridges can form.

The kinetics are summarized graphically in Figure 4.5 as a function of intermolecular separation plotted as ln(MCS) to emphasize the behavior at short times. In all cases, the edge sites are populated by only Au-PDI adatom complexes for the first ~10 MCS, after which the adatom complexes can diffuse and react with another reactive adatom complex to initially form dimers (chain lenght = 2). At longer times, more oligomers are nucleated and increase in number as a function of time to reach constant values as the assembly process self-limits. The exception is the formation of dimers where the proportion of dimers rapidly increases, but then decreases once again indicating that the rate of growth of dimers by reaction of adatom complex exceeds the rate at which they are formed.

The final chain-length distribution is shown in Figure 4.6, which distinguishes between those oligomers that can form conductive bridges, and those that do not. As expected, for systems in which the nanoparticles are too far apart to form bridges (Figure **??**d,e), the chain length distributions are identical. The chain-length distribution differs from a Schultz-Flory distribution [41] because of a limited inventory of propagating monomers. As the nanoparticles become closer to each other (Figure 4.6c), the distribution of nonbridging oligomers is sightly perturbed resulting in the formation of oligomers longer than 8 units because of bridging between the gold nanoparticles, where the oligomer distribution is dictated by the distances between sites on the edges of the nanoparticles. The distribution becomes even more perturbed from that found for the nonbridging systems with smaller internodal spacings.

Finally, Figure 4.7 plots the total number of percolation pathways for a system with a nanoparticle spacing of 5 monomers, where conductive bridges are formed. Here percolation paths are defined as the ability to connect a site on one edge of a sample to a site on the opposite edge following a NN pathway, where only oligomer species

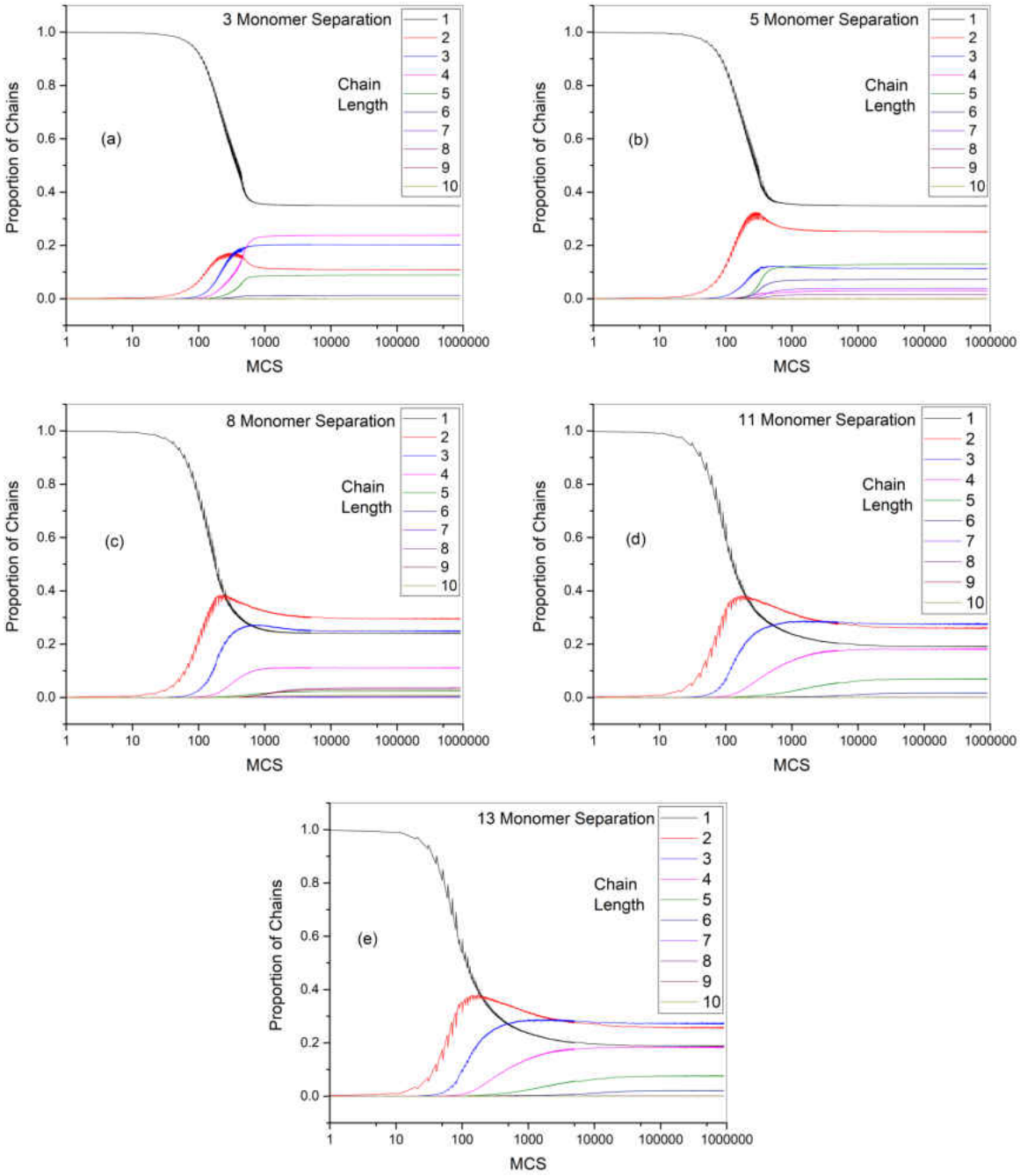

FIGURE 4.5: Plots of the population of Au-PDI oligomer units with different chain lengths as a function of the number of MCSs, which varies linearly with real time, using a constant incident flux of 1,4-PDI. A chain length of unity refers to the population of Au-PDI adatom complexes. The time variation of the distribution is shown for NN separarations of (a) 3, (b) 5, (c) 8, (d) 11, and (e) 13 monomer units.

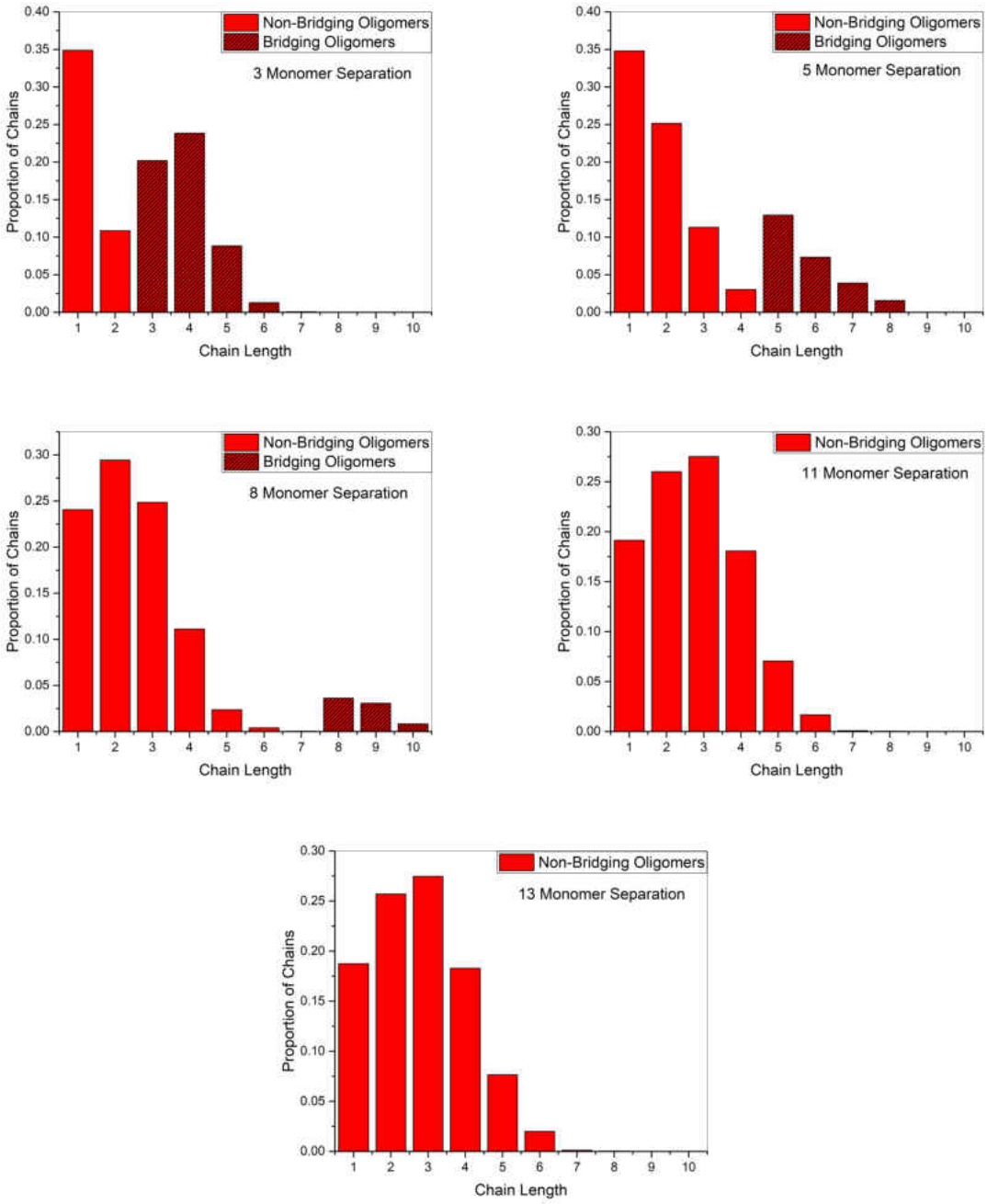

FIGURE 4.6: Histograms of the final, self-limiting chain-length distributions for the NN separations (a) 3, (b) 5, (c) 8, (d) 11, and (e) 13 monomer units. The histograms highlighted in red show the length distribution for nonbridging oligomers, while the crossed-hatched histograms give the distributions for the bridging oligomers.

and nodes can contribute to percolation. Not that for greater than ∼11 monomer spacings, no conductive bridges are predicted to occur and so that no significant increase in conductivity is expected to occur for gold nanoparticles placed farther apart than this. The resulting total number of percolation paths is plotted as a function of MCS showing a similar general form for the simple model in Figure 4.3, where there is an initial slow increase in percolation pathways for short times as oligomerization is initiated, and some bridges start to form. The number of percolation pathways then increase quite rapidly as more bridges form to eventually saturate to lead to a maximum value in conductivity. Note that the change in total number of percolation pathways can be related to the change in conduction [42, 43] to enable the results to be compared with the experiment.

The above analytical and Monte Carlo theroy analyses predict that the bridgin of gold nanoparticles by conductive Au-PDI oligomer chains should be self-limiting because both the initiation of the growth of oligomers by the formation of mobile adatom complexes and the propagation of the oligomers themselves occur at the peripheral edge sites of the gold nanoparticles. This suggests that judiciously spaced gold-nanoparticle nodes will enable them to be selectively bridged either by single(Figure 4.4b) or multiple (Figure 4.4a) conductive oligomer chains. This approach can, in principle, be used to design molecular-electronic architectures that might eventually form the basis for designing functional electronic circuits based on the assembly of molecular units. It is argued that, because the Monte Carlo simulations were carried out for reactions occuring at room temperature (∼298 K), using energies for the oligomerization of 1,4-PDI on gold from DFT calculations, the theoretical predictions should be reasonably accurate. In particular, if the monomer separation is taken to be equal to the periodicity of the oligomer chains formed from 1,4-PDI on Au(111) surfaces [29,31] of ∼1.1 nm, bridging between nanoelectrodes should only occur for spacing less than

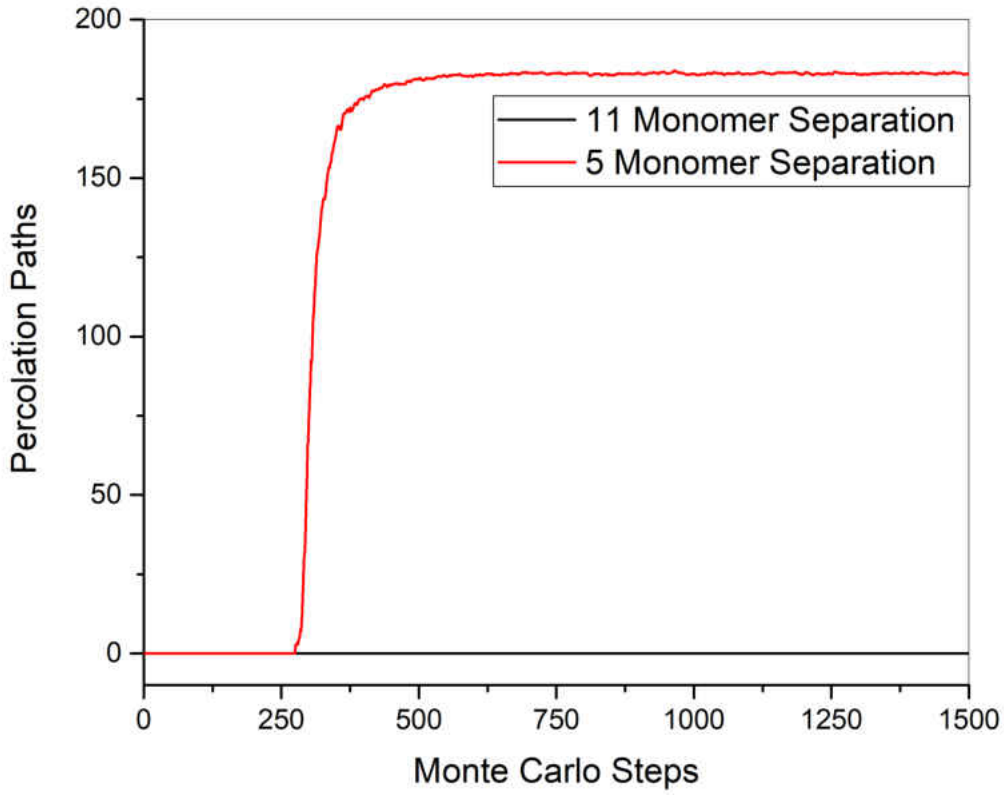

FIGURE 4.7: Plot of total number of percolation pathways as a function of MCSs at a constant flux of 1,4-PDI.

$\sim$12nm. For smaller spacing, the variation in conductivity as a function of total 1,4-PDI dose (pressure $\times$ time) should initially increase slowly, but accelerate with further dosing to reach a constant value of conductivity. The simple analytical model outlined in Section 4.2.1 suggests that the growth kinetics depend on the incident flux, but that the final chain length (and thus conductivity) is independent of the flux.

4.3 Conclusion

The work reported here suggests that the spontaneous oligomerization of 1,4-PDI, which is found on the Au(111) surface to form long, conducting oligomer chains, instead forms self-limiting oligomers on gold nanoparticles on an insulating substrate. It has been shown experimentally that the conductivities of gold-nanoparticle arrays increase when dosed with a range of diisocyanides, but the influence of nanoparticle separation has not yet been investigated for these systems in a controlled way. It has also been found that analogous dithiols similarly form gold-containing oligomeric species [44] suggesting that similar targeted nanoparticle bridging should be possible for other bifunctional molecules. It is noted that the simulations were carried out for energies for 1,4-PDI with the temperature set to $\sim$298 K to correspond to the most convenient experimental temperature. However, changing the reaction temperature will also change the relative rates of the various self-assembly processes thereby offering the possibility of tuning the range of distances over which the molecules can bridge merely by changing the reaction temperature.

Bibliography

[1] Arieh Aviram and Mark A Ratner. Molecular rectifiers. *Chemical physics letters*, 29(2):277–283, 1974.

[2] Mikio Ito, Hidenori Noguchi, Katsuyoshi Ikeda, and Kohei Uosaki. Substrate dependent structure of adsorbed aryl isocyanides studied by sum frequency generation (sfg) spectroscopy. *Physical Chemistry Chemical Physics*, 12(13):3156–3163, 2010.

[3] BongSoo Kim, Jeremy M Beebe, Yongseok Jun, X-Y Zhu, and C Daniel Frisbie. Correlation between homo alignment and contact resistance in molecular junctions: aromatic thiols versus aromatic isocyanides. *Journal of the American Chemical Society*, 128(15):4970–4971, 2006.

[4] Yan Li, Deyu Lu, Sally A Swanson, J Campbell Scott, and Giulia Galli. Microscopic characterization of the interface between aromatic isocyanides and au (111): A first-principles investigation. *The Journal of Physical Chemistry C*, 112(16):6413–6421, 2008.

[5] Kristen L Murphy, Wilfred T Tysoe, and Dennis W Bennett. A comparative investigation of aryl isocyanides chemisorbed to palladium and gold: An atr-ir spectroscopic study. *Langmuir*, 20(5):1732–1738, 2004.

[6] Mitchell J Robertson and Robert J Angelici. Adsorption of aryl and alkyl isocyanides on powdered gold. *Langmuir*, 10(5):1488–1492, 1994.

[7] Kuo-Chen Shih and Robert J Angelici. Equilibrium and saturation coverage studies of alkyl and aryl isocyanides on powdered gold. *Langmuir*, 11(7):2539–2546, 1995.

[8] Jason I Henderson, Sue Feng, Gregory M Ferrence, Thomas Bein, and Clifford P Kubiak. Self-assembled monolayers of dithiols, diisocyanides, and isocyanothiols on gold:'chemically sticky'surfaces for covalent attachment of metal clusters and studies of interfacial electron transfer. *Inorganica chimica acta*, 242(1-2):115–124, 1996.

[9] Mark A Reed, C Zhou, CJ Muller, TP Burgin, and JM Tour. Conductance of a molecular junction. *Science*, 278(5336):252–254, 1997.

[10] SN Yaliraki, M Kemp, and Mark A Ratner. Conductance of molecular wires: Influence of molecule- electrode binding. *Journal of the American Chemical Society*, 121(14):3428–3434, 1999.

[11] XD Cui, A Primak, X Zarate, J Tomfohr, OF Sankey, Ana L Moore, Thomas A Moore, D Gust, Gari Harris, and SM Lindsay. Reproducible measurement of single-molecule conductivity. *science*, 294(5542):571–574, 2001.

[12] Yongqiang Xue and Mark A Ratner. Microscopic study of electrical transport through individual molecules with metallic contacts. i. band lineup, voltage drop, and high-field transport. *Physical Review B*, 68(11):115406, 2003.

[13] Xiaoyin Xiao, Bingqian Xu, and Nongjian J Tao. Measurement of single molecule conductance: Benzenedithiol and benzenedimethanethiol. *Nano Letters*, 4(2):267–271, 2004.

[14] Manabu Kiguchi, Shinichi Miura, Kenji Hara, Masaya Sawamura, and Kei Murakoshi. Conductance of a single molecule anchored by an isocyanide substituent to gold electrodes. *Applied physics letters*, 89(21):213104, 2006.

[15] Renato B Pontes, Frederico D Novaes, Adalberto Fazzio, and Antonio JR da Silva. Adsorption of benzene-1, 4-dithiol on the au (111) surface and its possible role in molecular conductance. *Journal of the American Chemical Society*, 128(28):8996–8997, 2006.

[16] Makusu Tsutsui, Yumi Teramae, Shu Kurokawa, and Akira Sakai. High-conductance states of single benzenedithiol molecules. *Applied physics letters*, 89(16):163111, 2006.

[17] A Arnold, F Weigend, and F Evers. Quantum chemistry calculations for molecules coupled to reservoirs: formalism, implementation, and application to benzenedithiol. *The Journal of chemical physics*, 126(17):174101, 2007.

[18] Sina Yeganeh, Mark A Ratner, Michael Galperin, and Abraham Nitzan. Transport in state space: Voltage-dependent conductance calculations of benzene-1, 4-dithiol. *Nano letters*, 9(5):1770–1774, 2009.

[19] K Horiguchi, M Tsutsui, S Kurokawa, and A Sakai. Electron transmission characteristics of au/1, 4-benzenedithiol/au junctions. *Nanotechnology*, 20(2):025204, 2008.

[20] Artem Mishchenko, David Vonlanthen, Velimir Meded, Marius Burkle, Chen Li, Ilya V Pobelov, Alexei Bagrets, Janne K Viljas, Fabian Pauly, Ferdinand Evers, et al. Influence of conformation on conductance of biphenyl-dithiol single-molecule contacts. *Nano letters*, 10(1):156–163, 2009.

[21] Youngsang Kim, Torsten Pietsch, Artur Erbe, Wolfgang Belzig, and Elke Scheer. Benzenedithiol: a broad-range single-channel molecular conductor. *Nano letters*, 11(9):3734–3738, 2011.

[22] Renato Borges Pontes, Alexandre Reily Rocha, Stefano Sanvito, Adalberto Fazzio, and Antonio Jose Roque da Silva. Ab initio calculations of structural evolution and conductance of benzene-1, 4-dithiol on gold leads. *ACS nano*, 5(2):795–804, 2011.

[23] Alejandro Miguel Boscoboinik, Sergio Javier Manzi, WT Tysoe, Victor Daniel Pereyra, and JA Boscoboinik. Directed nanoscale self-assembly of molecular wires interconnecting nodal points using monte carlo simulations. *Chemistry of Materials*, 27(19):6642–6649, 2015.

[24] K-H Muller, J Herrmann, B Raguse, G Baxter, and T Reda. Percolation model for electron conduction in films of metal nanoparticles linked by organic molecules. *Physical Review B*, 66(7):075417, 2002.

[25] N Fishelson, I Shkrob, O Lev, J Gun, and AD Modestov. Studies on charge transport in self-assembled gold- dithiol films: conductivity, photoconductivity, and photoelectrochemical measurements. *Langmuir*, 17(2):403–412, 2001.

[26] Roger H Terrill, Timothy A Postlethwaite, Chun-hsien Chen, Chi-Duen Poon, Andreas Terzis, Aidi Chen, James E Hutchison, Michael R Clark, and George Wignall. Monolayers in three dimensions: Nmr, saxs, thermal, and electron hopping studies of alkanethiol stabilized gold clusters. *Journal of the American Chemical Society*, 117(50):12537–12548, 1995.

[27] Beatriz Roldan Cuenya. Metal nanoparticle catalysts beginning to shape-up. *Accounts of chemical research*, 46(8):1682–1691, 2012.

[28] Jorge Boscoboinik, John Kestell, Michael Garvey, Michael Weinert, and Wilfred T Tysoe. Creation of low-coordination gold sites on au (111) surface by 1, 4-phenylene diisocyanide adsorption. *Topics in Catalysis*, 54(1-4):20–25, 2011.

[29] Jorge A Boscoboinik, Florencia C Calaza, Zeesham Habeeb, Dennis W Bennett, Dario J Stacchiola, Martin A Purino, and Wilfred T Tysoe. One-dimensional supramolecular surface structures: 1, 4-diisocyanobenzene on au (111) surfaces. *Physical Chemistry Chemical Physics*, 12(37):11624–11629, 2010.

[30] J Zhou, D Acharya, N Camillone III, P Sutter, and MG White. Adsorption structures and electronic properties of 1, 4-phenylene diisocyanide on the au (111) surface. *The Journal of Physical Chemistry C*, 115(43):21151–21160, 2011.

[31] John Kestell, Rasha Abuflaha, J Anibal Boscoboinik, Yun Bai, Dennis W Bennett, and Wilfred T Tysoe. Linking gold nanoparticles with conductive 1, 4-phenylene diisocyanide–gold oligomers. *Chemical Communications*, 49(14):1422–1424, 2013.

[32] John Kestell, Rasha Abuflaha, J Anibal Boscoboinik, Michael Garvey, Dennis W Bennett, and Wilfred T Tysoe. Determination of adsorbate structures from 1, 4-phenylene diisocyanide on gold. *The journal of physical chemistry letters*, 5(20):3577–3581, 2014.

[33] Michael Garvey, John Kestell, Rasha Abuflaha, Dennis W Bennett, Graeme Henkelman, and Wilfred T Tysoe. Understanding and controlling the 1, 4-phenylene diisocyanide–gold oligomer formation pathways. *The Journal of Physical Chemistry C*, 118(36):20899–20907, 2014.

[34] Rasha Abuflaha, Dustin Olson, Dennis W Bennett, and Wilfred T Tysoe. Surface chemistry and structures of 1, 4-phenylene diisocyanide on gold films from solution. *Surface Science*, 649:56–59, 2016.

[35] Rasha Abuflaha and Wilfred T Tysoe. Spontaneous self-assembly of conductive molecular linkages between gold nanoelectrodes from aryl diisocyanides. *Applied Physics A*, 124(11):784, 2018.

[36] Eric W Hansen and Matthew Neurock. First-principles-based monte carlo simulation of ethylene hydrogenation kinetics on pd. *Journal of Catalysis*, 196(2):241–252, 2000.

[37] Donghai Mei, Eric W Hansen, and Matthew Neurock. Ethylene hydrogenation over bimetallic pd/au (111) surfaces: application of quantum chemical results and dynamic monte carlo simulation. *The Journal of Physical Chemistry B*, 107(3):798–810, 2003.

[38] Fabien Silly, Ulrich K Weber, Adam Q Shaw, Victor M Burlakov, Martin R Castell, GAD Briggs, and David G Pettifor. Deriving molecular bonding from a macromolecular self-assembly using kinetic monte carlo simulations. *Physical Review B*, 77(20):201408, 2008.

[39] Carlos-Andres Palma, Marco Cecchini, and Paolo Samori. Predicting self-assembly: from empirism to determinism. *Chemical Society Reviews*, 41(10):3713–3730, 2012.

[40] Ahmed Ghalgaoui, Nassar Doudin, Emil Kelderer, and Martin Sterrer. 1, 4-phenylene diisocyanide (pdi) interaction with low-coordinated gold sites: Dissociation and adsorbate-induced restructuring. *The Journal of Physical Chemistry C*, 2018.

[41] Paul J Flory. Molecular size distribution in linear condensation polymers1. *Journal of the American Chemical Society*, 58(10):1877–1885, 1936.

[42] David S McLachlan, Michael Blaszkiewicz, and Robert E Newnham. Electrical resistivity of composites. *Journal of the American Ceramic Society*, 73(8):2187–2203, 1990.

[43] Junjie Wu and DS McLachlan. Percolation exponents and thresholds obtained from the nearly ideal continuum percolation system graphite-boron nitride. *Physical Review B*, 56(3):1236, 1997.

[44] John Kestell, Rasha Abuflaha, Michael Garvey, and Wilfred T Tysoe. Self-assembled oligomeric structures from 1, 4-benzenedithiol on au (111) and the formation of conductive linkers between gold nanoparticles. *The Journal of Physical Chemistry C*, 119(40):23042–23051, 2015.

Chapter 5

Chemical Self-Assembly Strategies for Designing Molecular Electronic Circuits

5.1 Introduction

It is a significant experimental challenge to devise self-assembly strategies for the targeted design of electronic circuits based on molecules. [1–3] We recently proposed a self-limiting self-assembly method for selectively making controlled electrical connections between gold nano-electrode nodes [4] based on the oligomerization of 1,4-phenylene diisocyanide(1,4-PDI). 1,4-PDI self-assembles on gold to form conductive, one-dimensional, oligomeric chains that are comprised of alternating gold and 1,4-PDI units [5–9] in which a gold adatom is linked to two trans isocyanide groups. It was proposed in Chapter 4 that oligomer growth that is nucleated by gold nanoparticles is inherently self-limiting, thereby eliminating the sensitivity of the interparticle linking process to the reactant dose. [10] The self-limiting kinetics were modeled using an oligomer formation mechanism derived from density functional theory (DFT) calculations, which showed that oligomerization is initiated by the formation of a vertical, mobile Au-1,4-PDI adatom complex that forms by binding to the gold substrate, which

then oligomerizes by the gold adatom attaching to the isocyanide terminus of a growing chain. [11] The DFT calculations also determined the activation barriers for the various elementary-step processes and showed that the diffusion barrier for the motion of the Au-1,4-PDI adatom complex was low, while the activation energy for the oligomerization was found to be 152 kJ/mol. A kinetic Monte Carlo analysis demonstrated that the extent of oligomerization was limited because both the formation of the mobile Au-1,4-PDI adatom complex and the propagation of the oligomer chain take place at the peripheral sites on the gold nanoparticle. As a result, the initiation and growth of oligomer chains eventually block the sites at which the Au-1,4-PDI adatom complexes are formed, thereby quenching the reaction to prevent the growth of further oligomers and is therefore inherently self-limiting. [4] Using kinetic parameters found for the formation of oligomers on Au(111), the model predicted that the oligomers should be able to bridge gold nanoparticle nodes that were less than $\sim$ 12 nm apart. It has previously been demonstrated that 1,4-PDI and analogous molecules comprising two terminal anchoring -SH groups can form conductive molecular bridges between adjacent nanoparticles deposited onto an insulating mica substrate. [8, 12–15] Oligomer-linked gold nanoparticles have been directly imaged using STM [8] and have been used in single-molecule conductivity experiments. [13, 14, 16–34] While these experiments on an insulating mica substrate did not measure the conductivity as a function of particle separation, they do demonstrate the ability of these bifunctional molecules to link between nanoparticles on surfaces.

The following tests the prediction that the formation of conductive linkages between gold nanoparticles on and insulating support is self-limiting by measuring the conductivity of a relatively large array ($\sim$ 0.25 mm between the gold electrodes) of

gold nanoparticles deposited by evaporating gold onto a silica substrate in high vacuum as a function of gold film thickness. While his approach did not lead to nanoparticle spacings as large as the limiting value of $\sim$ 12 nm predicted by kinetic Monte Carlo simulations, it reveals a decrease in the change in conductivity after dosing with 1,4-PDI as the average gold nanoparticle spacing increased.

The ability to bridge nanogaps was therefore explored in greater detail using devices consisting of lithographically fabricated nanoelectrodes with gap spacings of $\sim 30nm$, significantly larger than the limiting spacing measured from kinetic Monte Carlo simulations. They showed no conductivity after dosing with 1,4-PDI. Hybrid devices were also fabricated by depositing a thin film of gold on the nanoelectrode devices by evaporation in vacuo to form nanoparticles in the interelectrode region to reduce the gap. [35] These hybrid devices displayed significant electron conductivity thereby experimentally verifying the postulate discussed above. [4]

5.2 Experimental Methods

5.2.1 Fabrication of Gold Nanogaps

The gold nanoelectrodes were fabricated using a JOEL model JBX-6300FS electron beam lithography system at the Center for Functional Nanomaterials at the Brookhaven National Laboratory. A uniform film of (1:2) ZEP520A:Anisole resist, was spin-coated on a SiO_2 wafer with a 300 nm-thick oxide layer at 2 krpm for 60s and then baked on a hot plate at 180^{o}C for 3 min. Gold electrodes were defined using an electron dose between 300-600 μC/cm^2 using a beam current of 1 nA with a design gap of 0nm. [36] The film was developed in cold hexyl acetate at -20 ^{o}C for 90 sec. Following development, nanogaps were fabricated by e-beam evaporating a chromium adhesion layer which was 3nm thick and deposited at a rate of 0.5/s followed by a 30 nm-thick film of

gold deposited at a rate of 1.0 /s, using a Kurt J. Lesker PVD-75 Evaporator. The final lift-off took place by sonication in pure acetone.

Contact pads were fabricated using photolithography that was carried out using a Karl Zeiss MA6 Mask Aligner using S1811 photoresist, which was spin coated at 4krpm for 60s, then baked at 110^{o}C for 3 min. A chromium mask was aligned with the previously fabricated nanogaps and exposed to UV radiation for 8.5 s, then developed in MF-312/H_2O 2:3 for 75s. A 3 nm thick chromium adhesion layer was deposited, followed by a 100 nm thick gold film using the conditions given above. The resist was then lifted-off in remover 1165 at 80 ^{0}C.

5.2.2 Fabrication of Gold Nanoparticle Array

The electrical characteristics were measured for larger-scale nanoparticle arrays to precisely monitor the change in current with 1,4-PDI dose. They were fabricated using gold electrodes deposited onto an oxidized silica substrate to create a gap of 0.25 mm between the gold electrodes. The electrode gap was defined using a chromium mask. The pattern was developed by photolithography using AZ 1512 resist spun onto a silica substrate using a spin-coater at $\sim$3 krpm for 60 s. The resist was exposed using an ultra violet lamp (TLC) for 30 min and then developed in 8% TMAH (tetramethylammonium hydroxide). A chromel adhesion layer ($\sim$5 nm thick) was deposited on the silica prior to evaporating a $\sim$200 nm thick film of gold in a vacuum evaporator. The film thicknesses were estimated from the total amount of material flash-evaporated and the distance from the source to the silica sample.

The sample was then attached to a sample manipulator in a high vacuum chamber operating at a base pressure of $\sim 1 \times 10^{-8}$ Torr. Gold was deposited from a home-built alumina tube furnace at a rate of $\sim$ 0.02 A/s and was monitored by a QCM (Sigma Instruments SQM-160) until the final desired film thickness was obtained.

5.2.3 Measurment of I/V Curves

The I/V characteristics were measured by applying a voltage between the gold electrodes via a D/A converter and the resulting current measured by means of a picoammeter that was monitored by a A/D converter to yeild I/V curves directly. No changes were found in the I/V curves for repeated experiments indicating that the sample remained stable. The temperature dependence of the conductivity was measured by allowing a cooled sample to warm slowly to ambient temperature. 1,4-PDI was dosed onto the sample via a home built Knudsen source [37] where the flux was gauged by the increase in background pressure in the vacuum chamber and was varied by changing the temperature of the 1,4-PDI sample.

5.2.4 Estimation of Nanoparticle Separation

Scanning Electron Microscope (SEM) images of gold nanoparticles deposited in vacuo on silica are displayed in Figure 5.4 for various total film thicknesses, t, which are measured using a quartz crystal microbalance and are used as a basis for estimating the average particle separation as a function of film thickness. The SEM images were analyzed using ImageJ [38], where the contrast is first enchanced to more easily identify the particles. The images were analyzed to count the number of particles per unit area and the results are shown plotted in Figure 5.1 (■) as a function of the thickness of the film, and fitted to a allometric function:

$$N(t) = N_0 t^n \tag{5.1}$$

where $N_0 = 4.6 \pm 0.2 \times 10^{-2}$ particles/nm^2 and $n = -1.55 \pm 0.10$.

The SEM images were analyzed to measure the proportion of the surface covered by gold as a function of the film thickness and the results are displayed in Figure 5.2

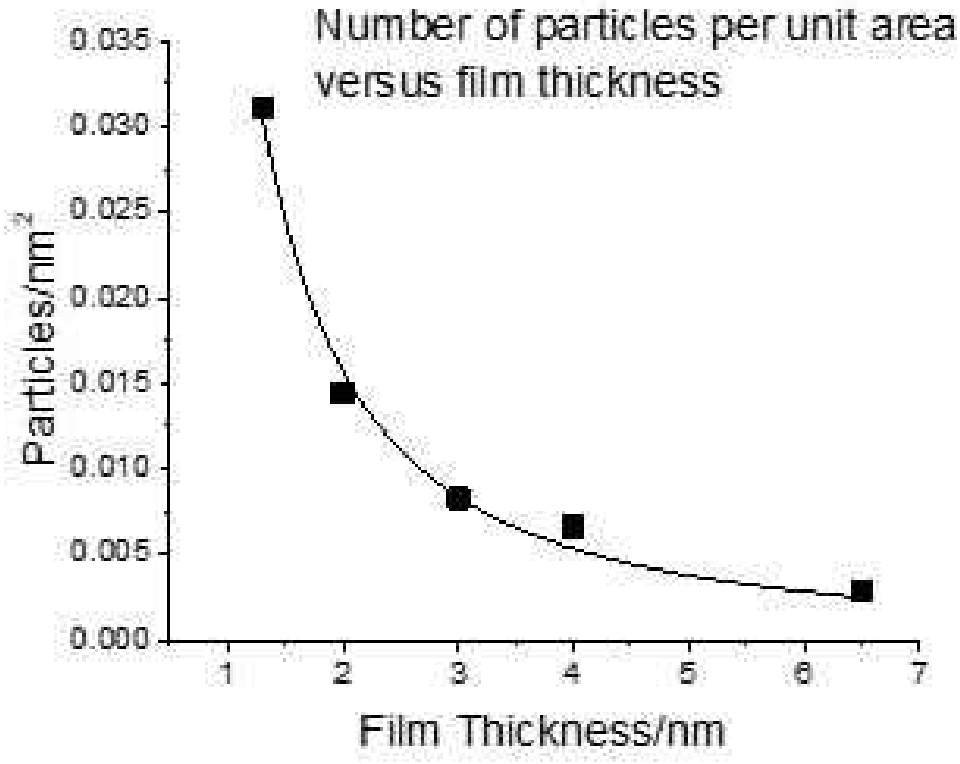

FIGURE 5.1: Plot of the number of nanoparticles per unit area as a function of film thickness on silica.

(■) and fits are also shown to an allometric growth equation:

$$\alpha(t) = \alpha_0 t^m \tag{5.2}$$

where $\alpha_0 = 0.29 \pm 0.01$ and $m = 0.36 \pm 0.03$.

It is not possible to use image analysis software to measure the closest interparticle distances as a function of film thickness. However, an estimate of the variation in interparticle distance can be made from the measurements of $N(t)$ and $\alpha(t)$ as follows. It is assumed that circular particles with average diameter $d(t)$ are uniformly distributed on the surface with an average separation $s(t)$ so that the number of nanoparticles per unit area is given by:

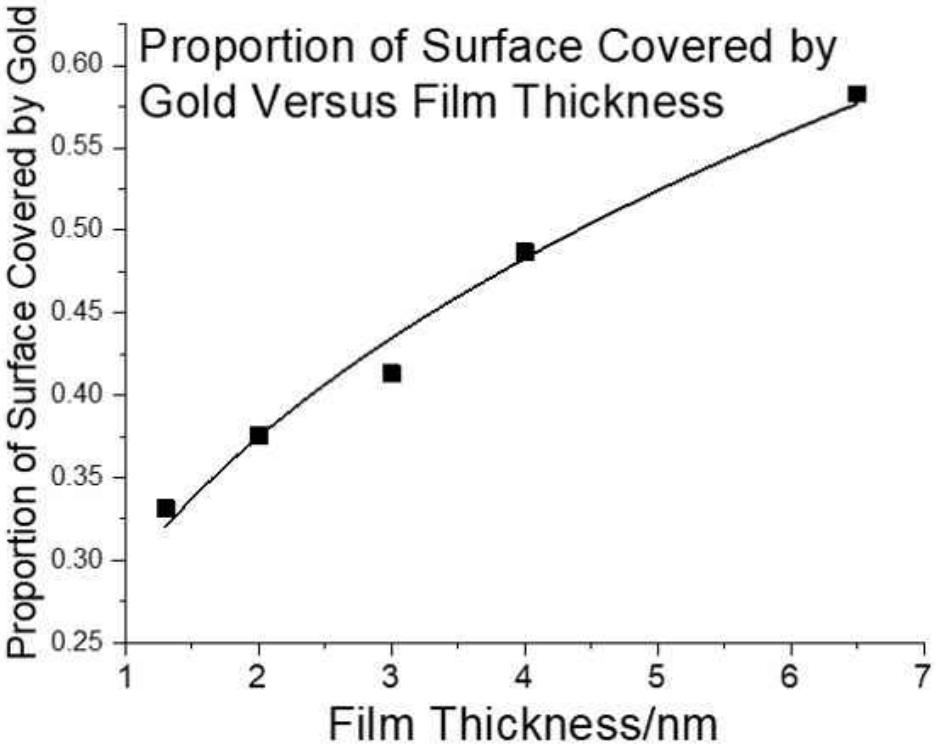

FIGURE 5.2: Plot of the proportion of the silica surface covered by gold nanoparticles as a function of total gold film thickness.

$$N(t) = \frac{2}{\sqrt{3}(s(t) + d(t))^2} \tag{5.3}$$

The area occupied by a particle is $\frac{\pi d^2}{4}$, so that the total area occupied by nanoparticles per unit area is given by:

$$\alpha(t) = \frac{\pi N(t) d(t)^2}{4} \tag{5.4}$$

The value of $s(t)$ is obtained by eliminating $d(t)$ from Eqns. 5.2.4 and 5.2.4 to yield an estimate for the average particle separation as a function film thickness as:

$$s(t) \propto \frac{1}{\sqrt{N(t)}} \left(\sqrt{\frac{2}{\sqrt{3}}} - \sqrt{\frac{4\alpha(t)}{\pi}} \right) \tag{5.5}$$

The results of Eqn. 5.2.4 are compared to those of direct measurements of the nanoparticle spacings measured manually from the SEm images of the nanoparticle covered surface as a function of film thickness in Figure 5.3(■), where the variation in particle separation as a function of film thickness is in accord with the simple analytical model.

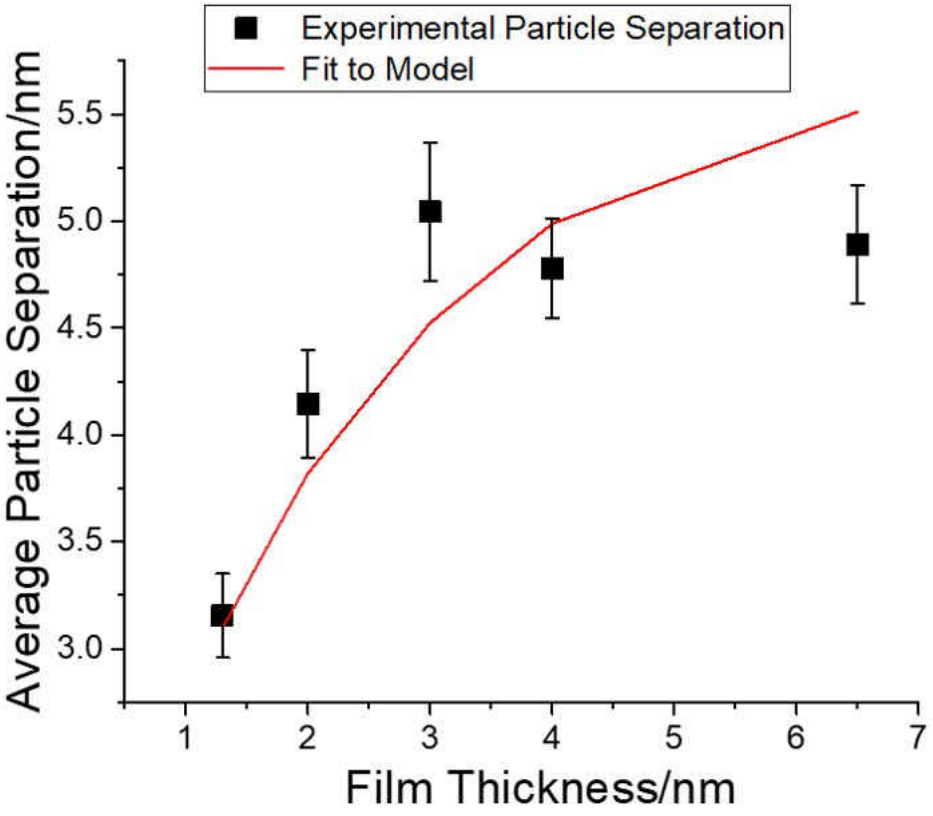

FIGURE 5.3: Plot of average particle separation obtained from Eqn. 5.2.4 (red line, using a scaling factor of 1.25), as a function of total gold film thickness compared with the results of direct measurements of interparticle spacings (■).

5.3 Results and Discussion

Experiments were initially carried out on thin gold films between gold electrodes separated by ~0.25 mm as a function of film thickness. As shown in Figure 5.4, the gold coalesces into nanoparticles, where it is expected that the separation between nanoparticles will very as a function of the film thickness of the gold film. The samples were then exposed to a constant flux of 1,4-PDI and the conductivity of the samples was monitored as a function of time. In all cases, the conductivity of the samples rises with increasing 1,4-PDI dose to reach a satruation conductivity that depends on the thickness of the initial gold film. All samples showed a variation in the conductivity with temperature and a typical plot of the temperature dependence, in this case for a 6.5 nm thick gold film, is shown in Figure 5.5, where $ln\,(\sigma)$ varies as $1/\sqrt{T}$, where σ is the conductivity of the sample and T is the absolute temperature. This behavior has been observed for arrays of gold nanoparticles deposited onto mica [8, 12, 15, 35] and is typical for electron transport through disordered nanoparticle arrays. [39–42]. The conductivity between linked nanoparticles comprises an electron tunneling term that varies as $\sim exp\left(\frac{-E_c}{k_B T}\right)$ where E_c is the Coulomb charging energy, k_B is the Boltzmann constant and T is the absolute temperature and leads to the experimentally observed temperature dependence. [43]

The initial and final conductivities of nanoparticle arrays before and after saturating with 1,4-PDI are displayed in Figure 5.6 as a function of the thickness of the gold film. SEM images of the nanoparticle films were analysed to estimate the average interparticle spacings as a function of film thickness (Section 5.2.4), and the ratio of the final to initial conductivities are plotted versus the estimated interparticle separation inset in Figure 5.6, where conductivity ratios are plotted to take into account the different percolation pathways on the films with different film thicknesses. Extrapolating this line shows the ratio becomes unity at an interparticle separation of 7 ± 2 nm, indicating

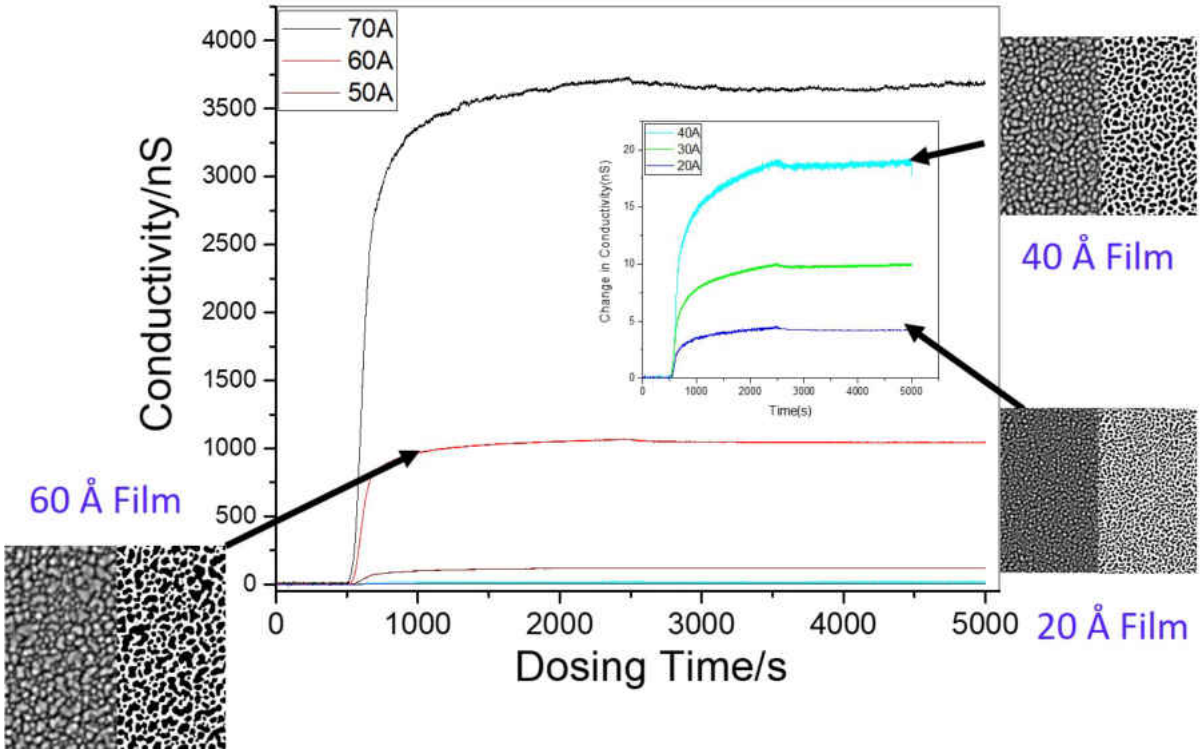

FIGURE 5.4: Plot of conductivity change versus 1,4-PDI dosing time at a background pressure of 1×10^{-8} Torr at a sample temperature of 280 K for various thicknesses of gold evaporated onto a silica substrate, where the film thicknesses are indicated. 1,4-PDI dosing was commenced at 500 s and stopped after 2000 s. The inset shows the data for thinner gold films. Shown also are selected SEM images (400 nm $\times$ 400 nm) of the films where the left-hand part of the images shows the raw data and the right-hand images are processed to more clearly show the nanoparticles.

that the bridging of initially separated gold nanoparticles by conducting -(1,4-PDI-Au)- oligomers is indeed self-limiting.

In order to confirm this, and to more accurately estimate the limiting distance, experiments were carried out using a 30-nm nanogap between gold electrodes as depicted in Figure 5.7. The design of the nanogaps is shown in Figs. 5.7 (a) to (d), where Fig. 5.7(d) shows that the gap separation is $\sim$30 nm. The sample was then saturated

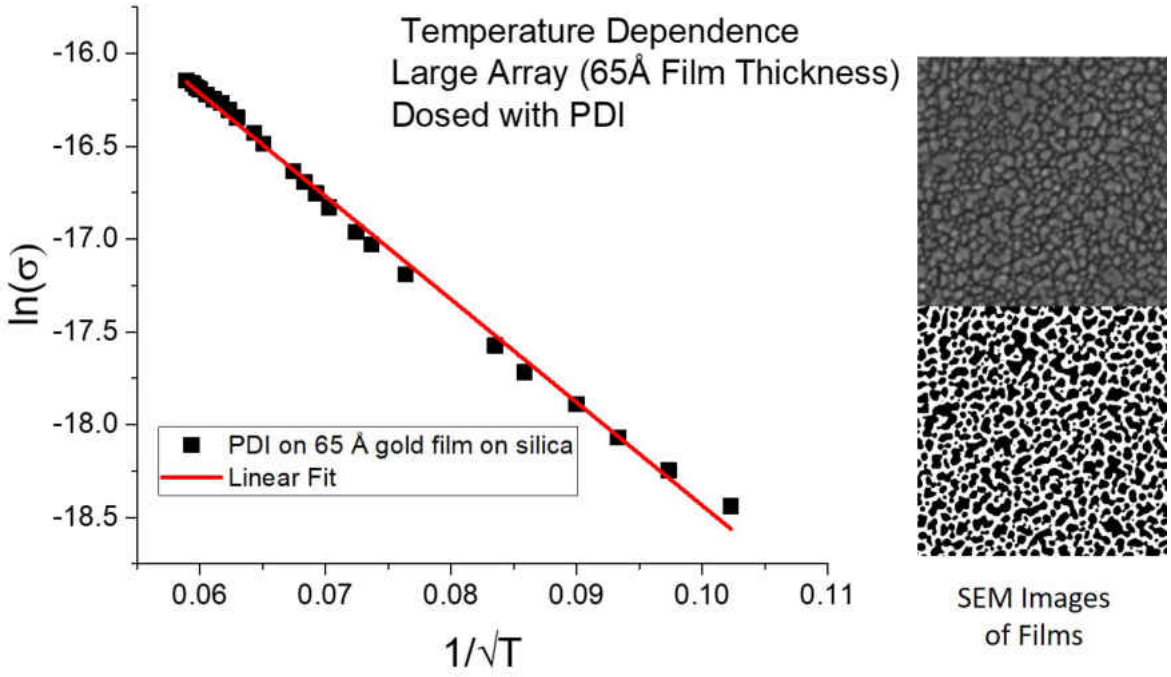

FIGURE 5.5: Plot of $ln(\sigma)$, where σ is the film conductivity, versus $1/\sqrt{T}$ where T is the sample temperature for an array of nanoparticles grown by gold evaporation on a silica substrate dosed to saturation with 1,4-PDI in high vacuum. Shown are SEM images of the film where the top images shows the raw data and the bottom is processed to more clearly show the nanoparticles.

with 1,4-PDI and the I/V curve measured (Fig. 5.7(e)). This shows no conductivity between the electrodes within the detection sensitivity. To determine whether decreasing the gap size leads to bridging by conductive 1,4-PDI oligomers, hybrid devices were fabricated by evaporating a thin film of gold onto the nanogap devices in vacuo. Two types of structures were observed. The first, shown in Figure 5.8B comprised nanoparticles located between the gold nanoelectrodes, highlighted in yellow, where the average diameter d of the nanoparticles between the gold electrodes is 11.2 ± 0.4 nm and $\frac{s}{d} = 0.46 \pm 0.03$, where s is the average interparticle separation. This 1,4-PDI-bridged

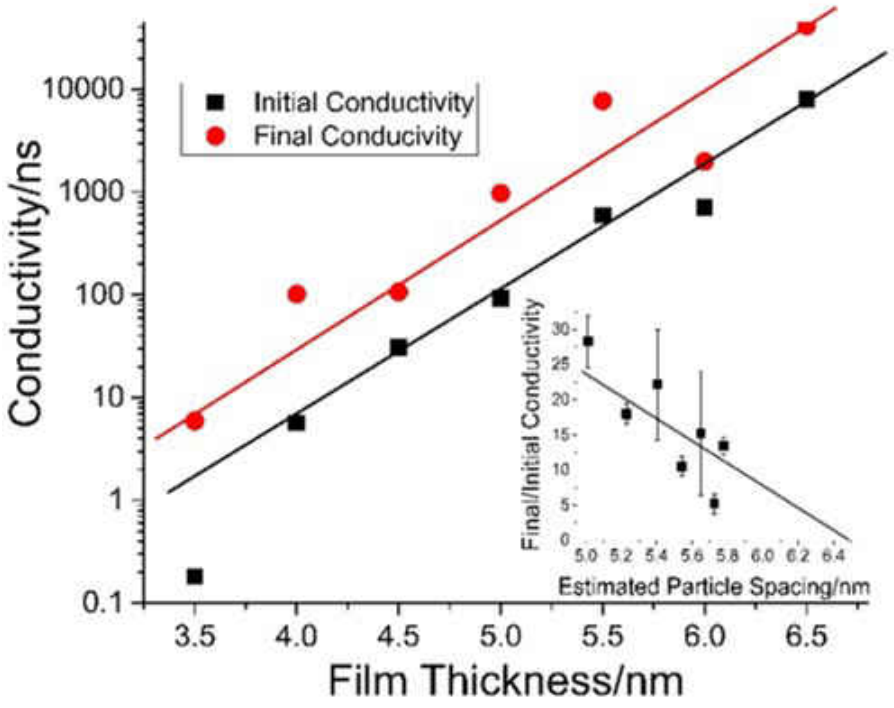

FIGURE 5.6: Plot of the initial and final conductivity for a series of nanoparticle arrays grown by gold evaporation on a silica support in UHV, values shown are for before and after saturation with 1,4-PDI. Shown in the inset is the ratio of final to the initial conductivity plotted versus the estimated particle separation.

hybrid system shows a significant change in conductivity after saturating with 1,4-PDI (Figure 5.8A), indicating that the oligomers can bridge a ∼5 nm gap. This device configuration shows a conductivity that depends significantly on temperature with an Arrhenius dependence (Fig. 5.8C) where $ln(R)$, where R is the low-voltage resistance of the hybrid device, varies linearly with $1/T$, with a slope of 2.02 ± 0.07 kJ/mol. As expected for a system consisting of nanoscale inter-gap nodes, the conductivity has a significant Coulomb charging energy contribution. The Coulomb charging energy is given by:

$$E_c = \frac{e^2}{4\pi\epsilon_0\epsilon} \frac{\frac{s}{d}}{d\left(\frac{1}{2} + \frac{s}{d}\right)} \tag{5.6}$$

where e is the charge on the electron, ϵ_0 is the permittivity of free space and ϵ is the

dielectric constant taken to be 3.5 for 1,4-PDI [44]. This results in a calculated Coulomb charging energy of 1.7±0.1 kJ/mol, in good agreement with experiment.

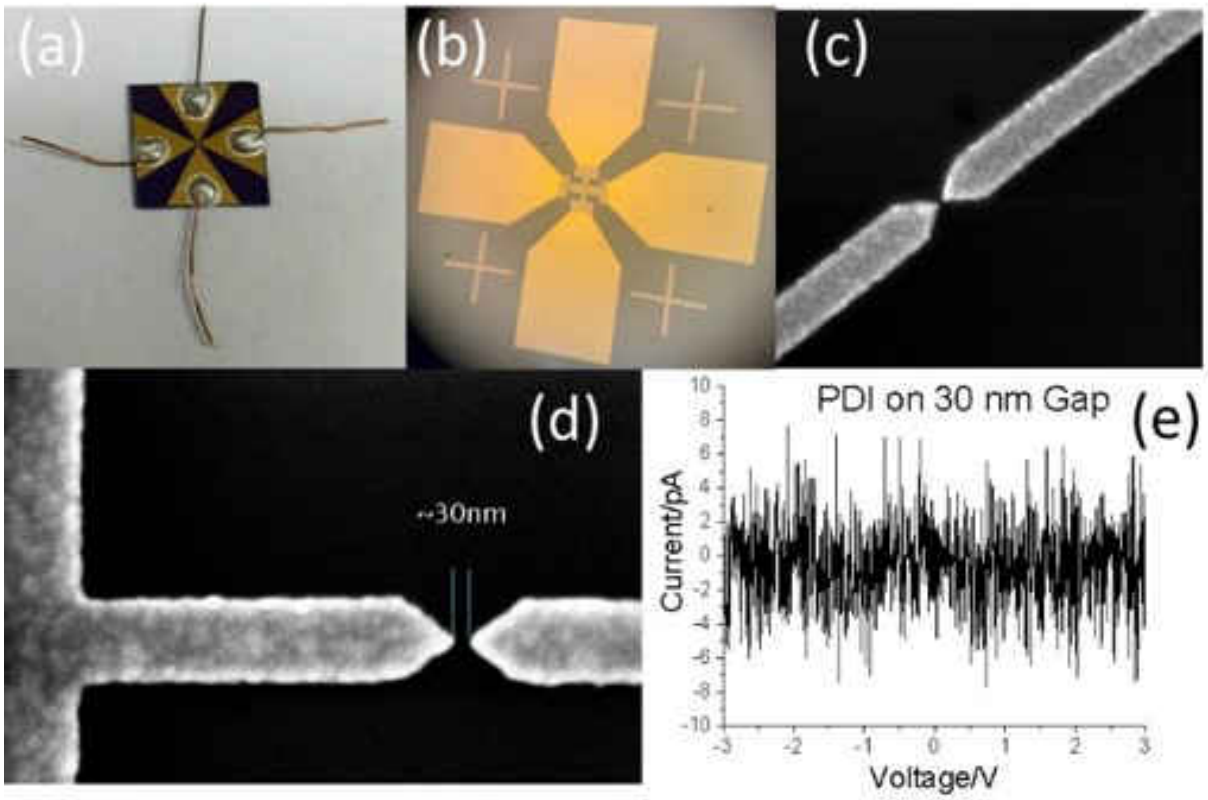

FIGURE 5.7: Depiction of the gold nanogaps fabricated on Silica. (A) shows the wiring of the connection pads, (B) shows the connecting pads and the nanoelectrodes, (C,D) show high-resolution SEM images of the gold nanogaps, and (e) displays an I/V curve after dosing with 1,4-PDI.

A second type of hybrid device was found as shown in Figure 5.9, where the nanoparticles decorate one of the nanoelectrodes (highlighted in yellow in the image shown as an inset to Fig. 5.9) to decrease the nanogap to 9.2±0.3 nm. The resulting I/V curve for a 1,4-PDI saturated gap shown in Fig. 5.9 has a resistance that is close to infinity for $|V| < 1.5$ V, which decreases drastically at higher voltages. This behavior differs from the theoretical [**?**] and experimental [**?**] single-molecule conductivities of gold-bridged 1,4-PDI where the high-resistance region occurs for $|V| < 0.5$ V, in accord with the

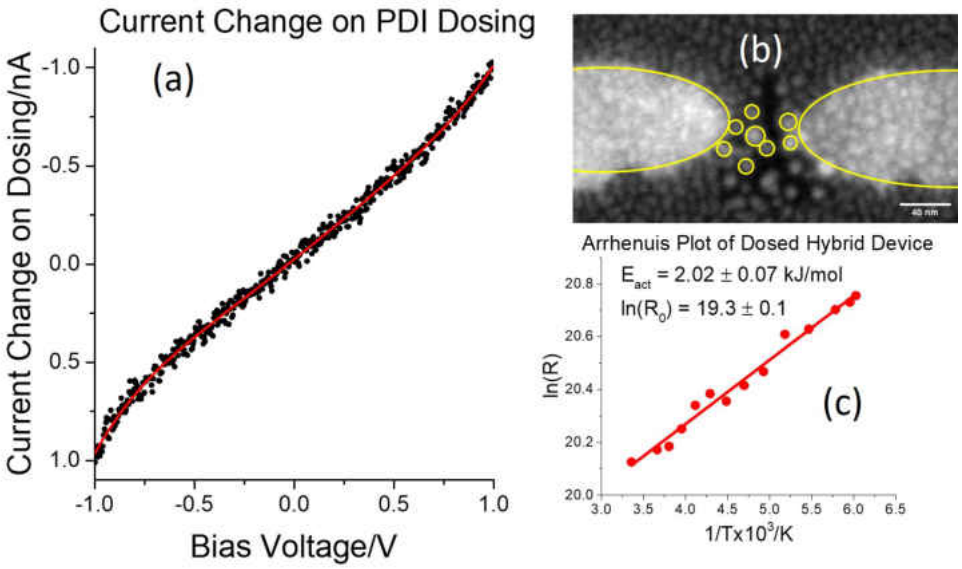

FIGURE 5.8: (a) Plot of the change in the I/V curve for the 1,4-PDI saturated hybrid device shown in (b) the SEM image is 300 nm across the gold nanoelectrodes and nanoparticles in the gap are highlighted in yellow,(c) Plot of ln(R), where R is the resistance of the device, versus 1/T, which shows good Arrhenius behavior. The Coulomb charging energy measured from the slope of the Arrhenius plot is 2.02±0.07 kJ/mol.

linkers between the nanoparticles in the device shown in Fig. 5.9 being oligomeric species, and not single molecules. The I/V curves also show a very weak temperature dependence consistent with the oligomer bridging two nanoelectrodes.

This work tests the postulate that the growth of 1,4-PDI-Au oligomers nucleated by gold nanoparticles is inherently self-limiting because both the nucleation and growth occur at the peripheries of the nanoparticles so that the eventual sturation of the edge sites on the gold nanoparticles by oligomers prevent them from growing, inherently leading to self-limiting growth. Monte Carlo simulations of this process using kinetic parameters previously found for oligomerization on a Au(111) substrate estimated that the maximum gap between gold nanoparticles that could be bridged by oligomers

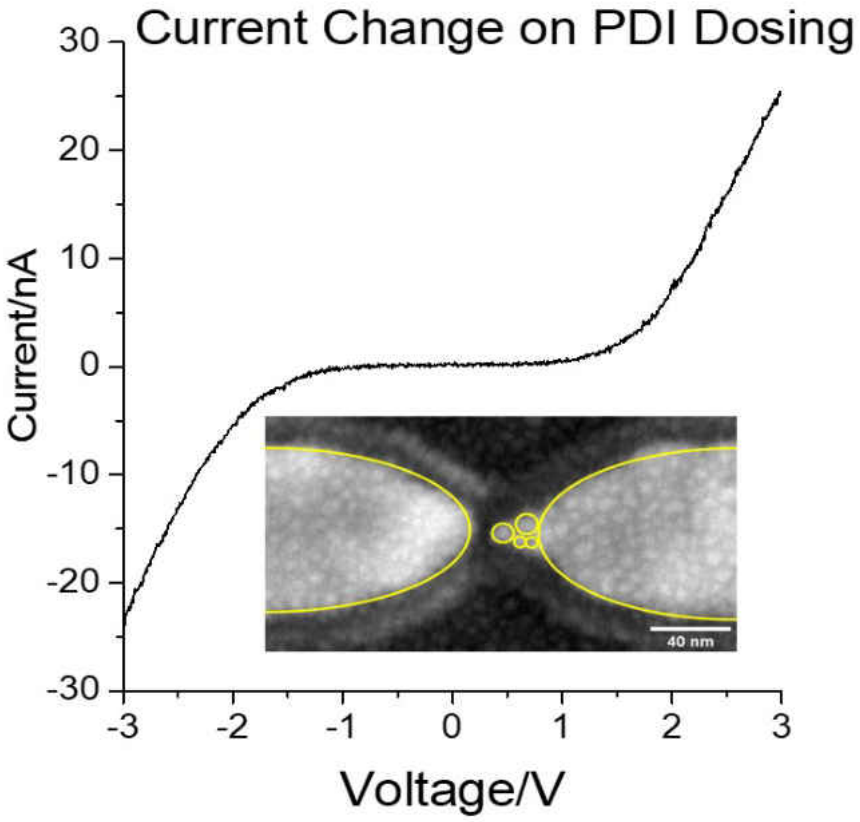

FIGURE 5.9: Plot of the I/V curve for the 1,4-PDI saturated hybrid device shown in the inset, where the gold nanoelectrodes and the gold nanoparticles within the gap are highlighted in yellow. This device shows negligible change in conductivity with temperature.

was ∼10 nm. [4] This postulate was tested on relatively large nanoparticle arrays, discrete nanogaps of ∼30 nm, and hybride devices consisting of thin gold films evaporated onto gold nanogap devices that all produced data that were consistent with this proposal; a nanogap of ∼30 nm showed no conductivity when dosed with 1,4-PDI, while hybrid devices for which the interparticle separations were ∼5 and 10 nm showed a significant increase in conductivity. It should be emphasized that, while there are currently no direct structural measurements of gold-containing oligomers between nanoparticles on silica, such linkages have been directly observed by STM on Au(111), [8] a combination of conductivity measurements on gold nanoparticle arrays

on silica and mica and measurements on hybrid devices allow a preliminary conclusions to be drawn that this approach provides a strategy for fabricating molecular-electronic circuits by judiciously changing the spacings between interconnecting gold nano-electrodes.

5.4 Conclusion

It was found that hybrid devices that contained discrete nanoparticles located within the gap showed an Arrhenius temperature dependence with an activation energy consistent with the calculated Coulomb charging energy, while the narrow gaps without inter-gap particles showed negligible temperature dependence. This suggests that even such simple molecular-electronic architectures can be used as molecular-electronic components. For example, devices containing nanoparticles within the gap (Fig. 5.8) can be used as temperature sensors, while those with narrow gaps with strongly non-linear I/V curves (Fig. 5.9) could find applications as voltage regulators where the regulation voltage can be adjusted by altering the oligomer length by changing the interelectrode separation.

Bibliography

[1] Tina A Gschneidtner, Yuri A Diaz Fernandez, and Kasper Moth-Poulsen. Progress in self-assembled single-molecule electronic devices. *Journal of Materials Chemistry C*, 1(43):7127–7133, 2013.

[2] Arieh Aviram and Mark A Ratner. Molecular rectifiers. *Chemical physics letters*, 29(2):277–283, 1974.

[3] Chad A Mirkin and Mark A Ratner. Molecular electronics. *Annual Review of Physical Chemistry*, 43(1):719–754, 1992.

[4] Dustin Olson, Alejandro Boscoboinik, Sergio Manzi, and Wilfred T Tysoe. Chemical self-assembly strategies for designing molecular electronic circuits: Demonstration of concept. *The Journal of Physical Chemistry C*, 123(16):10398–10405, 2019.

[5] Jorge Boscoboinik, John Kestell, Michael Garvey, Michael Weinert, and Wilfred T Tysoe. Creation of low-coordination gold sites on au (111) surface by 1, 4-phenylene diisocyanide adsorption. *Topics in Catalysis*, 54(1-4):20–25, 2011.

[6] Jorge A Boscoboinik, Florencia C Calaza, Zeesham Habeeb, Dennis W Bennett, Dario J Stacchiola, Martin A Purino, and Wilfred T Tysoe. One-dimensional supramolecular surface structures: 1, 4-diisocyanobenzene on au (111) surfaces. *Physical Chemistry Chemical Physics*, 12(37):11624–11629, 2010.

[7] J Zhou, D Acharya, N Camillone III, P Sutter, and MG White. Adsorption structures and electronic properties of 1, 4-phenylene diisocyanide on the au (111) surface. *The Journal of Physical Chemistry C*, 115(43):21151–21160, 2011.

[8] John Kestell, Rasha Abuflaha, J Anibal Boscoboinik, Yun Bai, Dennis W Bennett, and Wilfred T Tysoe. Linking gold nanoparticles with conductive 1, 4-phenylene diisocyanide–gold oligomers. *Chemical Communications*, 49(14):1422–1424, 2013.

[9] John Kestell, Rasha Abuflaha, J Anibal Boscoboinik, Michael Garvey, Dennis W Bennett, and Wilfred T Tysoe. Determination of adsorbate structures from 1, 4-phenylene diisocyanide on gold. *The journal of physical chemistry letters*, 5(20):3577–3581, 2014.

[10] Alejandro Miguel Boscoboinik, Sergio Javier Manzi, WT Tysoe, Victor Daniel Pereyra, and JA Boscoboinik. Directed nanoscale self-assembly of molecular wires interconnecting nodal points using monte carlo simulations. *Chemistry of Materials*, 27(19):6642–6649, 2015.

[11] Michael Garvey, John Kestell, Rasha Abuflaha, Dennis W Bennett, Graeme Henkelman, and Wilfred T Tysoe. Understanding and controlling the 1, 4-phenylene diisocyanide–gold oligomer formation pathways. *The Journal of Physical Chemistry C*, 118(36):20899–20907, 2014.

[12] Rasha Abuflaha, Dustin Olson, Dennis W Bennett, and Wilfred T Tysoe. Surface chemistry and structures of 1, 4-phenylene diisocyanide on gold films from solution. *Surface Science*, 649:56–59, 2016.

[13] Mitchell J Robertson and Robert J Angelici. Adsorption of aryl and alkyl isocyanides on powdered gold. *Langmuir*, 10(5):1488–1492, 1994.

[14] Kuo-Chen Shih and Robert J Angelici. Equilibrium and saturation coverage studies of alkyl and aryl isocyanides on powdered gold. *Langmuir*, 11(7):2539–2546, 1995.

[15] Rasha Abuflaha and Wilfred T Tysoe. Spontaneous self-assembly of conductive molecular linkages between gold nanoelectrodes from aryl diisocyanides. *Applied Physics A*, 124(11):784, 2018.

[16] Mikio Ito, Hidenori Noguchi, Katsuyoshi Ikeda, and Kohei Uosaki. Substrate dependent structure of adsorbed aryl isocyanides studied by sum frequency generation (sfg) spectroscopy. *Physical Chemistry Chemical Physics*, 12(13):3156–3163, 2010.

[17] BongSoo Kim, Jeremy M Beebe, Yongseok Jun, X-Y Zhu, and C Daniel Frisbie. Correlation between homo alignment and contact resistance in molecular junctions: aromatic thiols versus aromatic isocyanides. *Journal of the American Chemical Society*, 128(15):4970–4971, 2006.

[18] Yan Li, Deyu Lu, Sally A Swanson, J Campbell Scott, and Giulia Galli. Microscopic characterization of the interface between aromatic isocyanides and au (111): A first-principles investigation. *The Journal of Physical Chemistry C*, 112(16):6413–6421, 2008.

[19] Kristen L Murphy, Wilfred T Tysoe, and Dennis W Bennett. A comparative investigation of aryl isocyanides chemisorbed to palladium and gold: An atr-ir spectroscopic study. *Langmuir*, 20(5):1732–1738, 2004.

[20] Jason I Henderson, Sue Feng, Gregory M Ferrence, Thomas Bein, and Clifford P Kubiak. Self-assembled monolayers of dithiols, diisocyanides, and isocyanothiols on gold:'chemically sticky'surfaces for covalent attachment of metal clusters and

studies of interfacial electron transfer. *Inorganica chimica acta*, 242(1-2):115–124, 1996.

[21] Mark A Reed, C Zhou, CJ Muller, TP Burgin, and JM Tour. Conductance of a molecular junction. *Science*, 278(5336):252–254, 1997.

[22] SN Yaliraki, M Kemp, and Mark A Ratner. Conductance of molecular wires: Influence of molecule- electrode binding. *Journal of the American Chemical Society*, 121(14):3428–3434, 1999.

[23] XD Cui, A Primak, X Zarate, J Tomfohr, OF Sankey, Ana L Moore, Thomas A Moore, D Gust, Gari Harris, and SM Lindsay. Reproducible measurement of single-molecule conductivity. *science*, 294(5542):571–574, 2001.

[24] Yongqiang Xue and Mark A Ratner. Microscopic study of electrical transport through individual molecules with metallic contacts. i. band lineup, voltage drop, and high-field transport. *Physical Review B*, 68(11):115406, 2003.

[25] Xiaoyin Xiao, Bingqian Xu, and Nongjian J Tao. Measurement of single molecule conductance: Benzenedithiol and benzenedimethanethiol. *Nano Letters*, 4(2):267–271, 2004.

[26] Manabu Kiguchi, Shinichi Miura, Kenji Hara, Masaya Sawamura, and Kei Murakoshi. Conductance of a single molecule anchored by an isocyanide substituent to gold electrodes. *Applied physics letters*, 89(21):213104, 2006.

[27] Renato B Pontes, Frederico D Novaes, Adalberto Fazzio, and Antonio JR da Silva. Adsorption of benzene-1, 4-dithiol on the au (111) surface and its possible role in molecular conductance. *Journal of the American Chemical Society*, 128(28):8996–8997, 2006.

[28] Makusu Tsutsui, Yumi Teramae, Shu Kurokawa, and Akira Sakai. High-conductance states of single benzenedithiol molecules. *Applied physics letters*, 89(16):163111, 2006.

[29] A Arnold, F Weigend, and F Evers. Quantum chemistry calculations for molecules coupled to reservoirs: formalism, implementation, and application to benzenedithiol. *The Journal of chemical physics*, 126(17):174101, 2007.

[30] Sina Yeganeh, Mark A Ratner, Michael Galperin, and Abraham Nitzan. Transport in state space: Voltage-dependent conductance calculations of benzene-1, 4-dithiol. *Nano letters*, 9(5):1770–1774, 2009.

[31] K Horiguchi, M Tsutsui, S Kurokawa, and A Sakai. Electron transmission characteristics of au/1, 4-benzenedithiol/au junctions. *Nanotechnology*, 20(2):025204, 2008.

[32] Artem Mishchenko, David Vonlanthen, Velimir Meded, Marius Burkle, Chen Li, Ilya V Pobelov, Alexei Bagrets, Janne K Viljas, Fabian Pauly, Ferdinand Evers, et al. Influence of conformation on conductance of biphenyl-dithiol single-molecule contacts. *Nano letters*, 10(1):156–163, 2009.

[33] Youngsang Kim, Torsten Pietsch, Artur Erbe, Wolfgang Belzig, and Elke Scheer. Benzenedithiol: a broad-range single-channel molecular conductor. *Nano letters*, 11(9):3734–3738, 2011.

[34] Renato Borges Pontes, Alexandre Reily Rocha, Stefano Sanvito, Adalberto Fazzio, and Antonio Jose Roque da Silva. Ab initio calculations of structural evolution and conductance of benzene-1, 4-dithiol on gold leads. *ACS nano*, 5(2):795–804, 2011.

[35] Islamshah Amlani, Adam M Rawlett, Larry A Nagahara, and Raymond K Tsui. An approach to transport measurements of electronic molecules. *Applied Physics Letters*, 80(15):2761–2763, 2002.

[36] MSM Saifullah, T Ondarcuhu, DK Koltsov, C Joachim, and ME Welland. A reliable scheme for fabricating sub-5 nm co-planar junctions for single-molecule electronics. *Nanotechnology*, 13(5):659, 2002.

[37] Christopher J Baddeley, Mintcho Tikhov, Christopher Hardacre, Julian R Lomas, and Richard M Lambert. Ensemble effects in the coupling of acetylene to benzene on a bimetallic surface: a study with pd(111)/au. *The Journal of Physical Chemistry*, 100(6):2189–2194, 1996.

[38] Curtis T Rueden, Johannes Schindelin, Mark C Hiner, Barry E DeZonia, Alison E Walter, Ellen T Arena, and Kevin W Eliceiri. Imagej2: Imagej for the next generation of scientific image data. *BMC bioinformatics*, 18(1):529, 2017.

[39] Ping Sheng, B Abeles, and Y Arie. Hopping conductivity in granular metals. *Physical Review Letters*, 31(1):44, 1973.

[40] B Abeles, Ping Sheng, MD Coutts, and Y Arie. Structural and electrical properties of granular metal films. *Advances in Physics*, 24(3):407–461, 1975.

[41] Ping Sheng and J Klafter. Hopping conductivity in granular disordered systems. *Physical Review B*, 27(4):2583, 1983.

[42] CJ Adkins. Conduction in granular metals-variable-range hopping in a coulomb gap? *Journal of Physics: Condensed Matter*, 1(7):1253, 1989.

[43] J Herrmann, DJ Bray, K-H Muller, G Wei, and LF Lindoy. Tuning the coulomb charging energy in cross-linked nanoparticle films. *Physical Review B*, 76(21):212201, 2007.

[44] J Chen, LC Calvet, MA Reed, DW Carr, DS Grubisha, and DW Bennett. Electronic transport through metal–1, 4-phenylene diisocyanide–metal junctions. *Chemical Physics Letters*, 313(5-6):741–748, 1999.

Chapter 6

Surface Chemistry of an Asymmetric Molecular Linker 4-Isocyanophenyldisulfide on Au(111)

6.1 Introduction

In the 1970's, Aviram and Ratner proposed that electronic devices could be fabricated by individual molecules. [1] The simplest architectural basis for molecular electronic components comprises two terminal anchoring groups, often SH or -N≡C groups that bind strongly to gold. To facilitate electron transport through the molecule, the backbone is constructed from π-conjugated systems so that molecules such as 1,4-phenylene diisocyandide (PDI) and 1,4-benzenedithiol (BDT) have been extensively used as prototypes for single-molecule conductivity experments. [2–22]

It has been found that PDI self-assembles on Au(111) to form one-dimensional, oligomeric chains comprising alternating gold and 1,4-PDI units. [23–27] THe propagating monomer for oligomer growth consists of a vertical, mobile Au-PDI adataom complex that oligomerizes by the gold adatom attaching to the isocyanide terminus

of a growing chain. [28] This oligomerization chemistry can be used to form conductive bridges between gold nanoparticles using a similar process in which the PDI extracts gold atoms from the gold nanoparticles to form oligomeric bridges between them. [26, 29] In particular, it has been found that the chain growth between gold nanoparticles is inherently self-limiting since the creation of the Au-PDI adatom complex and the nucleation of oligomer growth both occur at the periphery of the gold nanoparticle. As a consequence, the formation of the adatom complexes is eventually quenched by the formation of growing oligomer chains, thereby preventing the chains from growing further. This provides an ideal strategy for constructing nanoelectronic architectures where the linkages between nanoparticles that can be tailored by adjusting the interparticle separations.

Similar behavior has been found for BDT, another prototypical molecule for examining electron transport through molecules, [8–11, 13, 15, 16, 18–21, 30–36] which, rather than forming SAMS on gold, oligomerize in a similar way by gold adatoms in the chain, to form benzenedithiolate-gold adatom oligomers [36–40],Chapter 7. These junctions are relatively stable for reasonable measurement times and are likely to be formed reproducibly because of the strong Au-S bond.

This raises the possibility of forming similar oligomers when the molecular linker contains different linking groups and of making linkers that have asymmetric electrical properties to from molecular rectifiers. [41] The obvious candidate for testing this idea is to use an asymmetric structure of BDT and PDI, HS-C_6H_4-NC. However it is a synthetic challenge to specifically functionalize such molecules and instead we use 4-isocyanophenyl disulfide (CN-C_6H_4-S-S-C_6H_4-NC)(ICPD)Figure 6.1. In this case, the molecule is expected to adsorb onto gold by cleavage of the weak S-S bond to form thiolate species on the surface, analogous to the chemistry found for dithiols. The following explores the surface chemistry on ICPD on an Au(111) single crystal using

reflection-absorption infrared spectroscopy (RAIRS) and temperature-programmed desorption (TPD).

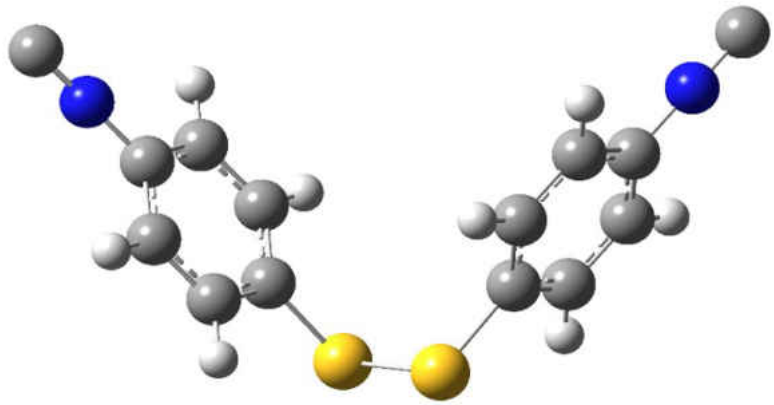

FIGURE 6.1: Optimized structure of gas-phase 4-ICPD.

6.2 Experimental Methods

6.2.1 Synthesis of 4-Isocyanophenyldisulfide (4-ICPD)

4-isocyanophenyl disulfide was prepared by first synthesizing 4-formamidophenyl disulfide. 0.9672 g of 4-aminophenyl disulfide was combined with 40 ml of formic acid and refluxed for 2 days. Formic acid was then removed using a rotary evaporator and the resulting product was stirred with 1 M HCl for ∼1 hour to dissolve any remaining starting material. Insoluble material was filtered and rinsed with distilled water and placed under vacuum to dry giving a 70% yield of crude product this was dissolved in ethanol and filtered while hot. 25 mL of hot toluene was then added, and the solution was concentrated to a total volume of ∼10 mL. The solution was cooled overnight to crystallize, and the resulting crystals were collected by filtration and dried

under vacuum (MP: 157-159 ^{o}C). This was used in a second synthesis to make to make 4,4'-diisocyanobiphenyl disulfide. 4-formamidophenyl disulfide(245.4 mg) was combined with CH_2Cl_2(40 mL) and Et_3N(1.0 mL) in a two-necked, round bottom flask. The apparatus was flushed with nitrogen gas and cooled to 0^oC. To this a solution of triphosgene in CH_2Cl_2(0.176 M, 5.0 mL) was added dropwise over a 5-minute period and refluxed until the starting material disappeared. The mixture was allowed to cool to room temperature and combined with a saturated Na_2CO_3 solution (25 mL) and stirred for 1 hour. The layers were then separated, and the aqueous layer extracted with CH_2Cl_2. The organic layers were combined and washed with a pH 7 buffer, dried over $MgSO_4$ and concetrated to dryness. The product was initially purified on silica gel and crystallized from hexanes:CH_2Cl_2(2:1, 6 mL).

6.2.2 Ultrahigh and High Vacuum Experiments

Experiments were carried out in ultrahigh vacuum (UHV) using an Au(111) single crystal (Princeton Scientific) that was cleaned with cycles of ion bombardment using 1 keV argon ions for 30 minutes (1 $\mu A/cm^2$), annealing to 900 K for 5 minutes and then to 600 K for 30 minutes. Temperature-programmed desorption (TPD) and reflection-absorption infrared spectroscopy (RAIRS) measurements were made in separate ultra-high vacuum (UHV) chambers operating at base pressures of $\sim 2 \times 10^{-10}$ Torr after bakeout. RAIRS experiments were carried out in a Bruker Equinox spectrometer, typically for 1000 scans at a resolution of 4 cm^{-1} as described elsewhere [42]. The sample could be cooled to $\sim$80 K in both chambers by thermal contact to a liquid-nitrogen-filled reservoir and resistively heated to $\sim$ 1200 K. This chamber was also equipped with a Hiden quadrupole mass spectrometer for leak checking, monitoring the purity of the introduced gases and for carrying out temperature-programmed desorption experiments. ICPD, as prepared as in Section 6.2.1 was purified by heating under high

vacuum and introduced into UHV via a gate valve isolating a crucible source containing the ICPD sample.

6.3 Results

The surface chemistry of ICPD adsorbed on a Au(111) surface is investiaged to ascertain whether ligation onto the surface is initiated by S-S scission to form adsorbed thiolate species [43] or whether the molecule is bound via the isocyanide group. The nature of the initial precusor will influence the subsequent putative oligomerization chemistry. For example, if the formation of the initial precursor occurs exclusively by thiolate formation, subsequent oligomerization is anticipated to lead to aligned Au-ICPD oligomers. It has also been suggested that the oligomer formation kinetics can be influenced by an imposed electric field acting on a dipolar adsorbate [28] possibly leading to aligned asymmetric oligomers that could exhibit asymmetric conductivity.

The desorption behavior is studied by TPD by monitoring 268 amu (the parent mass of ICPD) and 134 amu (the CN-C_6H_6S fragment). The desorption profiles were identical for both masses, while the 134-amu signal was the most intense, and the desorption profiles collected at this mass are shown plotted as a function of exposure in Figure 6.2. The presence of both 268 and 134 amu fragments indicates that the desorption profiles are due to the desorption of molecular ICPD from the surface. No other desorption products were detected implying that the desorption is reversible and is in accord with the proposal that ICPD adsorbs by S-S bond scission and desorbs in two states, centered at $\sim$400 and 467 K. The formation of dithiols from the recombinative desorption of adsorbed thiolates on Au(111) has beeen observed previously for alkyl thiols [44] where desorption occurs in two states with the low-temperature state being due to the evolution of a thiolate with first order kinetics, while a high-temperature desorption state is due to the formation of the dithiol with second-order kinetics. Since

both desorption states for ICPD are due to molecular desorption, the surface chemistry of ICPD appears to differ from that for simple alkyl thiolates so that the desorption profiles were fit to two second-order processes. Such desorption kinetics will give rise to symmetric desorption profiles [45] and, while the desorption features overlap at higher ICPD coverage, the low-coverage profiles are symmetric, in accord with the proposed second-order kinetics. Since the area under the desorption profile scales with coverage the TPD data in Figure 6.2 are shown and plotted as a function of relative ICPD coverage. The profiles were fit using the Polanyi-Wigner equation, $-\frac{d\theta}{dt} = A\theta^2 \exp \frac{-E_{act}}{k_B T}$ for a second-order kinetics for a linear heating rate of 5 K/s, where A is a pre-exponential factor, E_{act} is the desorption activation energy, k_B is the Boltzmann constant and,T the absolute temperature. The Polanyi-Wigner equation was numerically integrated over small time steps, where the time steps were varied to be sufficiently small so that no differences were found in the shapes of the calculated desorption profiles and fit to two desorption processes, Appendix A summarized the code used for the calculations. The resulting fits to the data are shown as solid lines that overlay the experimental profiles.

The resulting relative coverages of each of the adsorption states are displayed in Figure 6.3. This shows that only the high-temperature (∼467 K) desorption state is present for ICPD coverages below ∼0.2 ML, after which both the low-(∼400 K) and high-(∼467 K) temperature desorption states grow approximately linearly with total ICPD coverage. The corresponding desorption activation energies are plotted as a function of ICPD coverage in Figure 6.3B. The desorption activation energy of the high-temperature state initially increases up to a relative ICPD coverate of ∼0.1 ML from ∼93 kJ/mol to ∼99 kJ/mol, but then remains constant at this value close to saturation coverage where it increases slightly to ∼101 kJ/mol. The low-temperature state has a desorption activation energy of ∼ 88 kJ/mol, again showing a slight increase as the overlayer approaches saturation coverage.

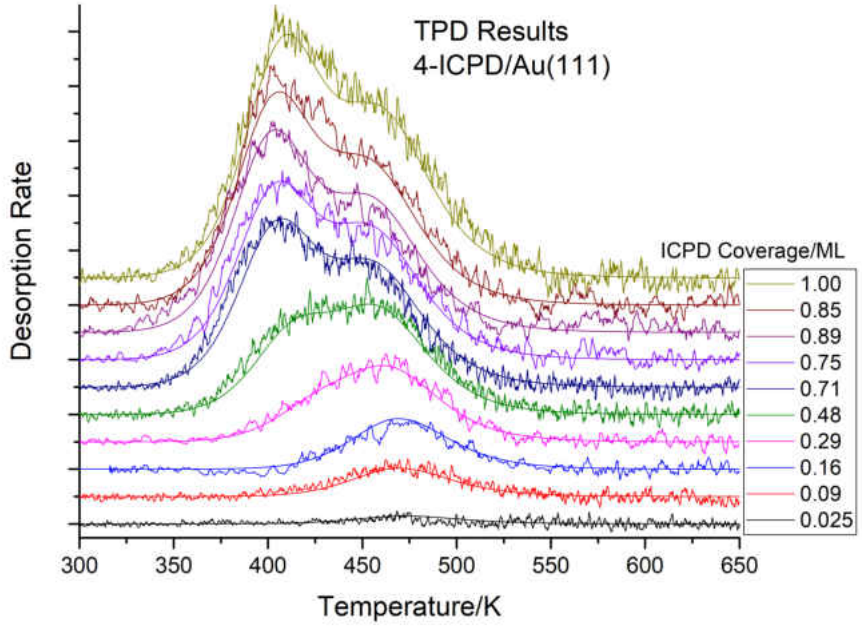

FIGURE 6.2: Desorption profiles of ICPD adsorbed on Au(111) at 300 K using a heating rate of 5 K/s monitored at 134 amu as a function of ICPD dose. The spectra are shown plotted as a function of relative ICPD coverage by assuming that the area under each curve is proportiona to the coverage of adsorbed ICPD.

RAIRS was used to monitor the surface species obtained from ICPD adsorption. The infrared spectra were continually recorded at a sample temperature of 300 K while dosing ICPD directly from a crucible source heated to 353 K, where the source was degassed for 30 min prior to exposure, by recording spectra at a rate of 1/min with a resolution of 4 cm^{-1} for 350 scans. The results are displayed in Figure 6.4 and show features at 829, 1011, 1072, 1482, 1576, 2121 and 2153 cm^{-1}. The spectra were assigned using previous assignments of PDI [2,27,46] and 1,4-BDT [36] and supplemented using vibrational frequencies calculated by Gaussian and the assignments are summarized in Table 6.1. Of particular interest are the isocyanide modes at 2153 and 2121 cm^{-1}, where the feature at 2121 cm^{-1} is due to a free isocyanide, while that at $\sim 2153^{-1}$ is due to an isocyanide bound to gold. This spectral region is highlighted in Figure 6.5(A) to

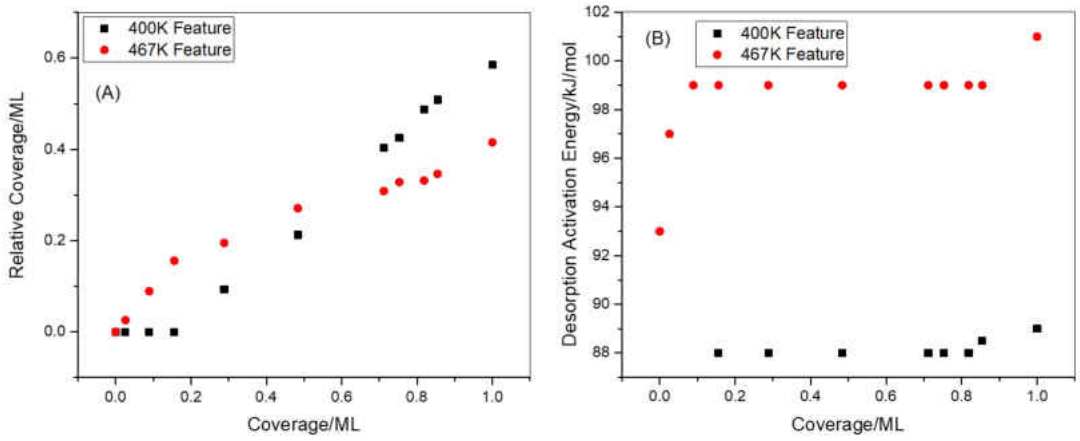

FIGURE 6.3: A. Plot of relative coverages of the 400(■) and 467(•) K features as a function of the relative coverages of ICPD on Au(111) obtained from the fitted profiles to the TPD data in Figure 6.2 B. Plot of the desorption activation energies of the 400(■) and 467(•) K features as a function of relative coverages of ICPD on Au(111) from the fitted profiles in 6.2.

more clearly show the evolution of the isocyanide stretching features as a function of exposure. The peaks in the spectra were fit to Gaussian functions and the relative integrated intensities of the components are shown in Figure 6.5(B). This reveals that ICPD adsorbs at low exposure ($\leq 0.5L$) to initially only form adsorbates with free isocyanide modes (■). However, bound isocyanides (•) start to form at higher exposures as the coverage of free isocyanide saturates at an exposure of ∼0.5 ML, while the coverage of bound isocyanides continues to grow up to an exposure of ∼1.2 L. Note that the integrated absorbance of the bound isocyanide mode is larger than that of the free isocyanide vibration at saturation. Since the free isocyanide is likely to be oriented more perpendicularly to the surface than the bound isocyanide and to therefore adsorb infrared radiation more strongly, [47] the coverage of the bound isocyanides is likely to be greater than the free species. In addition, in the case of PDI oligomers on Au(111), where the aryl group lies parallel to the surface, only a 813 cm $^{-1}$ out-of-plane ring

mode is detected, while additional ring modes are observed for ICPD. However, gold-containing oligomers obtained from 1,4-BDT on Au(111) does exhibit additional ring modes at 1182 and 1108 cm^{-1} due to distortion of the ring from being planar to the surface induced by the hybridization of the sulfur-gold linkages [36].

ICPD Vibrational Frequency/cm^{-1}					
Solution IR	**Multilayer ICPD**	**Monolayer ICPD**	**DFT**	**Assignment**	**Symmetry**
		2155		Bound-NC	
2122	2131	2121	2126	Free-NC	
1586	1589	1576	1629	C=C	
1570	1570	1570	1593	C=C	
1484	1484	1482	1524	In-plane C-H Bend	B_{1u}
1402	1403			In-plane C-H	B_{2u}
1302	1301				
1194	1197				
1167	1166				
1115	1114			In-plane C-H	B_{2u}
1101	1101				
1075	1076	1072	1084		
	1047		1044	In-plane ring	
1014	1014	1011	1016	In-plane C-H	B_{1u}
956	915			Out of plane wag	
941	898			Out of plane wag	
817	831	829	875	Out of plane	B_{3u}
	738		745	Ring chair mode	
667	669				
586			586	C-S Stretch	
508			516	NC Rocking	
486			475	Disulfide	

TABLE 6.1: Assignments of the infrared spectra of multilayar and solution-phase ICPD, and ICPD adsorved on Au(111) at 300 K. The vibrational frequencies were calculated for the structure optimized using Gaussian 09 software package [48] and the optimized structure of molecular ICPD is shown in Figure 6.1.

In order to correlate the presence of the surface species with the desorption profile (Figure6.2), an ICPD-saturated overlayer was heated at a ramp rate of 5 K/min while recording spectra at a rate of 1 spectra/min with a resolution of 4 cm^{-1} for 350 scans and the results are displayed in Figure6.6. This shows a general decrease in intensity of all the vibrational modes due to the removal of ICPD from the surface. There are

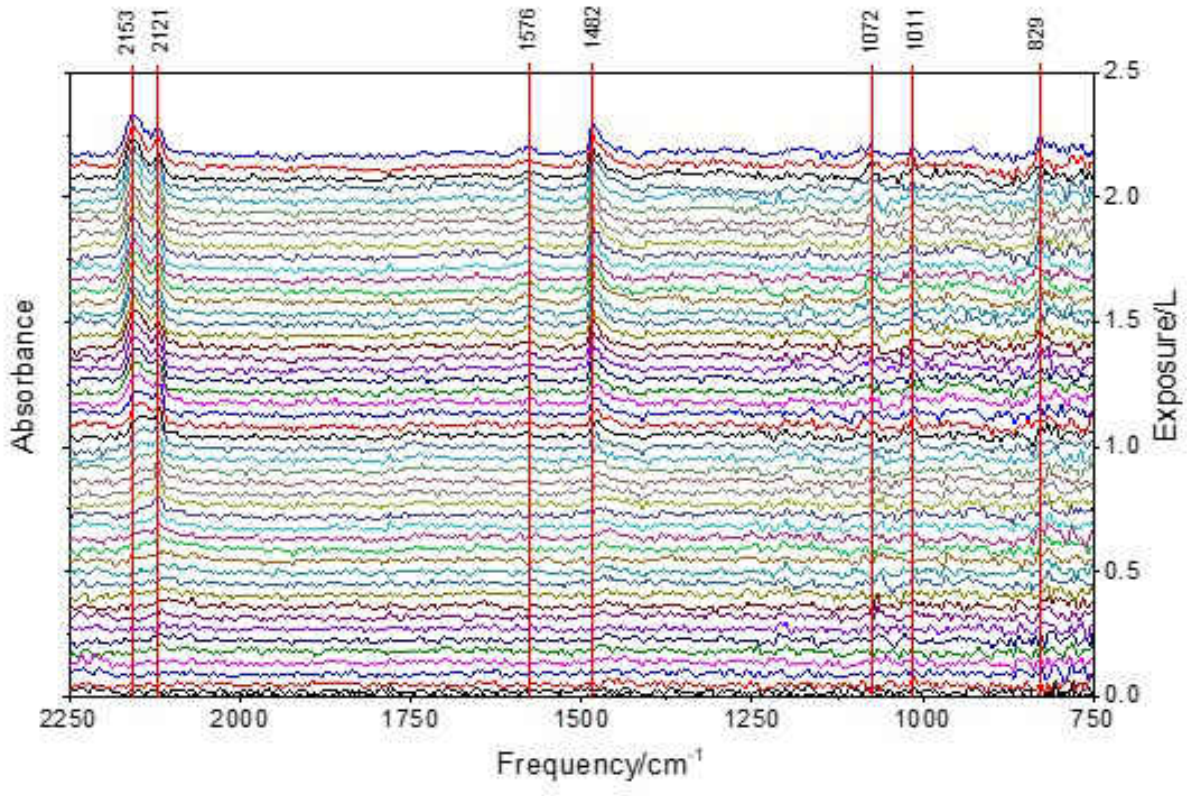

FIGURE 6.4: Infrared spectra of the uptake of ICPD at a sample temperature of 300 K as a function of exposure. ICPD was dosed from a crucible located in the infrared cell and was heated to 353 K and was degassed for 30 min prior to exposure. Spectra were continually recorded at a rate of 1/min with a resolution of 4cm^{-1}, and ∼350 scans/spectra. The corresponding ICPD exposures are indicated on the right hand axis of the figure.

particularly significant changes in the relative intensities of the isocyanide stretching modes, which are highlighted in Figure 6.6A. This shows that the feature at ∼2153 cm^{-1} due to the bound isocyanide decreases in intensity with increasing temperature more rapidly than the mode at 2121 cm^{-1}, due to a free isocyanide. This behavior is emphasized by the plot of the integrated areas in Figure 6.6B, showing that the peak due to the bound isocyanide (•) starts to decrease in intensity as the sample is heated above ∼300 K while the intensity of the free isocyanide mode (■) remains constant in intensity up to ∼400 K, and then rapidly attenuates. Note that the removal of the free

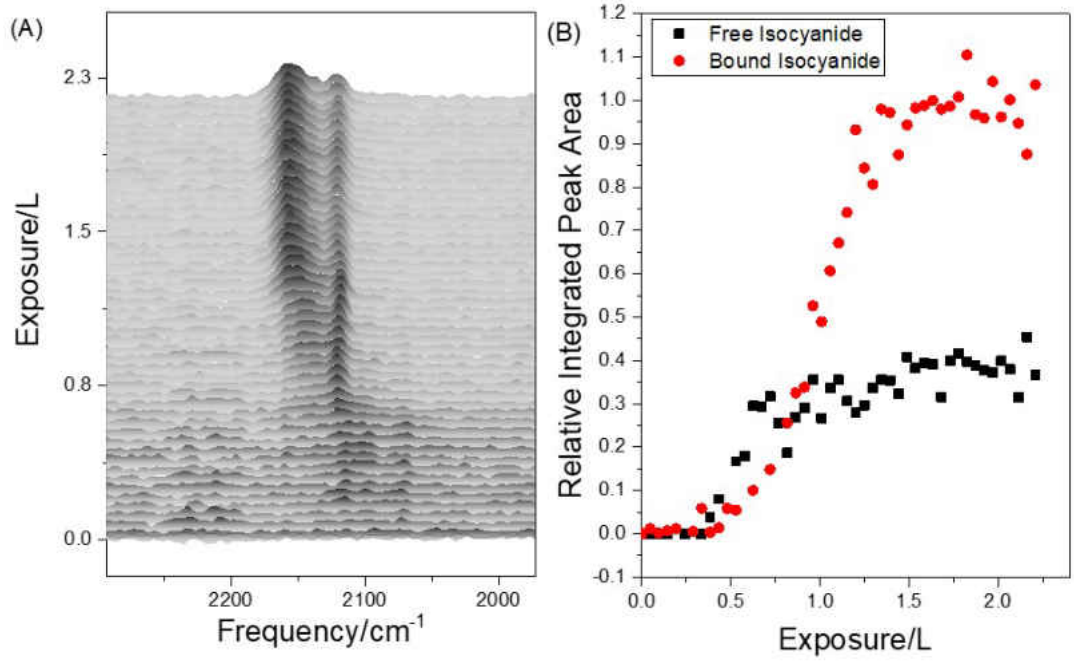

FIGURE 6.5: (A) Infrared spectra of ICPD as a function of exposure showing the isocyanide stretching region displaying the free (2121 cm^{-1}) and bound (2155 cm^{-1}) isocyanide modes and (B) plots of the integrated intensities of the free (■) and bound (•) isocyanide modes as a function of exposure.

and bound isocyanides on Au(111) are the reverse of the adsorption behavior (6.5), where the free isocyanide species are formed initially during adsorption (Fig.6.5B), but are removed at the highest temperature, after the bound species has disappeared (Fig. 6.6B).

Finally, to explore the transitions occurring at lower temperatures, temperature dependent infrared spectra were collected for a multilayer of ICPD on Au(111)6.8. The spectral features obtained for the multilayer at low temperatures are identical to those found for ICPD in solution(6.1). The infrared spectrum does not change on heating to ∼-200 K, but significant changes occur at higher temperatures. In particular, the skeletal features at 1486 and 832 cm^{-1}, as well as that due to the free isocyanide (2123 cm^{-1}),

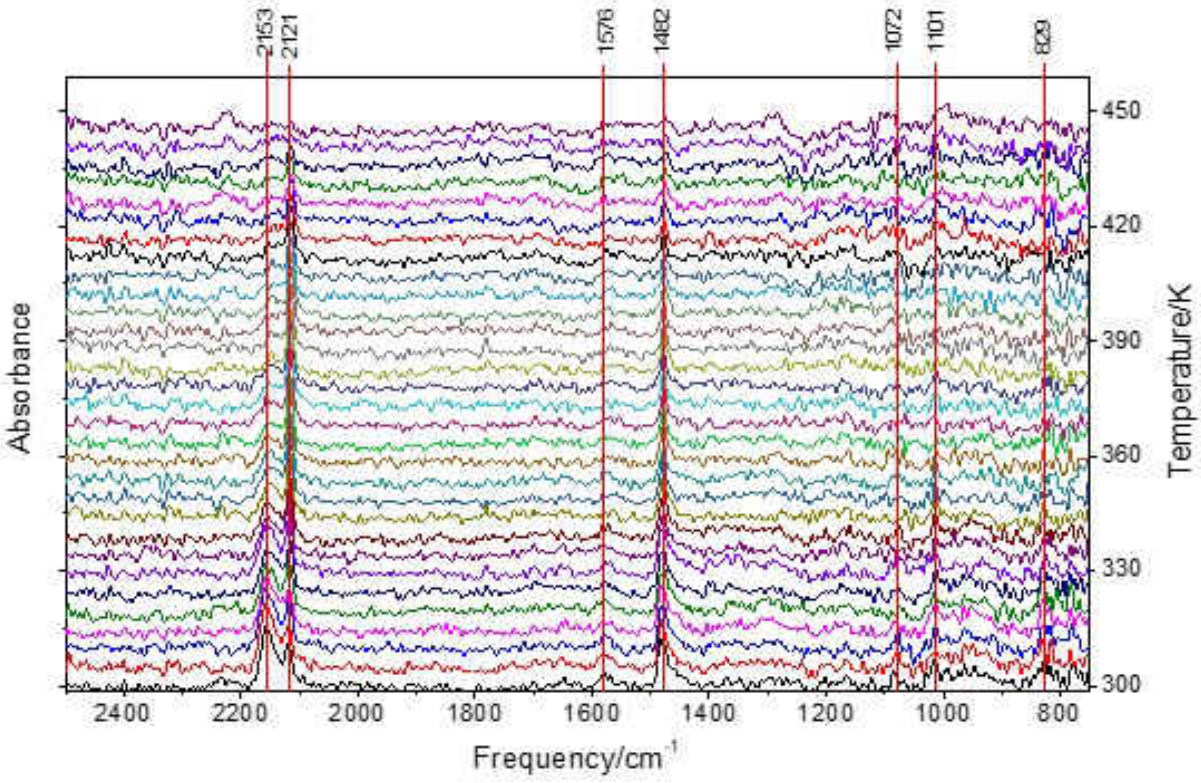

FIGURE 6.6: Infrared spectra of a saturated monolayer of ICPD adsorbed at 300 K on Au(111) and heating at a linear rate of 5 K/min. The infrared spectra were recorded at a rate of 1/min with a resolution of 4cm^{-1}, and ∼350 scans/spectra. The corresponding sample temperatures are indicated on the right-hand axis of the figure.

all increase in intensity. The symmetry of para-substituted aryl rings is described by the D_{2h} point group, where the corresponding irreducible representations of the infrared active modes are given in Table 6.1. The variation in the relative intensity of the most drastically varying modes is displayed in Figure 6.9. The intensity of the free isocyanide stretching mode (at 2123 cm^{-1}, blue line) increases in two stages starting at ∼210 K and then increases again to have a maximum intensity at ∼267 K, and then decreases in intensity at ∼289 K, due to the desorption of the multilayer. This confirms that the spectra in Fig. 6.4 is due to ICPD adsorbed on the surface and does not contain contributions from the multilayer. This also suggests that the isocyanide group on

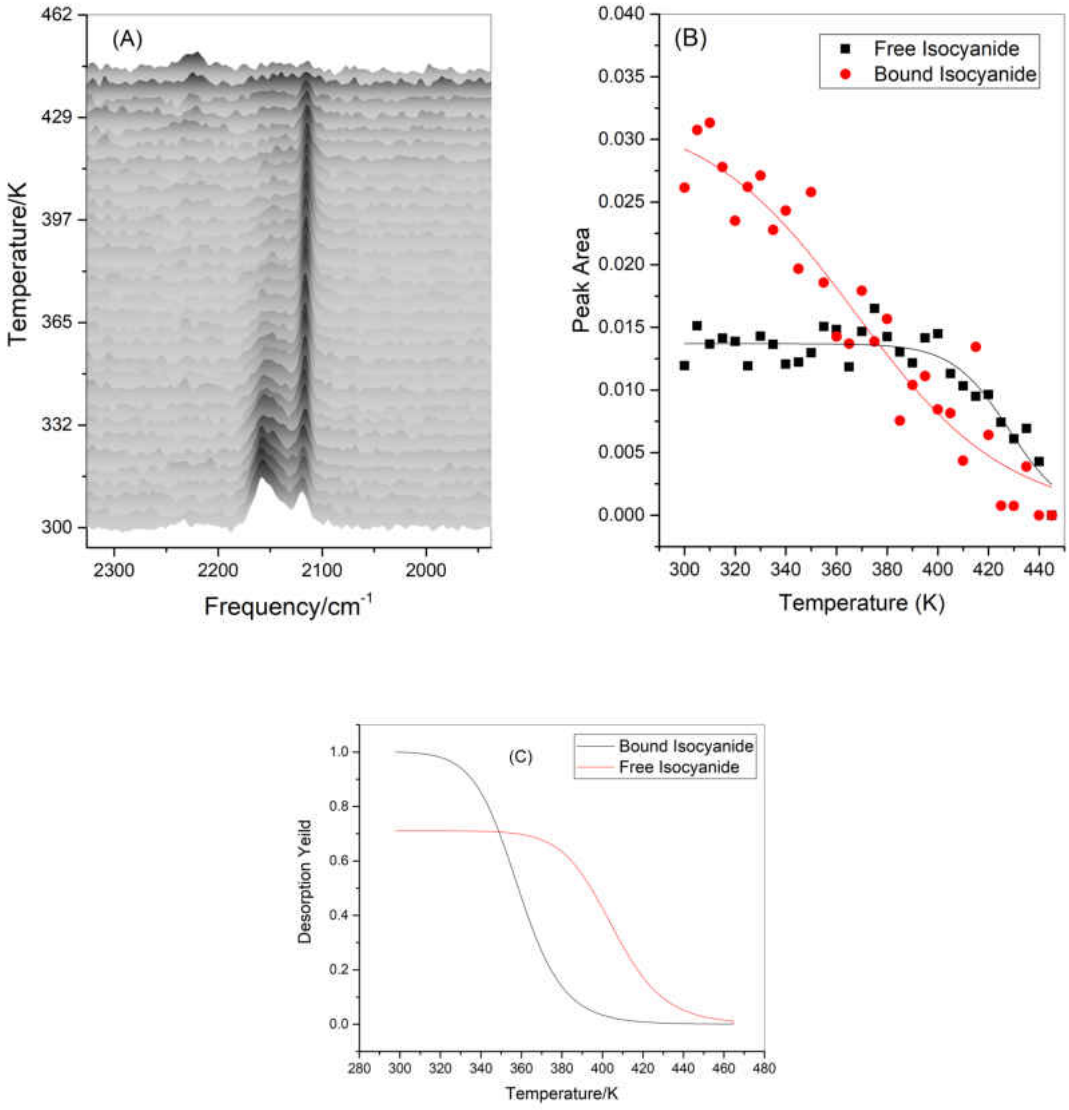

FIGURE 6.7: (A) Infrared spectra of ICPD as a function of temperature showing the isocyanide stretching region displaying the free (2121 cm^{-1}) and bound (2155 cm^{-1}) isocyanide modes and (B) plots of the integrated intensities of the free (■) and bound (•) isocyanide modes as a function of temperature.C) shows the relative coverages of the free (■) and bound (•) isocyanide species as a function of temperature from the parameters used to fit the TPD data (Fig. 6.2) using a heating rate of 5 K/min used to collect the infrared spectra.

ICPD becomes oriented more closely to parallel to the surface. Since the pendant isocyanide group is colinear with the z axis of the aryl ring, B_{1u} modes (at 1482 and 1014

cm^{-1}, Table 6.1) that transform as z are expected to change similarly in intensity as the isocyanide mode. This is illustrated by the change in intensity of the most-intense B_{1u} mode at 1486 cm^{-1}(Fig. 6.9, blue line), which mirrors the change in intensity of the isocyanide stretching vibration. This intensity change is mirrored by the intensity variation of the less intense 1014 cm^{-1} mode (Fig. 6.8.

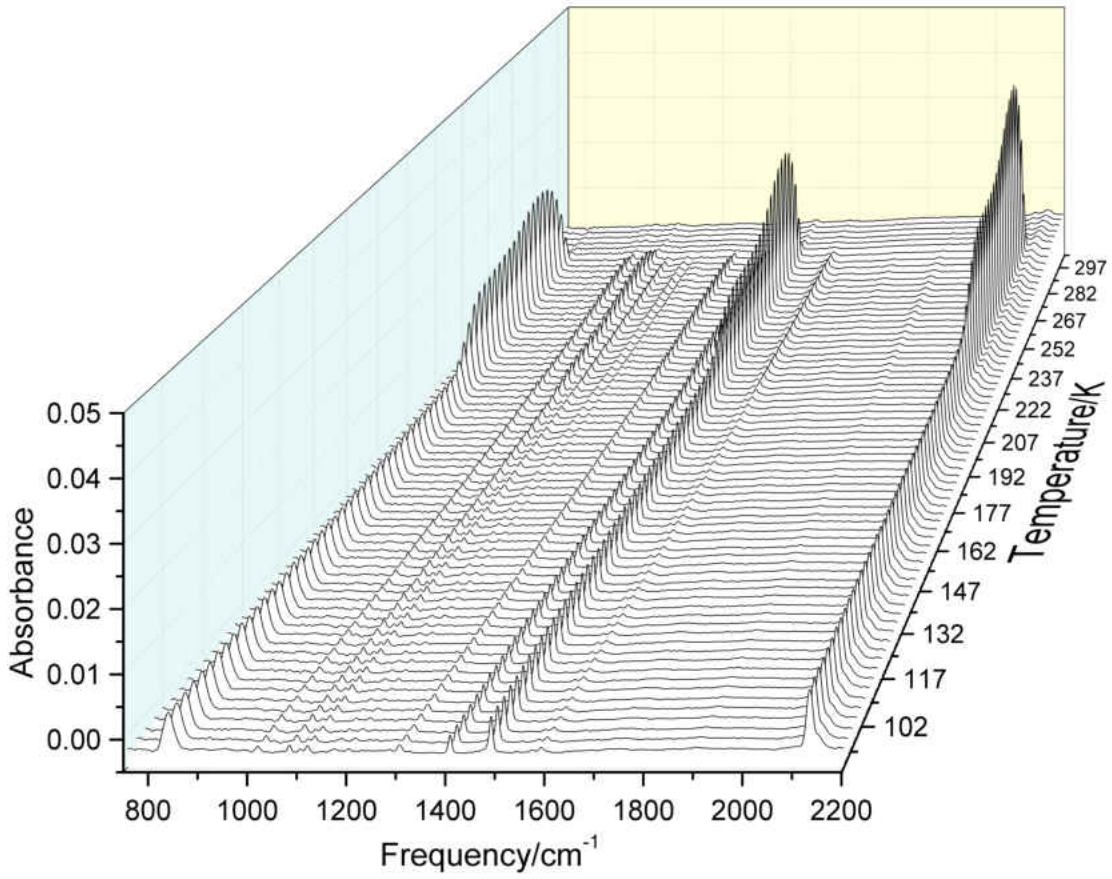

FIGURE 6.8: Infrared spectra of multilayers of ICPD adsorbed on Au(111) to prevent water adsorption then cooled to 90K. The temperature was then ramped at 3K/min and spectra were recorded at a rate of 1 min/spectra

However, modes that transform as y (which bisects the aryl ring and is oriented perpendicular to the plane of the ring) at 1403 and 1114 cm^{-1} show little change in

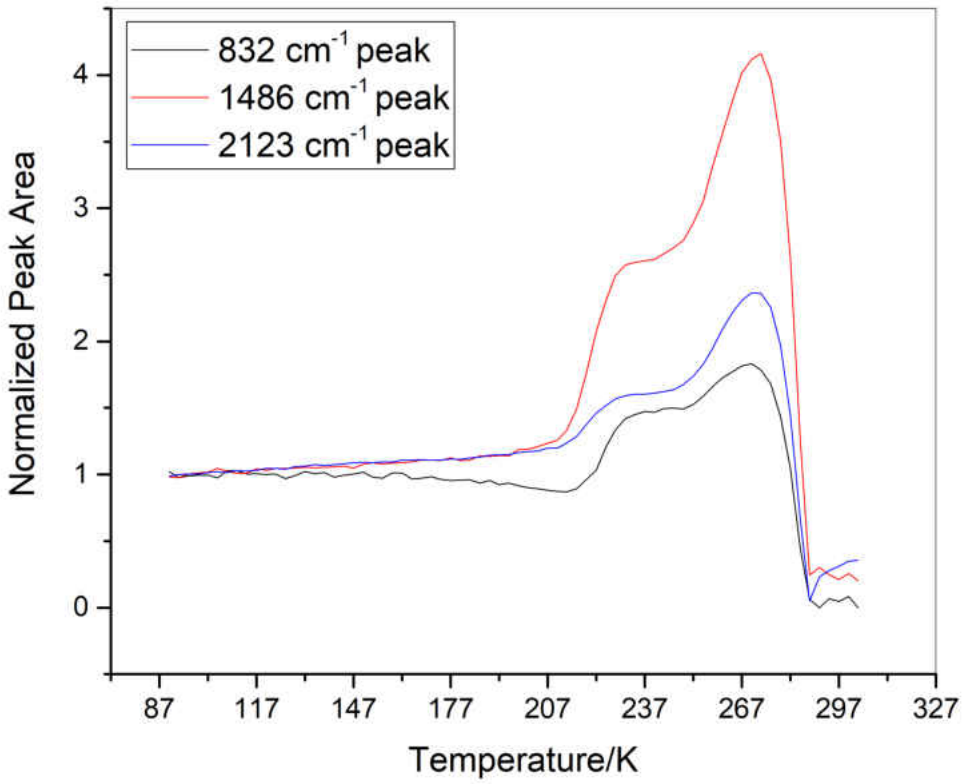

FIGURE 6.9: The integrated areas of selected peaks from the spectra shown in Fig. 6.8, where the areas were obtained using Gaussian fits to the spectral profiles for the 2123 cm^{-1} (free isocyanide mode, blue trace), 1486 cm^{-1} (in-plane ring mode, red trace) and 832 (out-of-plane ring mode, black trace) peaks.

intensity with heating (Fig. 6.8). However, if the plane of the z axis of the para-coordinated aryl ring were perpendicular to the surface, vibrational modes that transform as x (which lies perpendiuclar to the aryl ring with B_{3u} symmetry) should also not change with temperature. However, the intense mode at 832 cm^{-1}, B_{3u}, mirrors the 2123 and 1486 cm^{-1} modes (Fig. 6.9, black line), indicating that the aryl plane of the aryl ring is tilted with respect to the surface. These changes suggest that the -SC_6H_4-NC moiety becomes more ordered on heating above ~200 K. However, a small additional peak appears at ~2155 cm^{-1} on heating above ~200 K (Fig. 6.8) assigned to

a bound isocyanide, implying that oligomerization also occurs as soon as the S-S bond scission takes place in ICPD.

6.4 Discussion

Previous work has shown that PDI oligomerizes by forming a mobile gold-adatom complex that forms oligomers by the gold adatom inserting into the isocyanide terminus of a growing chain to form linear, conductive gold containing oligomers. [28] A key indicator for the formation of such self-assembled oligomers is the appearance of an isocyanide mode that is shifted to higher frequencies than that for a free isocyanide vibration (of 2121 cm^{-1}). The isocyanide streching mode for two isocyanide groups located trans to a gold adatom in the oligomer varies from $\sim$2150 cm^{-1} at low PDI doses to $\sim$2137 cm^{-1} at saturation. [27] This effect is ascribed to a coupling between isocyanide groups in adjacent PDI molecules in the linker, where short chains exhibit a N$\equiv$C stretching frequency of $\sim$2153 cm^{-1} at low doses and $\sim$2137 cm^{-1} for long chains. However, isocyanide containing self-assembled monolayers, presumably similar to the adatom complex show isocyanide frequencies at $\sim$2180 cm^{-1}.

Similar oligomers are formed from BDT implying that the dithiol similarly forms mobile gold-containing complexes [37, 38, 40] that oligomerize in a similar fashion as that proposed for PDI. In order to provide similar oligomer, but with asymmetric molecules we used ICPD (Fig. 6.1), which contains pendant isocyanide groups, but a disulfide rather than an S-H group based on the idea that disulfides and thols bind similarly to gold, [49, 50] and should therefore exhibit similar chemistry as thiols. It is also anticipated that the S-S linkage should be labile, thus resulting in the preferential formation of a sulfur-linked adatom complex that should, according to the kinetic model outlined above, lead to the formation of aligned, conductive oligomers.

TPD indicates the desorption of ICPD in two states centered at ∼400 and 467 K (Fig. 6.2), where the ICPD is formed via second -order kinetics. This is in general accord with the idea that the ICPD adsorbs dissociatively, where ICPD is reformed by the second-order reaction of the fragments with activation energies of ∼88 and 99 kJ/mol (Fig. 6.3B). The relative contributions of the desorption states as a function of coverage are given in (Fig. 6.3A), where up to coverages of ∼0.3 ML desorption is due exclusively to the high-temperature state (∼467 K), afterwards desorption occurs simultaneously from both states.

In order to identify the nature of the surface species formed following ICPD adsorption, infrared spectra were collected as a function of ICPD exposure at 300 K (Fig. 6.4), revealing the presence of two distinct isocyanide vibrational modes at 2155 and 2121 cm^{-1} (Fig. 6.5A, and Table 6.1). Based on the above, they are assigned to free (2121 cm^{-1}) and bound isocyanide modes (2155 cm^{-1}). However, in the case of PDI-derived oligomers, the isocyanide modes that initially form at an ICPD exposure of ∼0.8 L are at lower frequencies than that found at higher exposures. The most prominent difference is the fact that the formation of the free isocyanide mode precedes the formation of the bound isocyanide (Fig. 6.5), completely different to the case for oligomers formed from PDI. In the latter case, the isocyanides in the initially formed oligomers eventually de-coordinate as the PDI exposure increases, and enables other adsorbates such as CO to occupy the resulting sites. [51]

In order to correlate the species formed on the surface with the desorption states found in TPD(Fig. 6.2), a saturated overlayer of ICPD formed at 300 K, was heated (at a rate of 5K/min) while recording the infrared spectra (Fig. 6.6). The isocyanide stretching modes decrease in intensity as a function of temperature to eventually disappear completely after heating to ∼450 K. The resulting variation in the intensity of the free and bound isocyanide modes is shown in (Fig. 6.7B), where the free isocyanide

mode decreases at high annealing temperatures, suggesting that it is associated with desorption in the high-temperature (467 K) state in TPD (Fig. 6.2), while the bound isocyanide is associated with the low-temperature (∼400 K) state. This is further illustrated in (Fig. 6.7C), which uses the desorption parameters from the TPD data (Fig. 6.2) to calculate the variation in intensity of the free and bound isocyanide modes as a function of temperature at a heating rate of 5 K/min, used to collect the infrared data in (Fig. 6.6). This reveals that the variation in the desorption yeilds of free isocyanide closely mimics the variation in coverage of this species measured by infrared spectroscopy, while there are differences between the bound isocyanide coverages from TPD and infrared. Finally, the removal of the free and bound isocyanide modes as a function of temperature (Fig. 6.7B) mirror the variation in the coverages of these species during adsorption (Fig. 6.5B), implying that the desorption kinetics are the reverse of the kinetic processes occurring during adsorption.

These results, taken together, indicate that the formation of thiolate species from the dissociation of disulfide linkages differs from those formed from deprotonation of -SH groups. Based on the oligomerization chemistry of BDT described above, each thiolate species appears to be coordinated to a gold adatom that allows the gold-containing oligomers to form. This appears not to occur for disulfide linkers suggesting that both thiolate species bind to the same gold adatom. [37, 38, 40] In this case, one of the resulting thiolate species would be available to form gold containing oligomers with an isocyanide stretching frequency at 2155 cm^{-1}, while the other ICPD moiety will remain uncoordinated and have a free isocyanide vibrational frequency at 2121^{-1}. This model is broadly in accord with the ICPD adsorption kinetics (Fig. 6.4,6.5) where ICPD initially adsorbs to exhibit mainly free isocyanides for exposures up to ∼0.7 L, with the formation of a small portion of bound isocyanides (Fig. 6.5B). There is no evidence of the isocyanide group initially binding to a gold adatom, as this would give rise to a

vibrational mode at ∼2180 cm^{-1}, which is not observed.

The data in Fig. 6.8 provide some information that this occurs when there is an ordering of the system on heating to above ∼210 K (Fig. 6.9) and the concomitant appearance of a peak at ∼2155 cm^{-1} (Fig. 6.8) indicative of oligomer formation. In addition, the isocyanide stretching frequency for the ICPD-derived oligomer at saturation coverage occurs at ∼2155 cm^{-1}, while the isocyanide frequency of PDI-derived oligomers is at a lower frequency (2137 cm^{-1}). This implies that the isocyanide is not a -N≡C-Au-C≡N- fragment and is thus assigned to a -S-Au-C≡N- vibration, as expected from a -SC_6H_4-NC propagating species.

However, the simple model descrived above would suggest that the variation in coverage of Au-SC_6H_4-NC adatom species and the fragment in the oligomer should appear in equimolar ratios, while clearly, they do not. This implies that both of the -SC_6H_4-NC moieties of the dissociated ICPD bound to a gold adatom can form oligomeric linkages. The desorption behavior approximately mirrors the adsorption kinetics (Fig. 6.3) where, comparing Figs. (6.7A, 6.7B), the 467 K feature derives primarily from the formation of ICPD from Au-SC_6H_4-NC adatom species and is formed with an activation energy of ∼99 kJ/mol (Fig. 6.7B). The lower-temperature state appears to be fromed from the molecular fragments both in the oligomer and from the adatom species.

6.5 Conclusion

The adsorption of an asymmetric molecule comprising moieties with an aryl ring with para isocyanide and sulfide groups, (4-isocyanophenyl disulfide), is studied on a Au(111) surface to explore whether it can from the basis for molecular electronic devices through a self-assembly process found previously for symmetric molecules, PDI and BDT. Evidence is presented to suggest that ICPD adsorbs by S-S bond scission where both

sulfurs bind to the same adatom. While there is no direct evidence that oligomeric species are formed from ICPD on Au(111), adsorption at room temperatures yield surface species with an isocyanide stretching frequency that is consistent with the formation of an oligomeric species. The infrared spectrum also contains a species with free, pendent isocyanide groups characteristic of a Au-S-C_6H_4-NC adatom species due to the dissociative adsorption of ICPD on a single gold adatom site. The surface science results suggest that ICPD is likely to self-assemble to form aligned gold-containing oligomers. The adsorbed species are quite stable and thermally desorb above $\sim$370 K via a second-order reaction to reform ICPD. This structure still needs to be confirmed by direct imaging and the conductivity of the putative self-assembled oligomers to be measured. However, the relatively large calculated dipole moment of the -S-C_6H_4-NC moiety (of 1.5 Debye) suggest that it might be possible to align the oligomer in an external electric field. [51]

Bibliography

[1] Arieh Aviram and Mark A Ratner. Molecular rectifiers. *Chemical physics letters*, 29(2):277–283, 1974.

[2] Mikio Ito, Hidenori Noguchi, Katsuyoshi Ikeda, and Kohei Uosaki. Substrate dependent structure of adsorbed aryl isocyanides studied by sum frequency generation (sfg) spectroscopy. *Physical Chemistry Chemical Physics*, 12(13):3156–3163, 2010.

[3] BongSoo Kim, Jeremy M Beebe, Yongseok Jun, X-Y Zhu, and C Daniel Frisbie. Correlation between homo alignment and contact resistance in molecular junctions: aromatic thiols versus aromatic isocyanides. *Journal of the American Chemical Society*, 128(15):4970–4971, 2006.

[4] Yan Li, Deyu Lu, Sally A Swanson, J Campbell Scott, and Giulia Galli. Microscopic characterization of the interface between aromatic isocyanides and au (111): A first-principles investigation. *The Journal of Physical Chemistry C*, 112(16):6413–6421, 2008.

[5] Kristen L Murphy, Wilfred T Tysoe, and Dennis W Bennett. A comparative investigation of aryl isocyanides chemisorbed to palladium and gold: An atr-ir spectroscopic study. *Langmuir*, 20(5):1732–1738, 2004.

[6] Mitchell J Robertson and Robert J Angelici. Adsorption of aryl and alkyl isocyanides on powdered gold. *Langmuir*, 10(5):1488–1492, 1994.

[7] Kuo-Chen Shih and Robert J Angelici. Equilibrium and saturation coverage studies of alkyl and aryl isocyanides on powdered gold. *Langmuir*, 11(7):2539–2546, 1995.

[8] Jason I Henderson, Sue Feng, Gregory M Ferrence, Thomas Bein, and Clifford P Kubiak. Self-assembled monolayers of dithiols, diisocyanides, and isocyanothiols on gold:'chemically sticky'surfaces for covalent attachment of metal clusters and studies of interfacial electron transfer. *Inorganica chimica acta*, 242(1-2):115–124, 1996.

[9] Mark A Reed, C Zhou, CJ Muller, TP Burgin, and JM Tour. Conductance of a molecular junction. *Science*, 278(5336):252–254, 1997.

[10] SN Yaliraki, M Kemp, and Mark A Ratner. Conductance of molecular wires: Influence of molecule- electrode binding. *Journal of the American Chemical Society*, 121(14):3428–3434, 1999.

[11] XD Cui, A Primak, X Zarate, J Tomfohr, OF Sankey, Ana L Moore, Thomas A Moore, D Gust, Gari Harris, and SM Lindsay. Reproducible measurement of single-molecule conductivity. *science*, 294(5542):571–574, 2001.

[12] Yongqiang Xue and Mark A Ratner. Microscopic study of electrical transport through individual molecules with metallic contacts. i. band lineup, voltage drop, and high-field transport. *Physical Review B*, 68(11):115406, 2003.

[13] Xiaoyin Xiao, Bingqian Xu, and Nongjian J Tao. Measurement of single molecule conductance: Benzenedithiol and benzenedimethanethiol. *Nano Letters*, 4(2):267–271, 2004.

[14] Manabu Kiguchi, Shinichi Miura, Kenji Hara, Masaya Sawamura, and Kei Murakoshi. Conductance of a single molecule anchored by an isocyanide substituent to gold electrodes. *Applied physics letters*, 89(21):213104, 2006.

[15] Renato B Pontes, Frederico D Novaes, Adalberto Fazzio, and Antonio JR da Silva. Adsorption of benzene-1, 4-dithiol on the au (111) surface and its possible role in molecular conductance. *Journal of the American Chemical Society*, 128(28):8996–8997, 2006.

[16] Makusu Tsutsui, Yumi Teramae, Shu Kurokawa, and Akira Sakai. High-conductance states of single benzenedithiol molecules. *Applied physics letters*, 89(16):163111, 2006.

[17] A Arnold, F Weigend, and F Evers. Quantum chemistry calculations for molecules coupled to reservoirs: formalism, implementation, and application to benzenedithiol. *The Journal of chemical physics*, 126(17):174101, 2007.

[18] Sina Yeganeh, Mark A Ratner, Michael Galperin, and Abraham Nitzan. Transport in state space: Voltage-dependent conductance calculations of benzene-1, 4-dithiol. *Nano letters*, 9(5):1770–1774, 2009.

[19] K Horiguchi, M Tsutsui, S Kurokawa, and A Sakai. Electron transmission characteristics of au/1, 4-benzenedithiol/au junctions. *Nanotechnology*, 20(2):025204, 2008.

[20] Artem Mishchenko, David Vonlanthen, Velimir Meded, Marius Burkle, Chen Li, Ilya V Pobelov, Alexei Bagrets, Janne K Viljas, Fabian Pauly, Ferdinand Evers, et al. Influence of conformation on conductance of biphenyl-dithiol single-molecule contacts. *Nano letters*, 10(1):156–163, 2009.

[21] Youngsang Kim, Torsten Pietsch, Artur Erbe, Wolfgang Belzig, and Elke Scheer. Benzenedithiol: a broad-range single-channel molecular conductor. *Nano letters*, 11(9):3734–3738, 2011.

[22] Renato Borges Pontes, Alexandre Reily Rocha, Stefano Sanvito, Adalberto Fazzio, and Antonio Jose Roque da Silva. Ab initio calculations of structural evolution and conductance of benzene-1, 4-dithiol on gold leads. *ACS nano*, 5(2):795–804, 2011.

[23] Jorge Boscoboinik, John Kestell, Michael Garvey, Michael Weinert, and Wilfred T Tysoe. Creation of low-coordination gold sites on au (111) surface by 1, 4-phenylene diisocyanide adsorption. *Topics in Catalysis*, 54(1-4):20–25, 2011.

[24] Jorge A Boscoboinik, Florencia C Calaza, Zeesham Habeeb, Dennis W Bennett, Dario J Stacchiola, Martin A Purino, and Wilfred T Tysoe. One-dimensional supramolecular surface structures: 1, 4-diisocyanobenzene on au (111) surfaces. *Physical Chemistry Chemical Physics*, 12(37):11624–11629, 2010.

[25] J Zhou, D Acharya, N Camillone III, P Sutter, and MG White. Adsorption structures and electronic properties of 1, 4-phenylene diisocyanide on the au (111) surface. *The Journal of Physical Chemistry C*, 115(43):21151–21160, 2011.

[26] John Kestell, Rasha Abuflaha, J Anibal Boscoboinik, Yun Bai, Dennis W Bennett, and Wilfred T Tysoe. Linking gold nanoparticles with conductive 1, 4-phenylene diisocyanide–gold oligomers. *Chemical Communications*, 49(14):1422–1424, 2013.

[27] John Kestell, Rasha Abuflaha, J Anibal Boscoboinik, Michael Garvey, Dennis W Bennett, and Wilfred T Tysoe. Determination of adsorbate structures from 1, 4-phenylene diisocyanide on gold. *The journal of physical chemistry letters*, 5(20):3577–3581, 2014.

[28] Michael Garvey, John Kestell, Rasha Abuflaha, Dennis W Bennett, Graeme Henkelman, and Wilfred T Tysoe. Understanding and controlling the 1, 4-phenylene diisocyanide–gold oligomer formation pathways. *The Journal of Physical Chemistry C*, 118(36):20899–20907, 2014.

[29] Rasha Abuflaha, Dustin Olson, Dennis W Bennett, and Wilfred T Tysoe. Surface chemistry and structures of 1, 4-phenylene diisocyanide on gold films from solution. *Surface Science*, 649:56–59, 2016.

[30] Ronald P Andres, Jeffery D Bielefeld, Jason I Henderson, David B Janes, Venkat R Kolagunta, Clifford P Kubiak, William J Mahoney, and Richard G Osifchin. Self-assembly of a two-dimensional superlattice of molecularly linked metal clusters. *Science*, 273(5282):1690–1693, 1996.

[31] N Fishelson, I Shkrob, O Lev, J Gun, and AD Modestov. Studies on charge transport in self-assembled gold- dithiol films: conductivity, photoconductivity, and photoelectrochemical measurements. *Langmuir*, 17(2):403–412, 2001.

[32] Jianhui Liao, Markus A Mangold, Sergio Grunder, Marcel Mayor, Christian Schonenberger, and Michel Calame. Interlinking au nanoparticles in 2d arrays via conjugated dithiolated molecules. *New Journal of Physics*, 10(6):065019, 2008.

[33] David Vonlanthen, Artem Mishchenko, Mark Elbing, Markus Neuburger, Thomas Wandlowski, and Marcel Mayor. Chemically controlled conductivity: Torsion-angle dependence in a single-molecule biphenyldithiol junction. *Angew. Chem., Int. Ed*, 48(47):8886–8890, 2009.

[34] Li-Li Lin, Chuan-Kui Wang, and Yi Luo. Inelastic electron tunneling spectroscopy of gold- benzenedithiol- gold junctions: Accurate determination of molecular conformation. *ACS nano*, 5(3):2257–2263, 2011.

[35] Ryuji Matsuhita, Masyo Horikawa, Yasuhisa Naitoh, Hisao Nakamura, and Manabu Kiguchi. Conductance and sers measurement of benzenedithiol molecules bridging between au electrodes. *The Journal of Physical Chemistry C*, 117(4):1791–1795, 2013.

[36] John Kestell, Rasha Abuflaha, Michael Garvey, and Wilfred T Tysoe. Self-assembled oligomeric structures from 1, 4-benzenedithiol on au (111) and the formation of conductive linkers between gold nanoparticles. *The Journal of Physical Chemistry C*, 119(40):23042–23051, 2015.

[37] Peter Maksymovych, Dan C Sorescu, and John T Yates Jr. Gold-adatom-mediated bonding in self-assembled short-chain alkanethiolate species on the au (111) surface. *Physical Review Letters*, 97(14):146103, 2006.

[38] Peter Maksymovych and John T Yates Jr. Au adatoms in self-assembly of benzenethiol on the au (111) surface. *Journal of the American Chemical Society*, 130(24):7518–7519, 2008.

[39] Oleksandr Voznyy, Jan J Dubowski, John T Yates Jr, and Peter Maksymovych. The role of gold adatoms and stereochemistry in self-assembly of methylthiolate on au (111). *Journal of the American Chemical Society*, 131(36):12989–12993, 2009.

[40] Peter Maksymovych, Oleksandr Voznyy, Daniel B Dougherty, Dan C Sorescu, and John T Yates Jr. Gold adatom as a key structural component in self-assembled monolayers of organosulfur molecules on au (1 1 1). *Progress in Surface Science*, 85(5-8):206–240, 2010.

[41] Gregory M Ferrence, Jason I Henderson, Dirk G Kurth, David A Morgenstern, Thomas Bein, and Clifford P Kubiak. Covalent attachment of nickel clusters

to gold electrode surfaces. formation of rectifying molecular layers. *Langmuir*, 12(12):3075–3081, 1996.

[42] M Kaltchev, AW Thompson, and WT Tysoe. Reflection-absorption infrared spectroscopy of ethylene on palladium (111) at high pressure. *Surface science*, 391(1-3):145–149, 1997.

[43] Hans A Biebuyck and George M Whitesides. Interchange between monolayers on gold formed from unsymmetrical disulfides and solutions of thiols: evidence for sulfur-sulfur bond cleavage by gold metal. *Langmuir*, 9(7):1766–1770, 1993.

[44] Naoki Nishida, Masahiko Hara, Hiroyuki Sasabe, and Wolfgang Knoll. Thermal desorption spectroscopy of alkanethiol self-assembled monolayer on au (111). *Japanese journal of applied physics*, 35(11R):5866, 1996.

[45] PA Redhead. Thermal desorption of gases. *vacuum*, 12(4):203–211, 1962.

[46] Sally A Swanson, Richard McClain, Katherine S Lovejoy, Neda B Alamdari, Jeremy S Hamilton, and J Campbell Scott. Self-assembled diisocyanide monolayer films on gold and palladium. *Langmuir*, 21(11):5034–5039, 2005.

[47] Robert G Greenler. Infrared study of adsorbed molecules on metal surfaces by reflection techniques. *The Journal of Chemical Physics*, 44(1):310–315, 1966.

[48] M. J. Frisch, G. W. Trucks, H. B. Schlegel, G. E. Scuseria, M. A. Robb, J. R. Cheeseman, G. Scalmani, V. Barone, B. Mennucci, G. A. Petersson, H. Nakatsuji, M. Caricato, X. Li, H. P. Hratchian, A. F. Izmaylov, J. Bloino, G. Zheng, J. L. Sonnenberg, M. Hada, M. Ehara, K. Toyota, R. Fukuda, J. Hasegawa, M. Ishida, T. Nakajima, Y. Honda, O. Kitao, H. Nakai, T. Vreven, J. A. Montgomery, Jr., J. E. Peralta, F. Ogliaro, M. Bearpark, J. J. Heyd, E. Brothers, K. N. Kudin, V. N. Staroverov,

R. Kobayashi, J. Normand, K. Raghavachari, A. Rendell, J. C. Burant, S. S. Iyengar, J. Tomasi, M. Cossi, N. Rega, J. M. Millam, M. Klene, J. E. Knox, J. B. Cross, V. Bakken, C. Adamo, J. Jaramillo, R. Gomperts, R. E. Stratmann, O. Yazyev, A. J. Austin, R. Cammi, C. Pomelli, J. W. Ochterski, R. L. Martin, K. Morokuma, V. G. Zakrzewski, G. A. Voth, P. Salvador, J. J. Dannenberg, S. Dapprich, A. D. Daniels, O. Farkas, J. B. Foresman, J. V. Ortiz, J. Cioslowski, and D. J. Fox. Gaussian 09 Revision E.01. Gaussian Inc. Wallingford CT 2009.

[49] M Jaschke, H Schönherr, H Wolf, H-J Butt, E Bamberg, MK Besocke, and H Ringsdorf. Structure of alkyl and perfluoroalkyl disulfide and azobenzenethiol monolayers on gold (111) revealed by atomic force microscopy. *The Journal of physical chemistry*, 100(6):2290–2301, 1996.

[50] Tomohiro Hayashi, Yoshitada Morikawa, and Hisakazu Nozoye. Adsorption state of dimethyl disulfide on au (111): Evidence for adsorption as thiolate at the bridge site. *The Journal of Chemical Physics*, 114(17):7615–7621, 2001.

[51] John Kestell, J Anibal Boscoboinik, Lanxia Cheng, Michael Garvey, Dennis W Bennett, and Wilfred T Tysoe. Structural changes in self-catalyzed adsorption of carbon monoxide on 1, 4-phenylene diisocyanide modified au (111). *The Journal of Physical Chemistry C*, 119(32):18317–18325, 2015.

Chapter 7

Surface Structure of 1,4-Benzenedithiol on Au(111)

7.1 Introduction

The electron transport properties of the prototypical molecular electronic component 1,4-benzene dithiol (1,4-BDT), have been extensively studied though the use of STM, and mechanical break-junction experiments [1–5]. The interest in di-thiols as molecular electronic components is largely due to their formation of strong thiolate bonds with gold and other metals [6–8]. The exact binding geometry of thiols, and disulfides on gold has been largely under discussion for many years, but it was found that similarly to the structures observed for PDI, the thiolate binds to gold though an adatom [9–11].

The formation of oligomeric chains analogous to those formed by PDI by the incorporation of gold adatoms upon exposure of 1,4-BDT to Au(111) has been previously observed, resulting in predominately zigzag chains, where it is postulated that their formation is due to a *trans* configured oligomer chain consisting of -(Au-1,4-BDT)- oligomer units [12]. In the following, we the test the previously postulated geometries for 1,4-BDT oligomers by a combination of scanning tunneling microscopy, and density functional theory (DFT) calculations.

7.2 Experimental Methods

Scanning tunneling microscopy measurements were made in a ultrahigh vacuum (UHV) chamber operating at base pressure of $\sim 2 \times 10^{-10}$ Torr after bakeout. STM experiments were carried out using an RHK UHV 350 dual AFM/STM, as described elsewhere, [13] along with the methods used to prepare the tungsten tip. 1,4-BDT was dosed via a knudsen source with a directional dosing tube that is ~0.25" in diameter directed toward the sample to minimize background contamination. The vial containing 1,4-BDT could be cooled by submersion in a cryogenic bath, generally consisting of ice water bath to control the vapor pressure and thus the exposure.

The Au(111) single crystal (Princeton Scientific) was cleaned with cycles of ion bombardment using 1 keV argon ions for 30 min (1 μA/cm2), annealing to 900 K for 5 min and then to 600 K for 30 min. The sample could be cooled to ~95 K in the infrared chamber and to ~120 K in the STM chambers by thermal contact to a liquid-nitrogen-filled reservoir, and resistively heated to ~1200 K.

Density functional theory (DFT) calculations were performed with the projector augmented wave (PAW) method [14, 15] as implemented in the Vienna ab initio simulationpackage, VASP. [16, 17] The exchange-correlation potential was described using the generalized gradient approximation (GGA) of Perdew, Burke, and Ernzerhof. [18] A cutoff of 400 eV was used for the planewave basis set, and the wave functions and electron density were converged to within 1×10^{-5} eV. The first Brillouin zone was sampled with a $4 \times 4 \times 1$ Γ-centered k-point mesh. Geometric relaxations were considered to be converged when the force was less than 0.02 eV/Å on all unrestricted atoms. STM simulations were performed by using the Tersoff-Hamann method [19] for comparison to experiment.

7.3 Results and Discussion

The resulting STM images acquired for high, and low coverages of 1,4-BDT dosed on Au(111) at 300 K are shown in Figure 7.1. Figure 7.1A shows an image of a high coverage film of 1,4-BDT, displaying close packed domains constructed largely of zigzag chains of 1,4-BDT, where bends in the chains result in directional changes of the chains of 120 degrees. It was previously postulated that the origin of the oligomer structure is due to the sp^3 bonding of sulfur, causing the thiolate structure to adopt *trans* and *cis* configurations when bound to a gold adatom [12], where the *trans* motif is responsible for the linear oligomer chains and dominates the observed oligomer structures. Shown in Figure 7.1B, is a STM image of a low coverage of 1,4-BDT, where the BDT sample was cooled via an ice bath to lower the vapor pressure and thus the dose, the observed large domains appear to grow preferentially from the step edge in the lower right corner of the image, consistent with the suggestion that gold adatoms are extracted from low coordination sites. Similar to the oligomerization mechanism proposed for phenylene disocyanide (PDI) [20], it was found that 1,4-BDT initially adsorbs in a similar manner via an mobile upright η^1 adatom complex [12] that can then diffuse until inserting into an growing oligomer chain. The initially adsorbed mobile adatom complex is consitent with the preference to grow domains, and the lack of single monomer species in the low coverage STM image. Figure 7.1C, shows an additional image of a low coverage of 1,4-BDT on Au(111) where here the herringbone reconstruction [21] of the substrate is still visible, and the oligomer chains appear to grow preferentially between the solitons of the reconstruction.

The results of DFT calculations are shown in Figure 7.2 for the relaxed *trans* structure of the 1,4-BDT oligomer chains, where Figure 7.2A provides a top view of the oligomer structure, Figure 7.2B shows an angled view, and Figure 7.2C shows a side

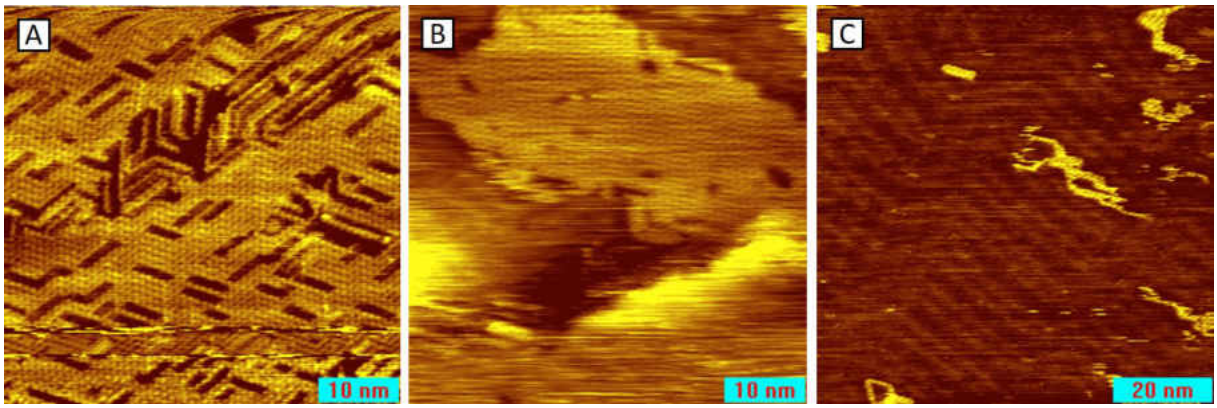

FIGURE 7.1: STM images of 1,4-BDT on Au(111) adsorbed at 300K. (A) High coverage film showing close-packed features consisting of chains of oligomers rotating by 120^o(I_t=0.254 nA, V_t=-0.64 V). (B) Low coverage film showing close packed domain of BDT growing from a step edge, surrounded by a clean terrace((I_t=0.143 nA, V_t=-0.75 V). (C) Low coverage film of BDT, herring bone reconstruction is clearly present with isolated oligomer patches growing preferentially between reconstruction(I_t=0.65 nA, V_t=-0.394 V).

view. The optimized geometry for the DFT calculations was found by first running single point calculations and by varying the separation between the linear chains, from there for the minimum energy structure, one chain was laterally offset with respect to the other, and the resulting lowest energy structure is shown. Provided in Figure 7.3A are the distances between sulfurs within a chain, as well as the the S-S distance to the neighboring chain allowing for comparison to the distances measured experimentally. Shown in Figure 7.3B are ladder-like features formed by two neighboring oligomer chains comprised of only *trans* oligomeric units. The corresponding experimental distances are found to be 0.982 nm (neighboring chain, Fig. 7.3C), and 0.934 nm (in chain, Fig. 7.3D) for the ladder-like oligomer formation, both in good agreement with the DFT calculated structure. In accord with the previous predictions based on RAIR spectra of 1,4-BDT on Au(111) [12], we find that for the *trans* oligomer configuration the aryl ring lies parallel to the surface

In order to confirm the incorporation of gold adatoms in the self-assembled oligomer

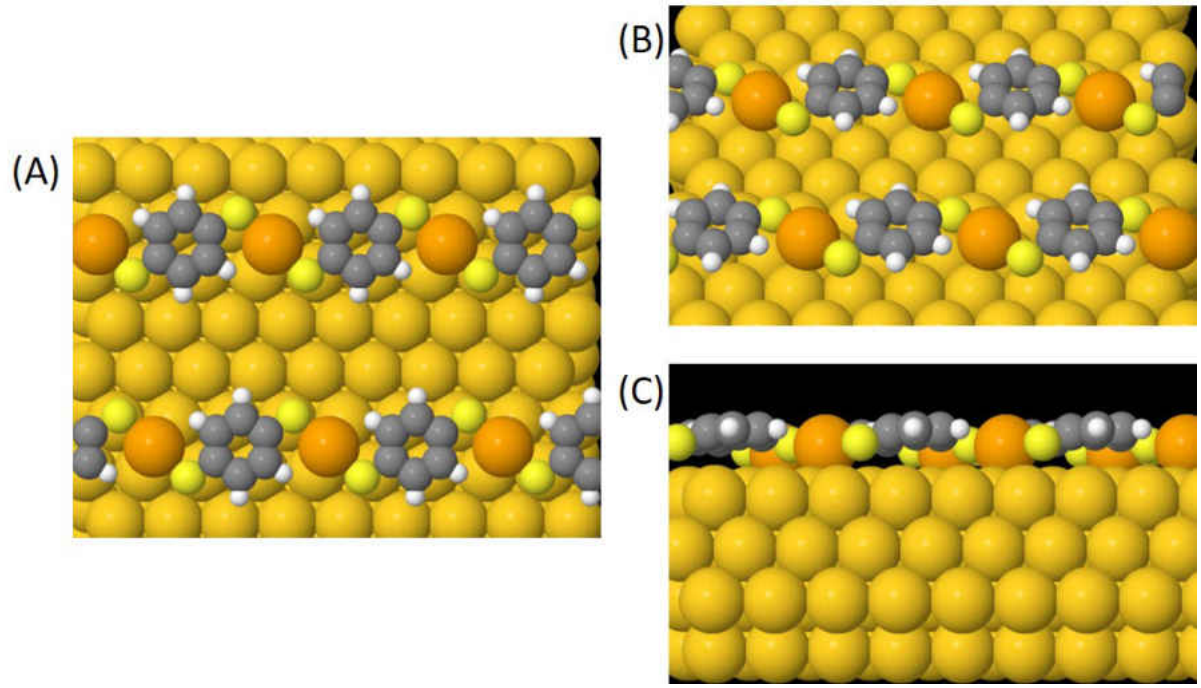

FIGURE 7.2: Structure of -(Au-BDT)- oligomers on gold calculated using density functional theory showing (A) a top view, (B) an angled view, and (C) a side view of the oligomer chains, where gold adatoms are highlighted in orange.

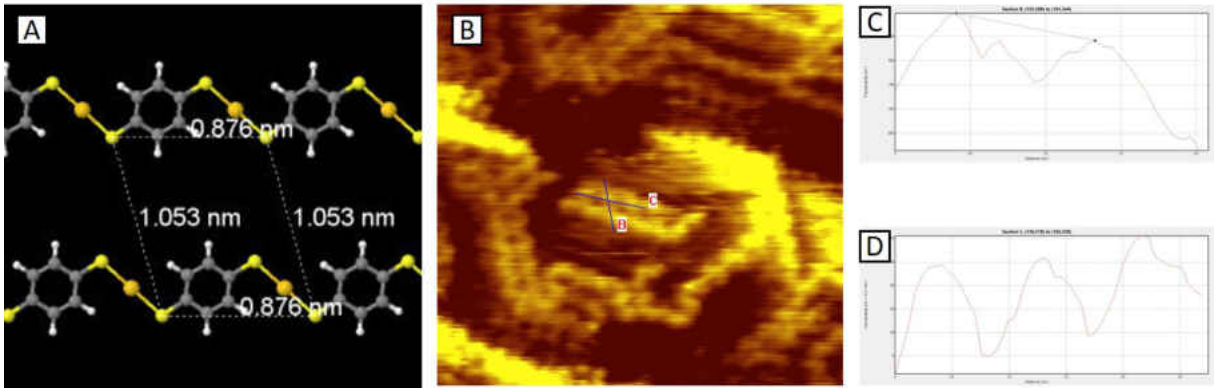

FIGURE 7.3: A) Structure of -(Au-BDT)- oligomers on gold with the surface removed for clarity, optimized structure has the S-S distance within the chain as 0.876 nm, and the S-S distance between chains as 1.053 nm. B) Experimentally observed ladder feature(I_t=0.33 nA, V_t=-0.63 V), and corresponding line scans (C,D) indicating the S-S distance within the chain as 0.982 nm, and between chains as 0.934 nm.

chains observed by STM for 1,4-BDT, STM simuations were done using the relaxed structures shown in Figure 7.2 using the Tersoff-Hamann method. The results of the

simulation are shown in Figure 7.4B, where the simulated image is overlapped with the oligomer structure to clarify the origin of the STM simulation, where the surface is also removed for clarity. For comparison, a magnified STM image showing features consistent with the STM simulation is provided in Figure 7.4A, suggesting that the ladder like features seen in STM originate from two parallel BDT oligomer chains consisting of -(Au-BDT)- units.

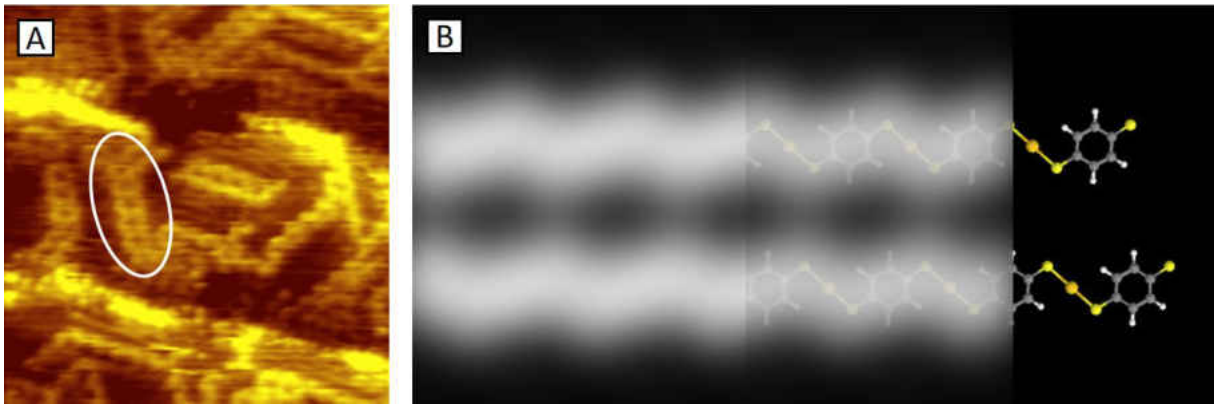

FIGURE 7.4: A)Magnification of STM image shown in Fig. **??**B highlighting ladder feature in circle, B) Result of simulated STM of ladder feature consisting of two BDT oligomers using Tersoff-Hamann method (blurred with 25 point smoothing to account for tip radius) overlapped with oligomer structure for clarity.

In order to investigate the effect of film annealing, a common techique used to acheive well ordered self-assembled monolayers (SAMs) [22], a high coverage film of 1,4-BDT was heated to 400 K and held at that temperature for 60 min, and the resulting STM images are provided in Figure 7.5A,B. The resulting layers are nearly defect free, as opposed to un-annealed high coverage films that have vacant patches (Fig 7.1A). In Figure 7.5A, the zigzag features can no longer be discerned, suggesting the entire domain of oligomer chains has adapted the same geometry.

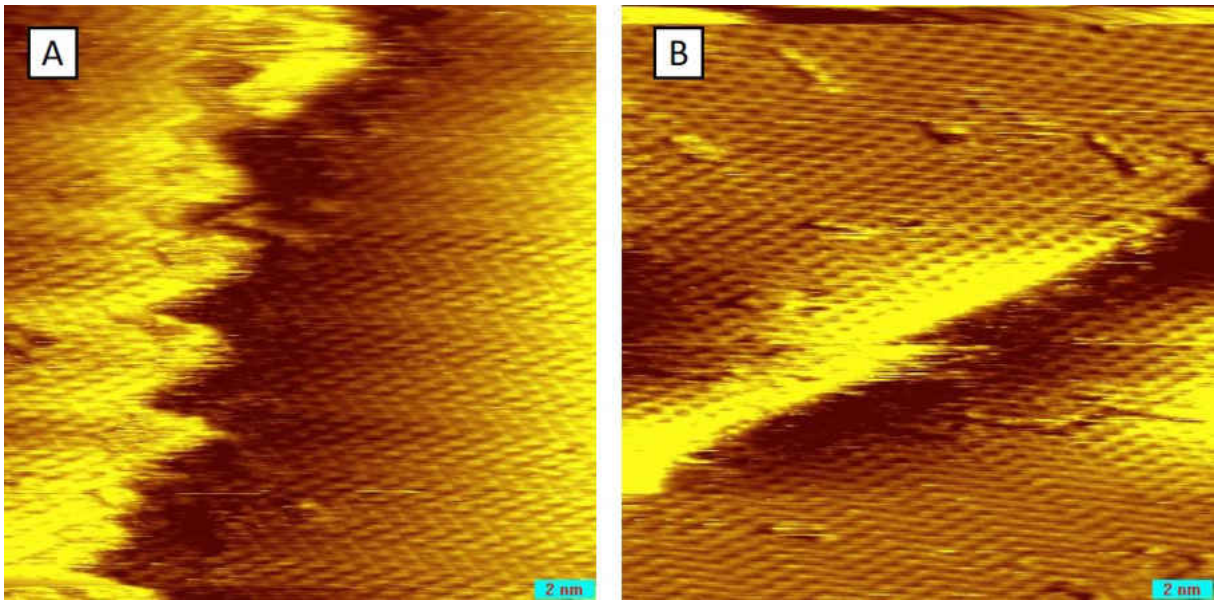

FIGURE 7.5: STM images of a high coverage film of 1,4-BDT on Au(111) annealed to 400 K after adsorption, (A,B) Well ordered monolayer of 1,4-BDT formed after annealing for 1 hr, imaged at 300 K (I_t=0.22 nA, V_t=0.60 V).

7.4 Conclusion

STM images were collected for low, and high coverages of 1,4-BDT adsorbed on Au(111) at 300 K, and the resulting oligomeric structure modeled by DFT calculations. At low coverage, we observe isolated domains growing from a step edge (7.1B) surrounded by clean Au(111) regions, consistent with a mobile adatom complex as the initiator to oligomerization. Contrary to the oligomers observered for PDI on Au(111) which demonstrate a interchain repulsive interaction [23], 1,4-BDT has the preference to grow as close packed domains as observed by STM. This is corroborated computationally by the stability gained for the optimized structure with a chain separation of 1.053 nm, as opposed to chains calculated with larger or smaller separation. The simulated STM images, along with the dimensions of the optimized oligomer chains in DFT agree very well with both previously postulated adsorption geometries [12], and the STM images

included here, confirming that the observed 1,4-BDT oligomers are comprised of -(Au-BDT)- units analogous to those found for PDI.

Bibliography

[1] Xiaoyin Xiao, Bingqian Xu, and Nongjian J Tao. Measurement of single molecule conductance: Benzenedithiol and benzenedimethanethiol. *Nano Letters*, 4(2):267–271, 2004.

[2] Li-Li Lin, Chuan-Kui Wang, and Yi Luo. Inelastic electron tunneling spectroscopy of gold- benzenedithiol- gold junctions: Accurate determination of molecular conformation. *ACS nano*, 5(3):2257–2263, 2011.

[3] Renato Borges Pontes, Alexandre Reily Rocha, Stefano Sanvito, Adalberto Fazzio, and Antonio Jose Roque da Silva. Ab initio calculations of structural evolution and conductance of benzene-1, 4-dithiol on gold leads. *ACS nano*, 5(2):795–804, 2011.

[4] Subhasis Ghosh, Henny Halimun, Ajit Kumar Mahapatro, Jaewon Choi, Saurabh Lodha, and David Janes. Device structure for electronic transport through individual molecules using nanoelectrodes. *Applied Physics Letters*, 87(23):233509, 2005.

[5] Manabu Kiguchi, Shinichi Miura, Kenji Hara, Masaya Sawamura, and Kei Murakoshi. Conductance of single 1, 4-disubstituted benzene molecules anchored to pt electrodes. *Applied Physics Letters*, 91(5):053110, 2007.

[6] Jingdong Zhang, Qijin Chi, and Jens Ulstrup. Assembly dynamics and detailed structure of 1-propanethiol monolayers on au (111) surfaces observed real time by in situ stm. *Langmuir*, 22(14):6203–6213, 2006.

[7] Paul E Laibinis, George M Whitesides, David L Allara, Yu Tai Tao, Atul N Parikh, and Ralph G Nuzzo. Comparison of the structures and wetting properties of self-assembled monolayers of n-alkanethiols on the coinage metal surfaces, copper, silver, and gold. *Journal of the American Chemical Society*, 113(19):7152–7167, 1991.

[8] J Christopher Love, Lara A Estroff, Jennah K Kriebel, Ralph G Nuzzo, and George M Whitesides. Self-assembled monolayers of thiolates on metals as a form of nanotechnology. *Chemical reviews*, 105(4):1103–1170, 2005.

[9] Peter Maksymovych, Dan C Sorescu, and John T Yates Jr. Gold-adatom-mediated bonding in self-assembled short-chain alkanethiolate species on the au (111) surface. *Physical Review Letters*, 97(14):146103, 2006.

[10] Natalie A Kautz and S Alex Kandel. Alkanethiol/au (111) self-assembled monolayers contain gold adatoms: Scanning tunneling microscopy before and after reaction with atomic hydrogen. *Journal of the American Chemical Society*, 130(22):6908–6909, 2008.

[11] Peter Maksymovych and John T Yates Jr. Au adatoms in self-assembly of benzenethiol on the au (111) surface. *Journal of the American Chemical Society*, 130(24):7518–7519, 2008.

[12] John Kestell, Rasha Abuflaha, Michael Garvey, and Wilfred T Tysoe. Self-assembled oligomeric structures from 1, 4-benzenedithiol on au (111) and the formation of conductive linkers between gold nanoparticles. *The Journal of Physical Chemistry C*, 119(40):23042–23051, 2015.

[13] Jorge A Boscoboinik, Florencia C Calaza, Zeesham Habeeb, Dennis W Bennett, Dario J Stacchiola, Martin A Purino, and Wilfred T Tysoe. One-dimensional supramolecular surface structures: 1, 4-diisocyanobenzene on au (111) surfaces. *Physical Chemistry Chemical Physics*, 12(37):11624–11629, 2010.

[14] Georg Kresse and Daniel Joubert. From ultrasoft pseudopotentials to the projector augmented-wave method. *Physical review b*, 59(3):1758, 1999.

[15] Peter E Blochl. Projector augmented-wave method. *Physical review B*, 50(24):17953, 1994.

[16] Georg Kresse and Jurgen Furthmuller. Efficient iterative schemes for ab initio total-energy calculations using a plane-wave basis set. *Physical review B*, 54(16):11169, 1996.

[17] Georg Kresse and Jurgen Furthmuller. Efficiency of ab-initio total energy calculations for metals and semiconductors using a plane-wave basis set. *Computational materials science*, 6(1):15–50, 1996.

[18] John P Perdew, Kieron Burke, and Matthias Ernzerhof. Generalized gradient approximation made simple. *Physical review letters*, 77(18):3865, 1996.

[19] Jerry Tersoff and Donald R Hamann. Theory of the scanning tunneling microscope. *Physical Review B*, 31(2):805, 1985.

[20] John Kestell, Rasha Abuflaha, J Anibal Boscoboinik, Michael Garvey, Dennis W Bennett, and Wilfred T Tysoe. Determination of adsorbate structures from 1, 4-phenylene diisocyanide on gold. *The journal of physical chemistry letters*, 5(20):3577–3581, 2014.

[21] JV Barth, Harald Brune, G Ertl, and RJ Behm. Scanning tunneling microscopy observations on the reconstructed au (111) surface: Atomic structure, long-range superstructure, rotational domains, and surface defects. *Physical Review B*, 42(15):9307, 1990.

[22] C Vericat, ME Vela, G Benitez, P Carro, and RC Salvarezza. Self-assembled monolayers of thiols and dithiols on gold: new challenges for a well-known system. *Chemical Society Reviews*, 39(5):1805–1834, 2010.

[23] Min Feng, Hao Sun, Jin Zhao, and Hrvoje Petek. Self-catalyzed carbon dioxide adsorption by metal–organic chains on gold surfaces. *ACS nano*, 8(8):8644–8652, 2014.

Appendix A

Temperature Programmed Desorption Simulator

```
/*
 * File:   TPD.cpp
 * Author: Dustin Olson
 *
 * Created on August 2, 2019, 11:03 AM
 */

#include <iostream>
#include <cmath>
#include <iomanip>
#include <cstdlib>

using namespace std;
```

```
double Eact1 = 80000; // J/mol
double Eact2 = 101000; // J/mol
double n1 = 1;
double n2 = 2;
double Theta01 = 50000000000000;
double Theta02 = 50000000000000;


const double A = 1000000000000000; // s-1
const double A2 = 100000000000000;
const double T0 = 220; //Kelvin
const double Beta = 2.0; //k s-1
const double dt = .01; // s
const double R = 8.32;
double dT = Beta*dt;

double TimeScale[20000];
double TempScale[20000];
double Theta1[2][20000];
double Rate[10][20000];
double Rate2[10][20000];
double Total[10][20000];
double dTheta[2][20000];


void Theta(void);
```

```
void dTheta1(void);
void datafile(void);

FILE *text_file;
#define file_fila "TPD_Sim.dat"

/*-------------------------------------------------------------------*/
void Time(void) {
    TimeScale[0] = 0;
    for (int i = 1; i < 20000; i++) {
        TimeScale[i] = TimeScale[0] + i*dt;
    }
}

/*-------------------------------------------------------------------*/
void TempRamp(void) {
    TempScale[0] = T0;
    for (int i = 1; i < 20000; i++) {
        TempScale[i] = TempScale[i-1] + dT;
    }
}

/*-------------------------------------------------------------------*/
void Theta(void) {
    Theta1[0][0] = Theta01;
    Theta1[1][0] = Theta02;
```

```
    for (int j = 0; j < 20000; j++) {
        dTheta[0][j] = -A*exp(((-Eact1) / (R * TempScale[j])))
           * pow(Theta1[0][j], n1)*dt;
        dTheta[1][j] = -A2*exp(((-Eact2) / (R * TempScale[j])))
            * pow(Theta1[1][j], n2)*dt;
        Theta1[0][j + 1] = Theta1[0][j] + dTheta[0][j];
        Theta1[1][j + 1] = Theta1[1][j] + dTheta[1][j];
        if (Theta1[0][j + 1] < 0) {
            Theta1[0][j + 1] = 0;
        }
        else if (Theta1[1][j + 1] < 0) {
            Theta1[1][j + 1] = 0;
        }
    }
}

/*-------------------------------------------------------------------*/
int main(void) {
        srandom(time(NULL));

        Time();
        TempRamp();
        Theta();
        for (int j = 0; j < 20000; j++) {
            Rate[0][j] = (-dTheta[0][j] / dt);
            Rate2[0][j] = (-dTheta[1][j] / dt);
```

```
            Total[0][j] = (Rate[0][j]+Rate2[0][j]);
        }
    datafile();
    return 0;
}

/*--------------------------------------------------------------*/
void datafile(void) {
    if ((text_file = fopen(file_fila, "wt")) == NULL) {
        printf("Error\n");
    }

    for (int i = 0; i < 20000; i++) {
        fprintf(text_file,"␣%1.20f␣%1.20f␣%1.20f␣%1.20f\n",
                TempScale[i],
                Rate[0][i],
                Rate2[0][i],
                Total[0][i]
                );
    }
    fclose(text_file);

}
/*--------------------------------------------------------------*/
```

CURRICULUM VITAE

DUSTIN R. OLSON

EDUCATION

University of Wisconsin Milwaukee *2014 - 2019*
Ph.D in Chemistry GPA: 3.78
Department of Chemistry & Biochemistry

University of Wisconsin Whitewater *2009 - 2013*
Bachelor of Chemistry, ACS Approved

RESEARCH EXPERIENCE/INTERESTS

- Molecular electronics
- Surface Science
- Nano-tribology/Mechanochemistry

SKILLS

Experimental Techniques
AES (Auger Electron Spectroscopy), STM(Scanning Tunneling Microscopy)
AFM(Atomic Force Microscopy), LEED (Low Energy Electron Diffraction)
E-Beam/Photolithography, SEM (Scanning Electron Microscopy), RAIRS (Reflection Adsorption Infrared Spectroscopy), MS (Mass Spectroscopy)

Computing Software/Languages
C++, Labview, OriginLab, Microsoft Office, LaTeX

Other Applicable Skills
Basic electronics repair, Mechanical aptitude, Cleanroom experience

ACADEMIC ACHEIVEMENTS

• Selected for NSF Funded International Research Experience for Students(IRES): Indian Institute of Chemical Technology, Hyderabad, India/ University Wisconsin, Whitewater (2013)
• Accepted user proposal request for instrument time at the Center for Functional Nanomaterials (CFN), Brookhaven National Laboratory, Upton NY (2017)
• UWM Chemistry Graduate Student Council travel award (2018)
• VI San Luis School and Conference on Surfaces and Catalysis Fellowship, Sante Fe, Argentina (2018)

RELEVANT EXPERIENCE

Graduate Teaching/Research Assistant

PRESENTATIONS

• National Conference of Undergraduate Research (NCUR), University of Wisconsin-La Crosse, Poster Presentation. (2013)
• Undergraduate Research Day, University of Wisconsin-Whitewater, Poster Presentation. (Fall 2013)
• VI San Luis School and Conference on Surfaces and Catalysis , Sante Fe, Argentina, Poster Presentation. (2018)
• American Vacuum Society (AVS) Prairie Chapter Symposium, Chicago, IL, Poster Presentation. (2018)

PUBLICATIONS

1. **Olson, D**., Gao, H., Tang, C., Tysoe, W. T., & Martini, A. (2015). Pressure dependence of the interfacial structure of potassium chloride films on iron. Thin Solid Films, 593, 150-157.

2. Abuflaha, R., **Olson, D**., Bennett, D. W., & Tysoe, W. T. (2016). Surface chemistry and structures of 1, 4-phenylene diisocyanide on gold films from solution. Surface Science, 649, 56-59.

3. Zheng, X., Xu, Y., Geng, J., Peng, Y., **Olson, D**., & Hu, X. (2016). Tribological behavior of Fe3O4/MoS2 nanocomposites additives in aqueous and oil phase media. Tribology International, 102, 79-87.

4. Xu, Y., Yu, J., Geng, J., Abuflaha, R., **Olson, D**., Hu, X., & Tysoe, W. T. (2018). Characterization of the Tribological Behavior of the Textured Steel Surfaces Fabricated by Photolithographic Etching. Tribology Letters, 66(2), 55.

5. **Olson, D**., Boscoboinik, A., Manzi. S., & Tysoe, W, T. (2019). Chemical Self-Assembly Strategies for Designing Molecular Electronic Circuits; Demonstration of Concept.
   The Journal of Physical Chemistry C, 123(16), 10398-10405.

6. Xu, Y., Zheng, Q., Abuflaha, R., **Olson, D**., Furlong, O., You, T., ... & Tysoe, W. T. (2019). Influence of dimple shape on tribofilm formation and tribological properties of textured surfaces under full and starved lubrication. Tribology International.

7. **Olson, D**., Boscoboinik, A., & Tysoe, W, T. (2019). Chemical self-assembly strategies for designing molecular electronic circuits. Chemical Communications

8. **Olson, D**., Bavisotto, R., Hopper, N., Abuflaha, R., Schwabacher, A., Fenske, T., & Tysoe, W, T. (2019). Surface Chemistry and Electron Transport of an Asymmetric Molecular Linker, 4-Isocyanophenyl Disulfide on Gold (Manuscript In Preparation).